

Conquering Metal–Organic Frameworks by Raman Scattering Techniques

Jonas Tittel, Fabian Knechtel, and Evelyn Ploetz*

Metal–organic frameworks (MOFs) have emerged as a versatile class of materials. Understanding the structural and chemical properties of MOFs is essential for tailoring their performance to suit specific applications. In recent years, Raman spectroscopy, a non-destructive vibrational spectroscopic technique, has evolved into a powerful tool for characterizing MOFs. Beyond spontaneous Raman scattering, numerous advanced Raman techniques have been developed to amplify the inherently weak Raman signal. These innovations have significantly enhanced the spatial resolution, frame rate, and sensitivity of Raman imaging, thereby opening up new possibilities for applications, such as label-free sensing. This tutorial work is designed to demystify the fundamental theory and instrumentation of Raman spectroscopy, elucidating the differences between commonly used Raman techniques. Particular emphasis is placed on their advantages and limitations when applied to MOF materials. Furthermore, this work showcases how Raman techniques are employed in studying MOF systems to address societal needs and explore future directions. Ultimately, this review emphasizes the crucial role of Raman spectroscopy and the development of novel Raman-based in situ techniques to conquer the field of MOFs.

the Cambridge Structural Database (CSD) since their first publications (Figure 1).^[2] Currently, another 500.000 structures are predicted by computational screening and machine learning.^[3] Concomitantly, properties and applications of MOFs are manifold and nowadays tuned for specific purposes ranging from gas storage and separation^[4] to pollution removal,^[5] water harvesting,^[6] energy conversion,^[7] catalysis,^[8] sensing,^[9] electronics,^[10] nanotechnology,^[4e,11] biomedical imaging,^[12] or drug delivery.^[13] Physicochemical properties of MOFs can comprise luminescence,^[14] electrical conductivity,^[15] magnetic properties,^[16] or even switchable mechanical properties.^[17]

Many parameters influence the structure and performance of MOFs (Table 1). First, MOFs vary in their composition and functionalization of linkers and secondary building units (SBUs). For example, based on MOF-5, which exhibits an octahedral SBU made of $Zn_4O(CO_2)_6$, we obtain the isorecticular series IRMOF-1-16


by choosing differently functionalized, carboxylate-based linkers (Figure 1A). Additionally, MOFs differ in framework topologies, depending on the geometry and coordination number of the involved building blocks or synthesis pathway leading to different polymorphs. One example is the pyrene-based NU-1000, which contains structural motifs of MOF-901 depending on co-modulators (Figure 1B).^[19] Besides its structural variability with linkers, SBUs, internal/external functionalization, or topology (Figure 1C), MOFs can structurally deviate due to defects or multi-variances. Lastly, MOFs differ in their response to guest molecules. They are classified into three groups according to their stability (Figure 1D).^[20] An overview of the remarkable progress in responsive MOFs was recently given in the literature.^[17,21]

How do we characterize such complex materials? In a perfect world, we would have a single technique that can structurally investigate MOFs, their morphology and framework composition, their interaction with guest molecules, and their performance during applications and reactions, with high temporal and spatial resolution as well as chemical sensitivity at the same time. If we think about flexible MOFs, the methods should be able to 1) localize guest molecules within the framework, 2) monitor the dynamics of guest molecules during uptake, storage, and release from the framework, 3) probe the underlying

1. Introduction

Remarkable progress has been made in the synthesis of metal–organic frameworks (MOFs). This class of crystalline materials is formed by linking molecular building blocks into a pre-determined, extended periodic structure using strong bonds.^[1] Given the nearly unlimited pool of organic and inorganic building blocks, along with the versatility, for instance, in linker functionalization, synthesis pathways, available topologies, connectivity, and framework stability, more than 100.000 different structures have been synthesized and reported in

J. Tittel, F. Knechtel, E. Ploetz
Department of Chemistry and Center for NanoScience (CeNS)
Ludwig-Maximilians-Universität München
Butenandtstr 5–13, 81377 Munich, Germany
E-mail: evelyn.ploetz@lmu.de

 The ORCID identification number(s) for the author(s) of this article can be found under <https://doi.org/10.1002/adfm.202307518>

© 2023 The Authors. Advanced Functional Materials published by Wiley-VCH GmbH. This is an open access article under the terms of the Creative Commons Attribution-NonCommercial License, which permits use, distribution and reproduction in any medium, provided the original work is properly cited and is not used for commercial purposes.

DOI: 10.1002/adfm.202307518

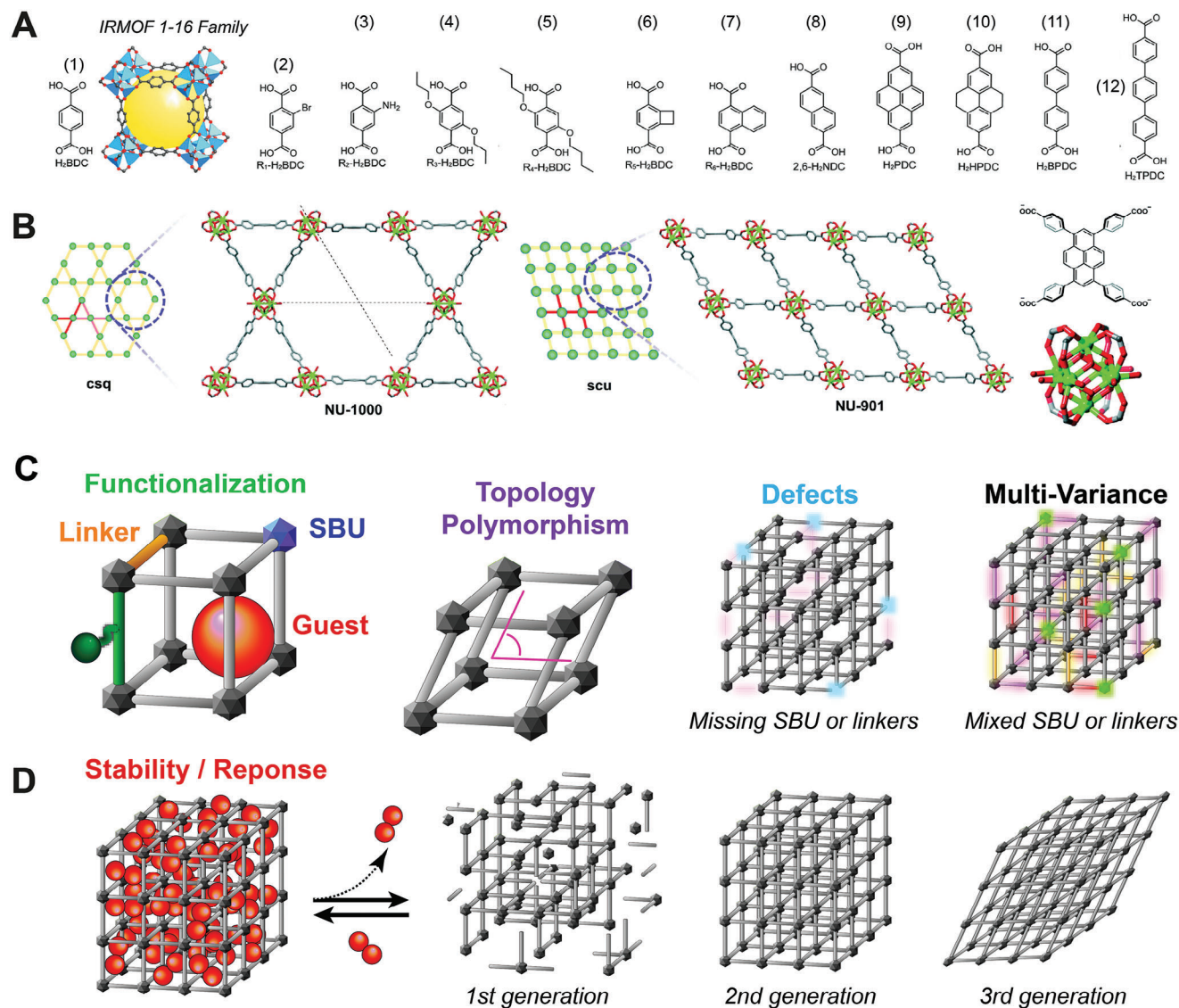


Figure 1. Parameter variations in metal–organic–frameworks. A) Isoreticular design principle. The IRMOF family is formed by a Zn_4O cluster linked to carboxylated organic molecules based on the 1,4-benzodicyclohexane dicarboxylate anion (BDC) in a cubic framework. Adopted and reproduced under the terms of the Creative Commons Attribution 4.0 Int. (CC-BY 4.0) License.^[18] Copyright 2020, The Authors, Published by Israel Chemical Society. B) Alternation between a tetratopic pyrene-based linker and a Zr_6 -based SBU can assemble in two polymorphs: NU 1000 and NU-901. Panel B was reproduced with permission.^[19] Copyright 2018, The Royal Society of Chemistry. C) MOFs can vary with composition (SBU, linker), internal and external functionalization, the presence of guest molecules, their topology and possible polymorphism, defects, potential multivalency, stability, and response. D) MOFs are classified according to their stability and response to external stimuli, such as guest molecules.

conformational changes of the framework as well as any site-specific host-guest interactions, and 4) identify potential phase transitions and intermediate states. So, the technique should simultaneously allow for in situ and in operando characterization of the material to decipher the molecular working mechanism, the underlying dynamics, reaction intermediates, and any structure-property relationships in MOFs. State-of-the-art methods for probing structural changes in MOFs rely on diffraction and magnetic resonance. Their advantages and limitations have been extensively reviewed.^[27] Structural parameters, including lattice dimensions, phase purities, and crystallinity, can be monitored by diffraction methods using X-ray radiation, electrons,

or neutrons.^[27c,n] They probe MOFs mainly under static conditions and are little suitable for in operando measurements. Magnetic resonance (EPR and NMR) spectroscopy can study dynamic processes in situ, including synthesis, functionalization, and host-guest interactions, however, they probe predominantly short ranges inside the material.

In contrast, advanced imaging methodologies based on light microscopy and spectroscopy have become powerful techniques for probing both structural and dynamic information simultaneously in MOFs. Numerous forms of light-matter interaction have been exploited, including UV–Vis absorption and emission for analyzing the electronic transitions of guest molecules,

Table 1. Parameters leading to the large variations of MOF structures including examples from literature.

Variation	Literature
Composition and Functionalization: Isorecticular design	[6a, 18, 22]
Topology: Geometry and coordination	[23]
Polymorphism	[23e, f, 24]
Multivariance and defects	[25]
Framework stability: Response to guest molecules	[21b, c, e, 26]

reactants, or the MOF itself.^[28] Together with confocal or wide-field microscopes, fluorescence-based single molecule imaging can probe single emitters on length scales from centimeters to ≈ 10 nm with a micro- to millisecond time resolution. Still, this approach is only applicable to luminescent guest molecules or MOFs and lacks chemical or structural information about the material. This weakness is mitigated by vibrational spectroscopy techniques based on light absorption in the infrared (IR) region or inelastic scattering of light called Raman scattering.^[29] Besides a static characterization of the chemical composition and structure of the framework, vibrational techniques can follow dynamic processes with high spatiotemporal resolution and help to elucidate reaction intermediates involved in the adsorption process, adsorption sites, defect sites, and many more. They are non-

invasive and serve for structure determination and monitoring of host-guest, guest-guest, and catalytic processes.^[29a-f, 30] Both approaches are powerful for analyzing MOFs as well as composite materials that are not fully crystalline, that contain movable moieties, or materials with transiently binding guest molecules, which cannot be resolved by crystallographic techniques.

While Raman and IR techniques complement each other, their applicability strongly depends on the chosen MOF system, guest system, and application. The absorption of IR light leads to a change in the molecular dipole moment, making IR spectroscopy more sensitive toward heteronuclear (polar functional) groups, such as CO₂. The inelastic scattering process, on the other hand, leads to a change in the polarizability, making Raman spectroscopy sensitive to homonuclear motifs such as the C-C bonds of the organic linker. Raman scattering suffers from low sensitivity compared to IR-based techniques, which can make it less suitable for trace-level detection. Spontaneous Raman scattering is more susceptible to fluorescence interferences, particularly in complex MOF structures, which hinders its application in some cases. Raman instrumentation tended to be more expensive and was, hence, less available in laboratories, contributing to its late adoption for MOFs compared to IR-based techniques (Figure 2). Despite these challenges, researchers increasingly recognize the unique insights Raman scattering can provide: It allows for in operando measurements of reactions in-

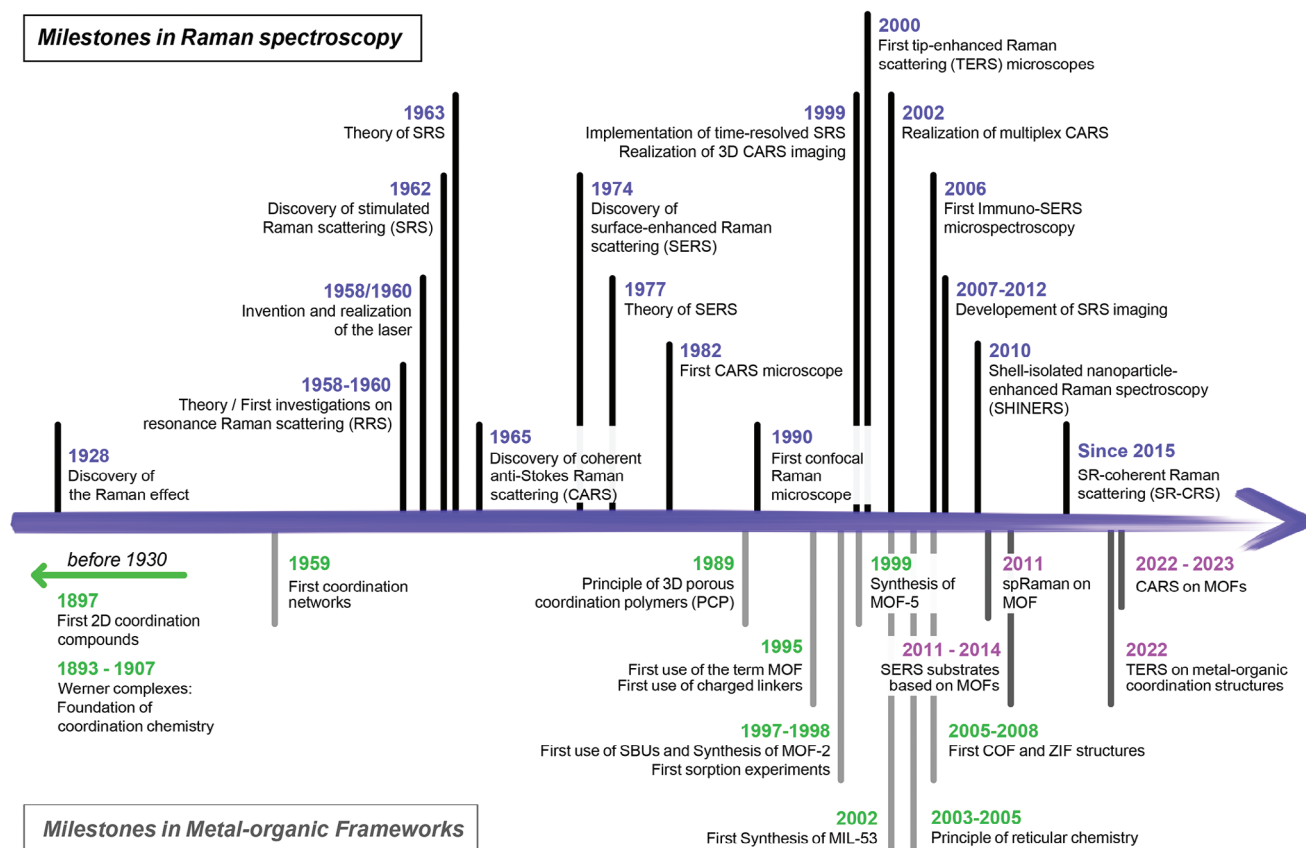


Figure 2. Timeline summarizing Raman and MOF development. References are given in Table 2.

volving water, while the water signature can be overwhelming in IR measurement.^[31] Raman microspectroscopy is the method of choice when it comes to in situ and in operando measurements that require high spatial resolution and access to the low wavenumber region ($<500\text{ cm}^{-1}$). This region is sensitive to chemical bonds involving the SBUs and crystal lattice vibrational modes reporting on crystal polymorphism. Both properties are hardly accessible to IR-based techniques. A primary objective of this tutorial review is, therefore, to offer an accessible introduction to the realm of Raman spectroscopy, demystify its intricate physical principles, underscore its versatile suitability for MOFs, and expound on the innovative solutions to overcome (limitations historically associated with conventional Raman spectroscopy) that allows for addressing societal needs via MOF-based materials. An overview of IR-based techniques can be found elsewhere.^[29b,g,32]

Approaching almost a century after the observation of the Raman effect in 1928 (Figure 2), the term Raman spectroscopy nowadays summarizes a large set of different techniques that vary tremendously in spatiotemporal resolution, sensitivity, read-out, and required instrumentation.^[33] Firstly, different resonance mechanisms are routinely available for enhancing the weak Raman signal. These were discovered during the 1960s/70s after the invention of lasers and included, for instance, coherent anti-Stokes Raman scattering (CARS) and stimulated Raman scattering (SRS), see Section 2. In the early 2000s to 2010s, the invention of pulsed light sources in combination with confocal microscopes pushed the application of advanced Raman techniques beyond pure spectroscopy and enabled 3D imaging and space-resolved spectroscopy. Using the power of plasmonics even single-molecule sensitivity for sensing applications and high-resolution imaging with nanometer resolution can be nowadays achieved based on Surface- and Tip-enhanced Raman scattering (SERS; TERS; Section 2) as well as super-resolved coherent Raman imaging. The first applications to MOFs have been reported since 2011. Technically, Raman scattering has been implemented 1) as bulk spectroscopy using spectrometers, 2) as imaging-based techniques relying on microscopes, as well as 3) in advanced laser-spectroscopy setups to enable time-resolved pump-probe spectroscopy and microscopy (see Table 2 and Section 3).

Given the wide range of technical approaches in Raman spectroscopy and its growing relevance in the field of MOFs, as discussed in recent work,^[29c,e,66] diving into the extensive scientific literature can be quite a challenge for newcomers to the world of Raman spectroscopy and MOFs. The sheer volume of literature encompassing the theory^[33a,d,67] and instrumentation^[68] of Raman techniques and comprehensive reviews on MOFs, spanning their synthesis,^[69] applications,^[70] and characterization,^[11b,13d,32b,71] can be likened to be a labyrinthine challenge. While there are many reviews about specific Raman subfields,^[33c,e,72] there are little to no overview articles with a unified nomenclature comparing available Raman methods, their benefits, pitfalls, and technical requirements, and their application to MOFs. This tutorial review aims to be a starting point for material scientists interested in applying state-of-the-art Raman techniques and for beginners embarking on their journey into spectroscopy. Our goal is to give a comprehensive overview of available Raman methods for studying MOFs 1) in bulk, 2) in situ, and 3) in operando with high spatiotemporal resolution

Table 2. Summary of milestones in Raman spectroscopy and metal-organic frameworks.

Year	Development	Literature
1897	First 2D coordination compound	[34]
1893–1907	Werner complexes: foundation of coordination chemistry	[35]
1928	Discovery of Raman effect	[36]
1958–1960	Theory and first investigations on resonance Raman scattering (RRS)	[37]
1959	First coordination networks	[38]
1958/1960	Invention and realization of the laser	[39]
1962	Discovery of stimulated Raman scattering (SRS)	[40]
1963	Theory of SRS	[41]
1965	Discovery of coherent anti-Stokes Raman scattering (CARS)	[42]
1974	Discovery of surface-enhanced Raman scattering (SERS)	[43]
1977	Theory of SERS	[43,44]
1982	First CARS microscope	[45]
1989	Principle of 3D porous coordination polymers (PCP)	[46]
1990	First confocal Raman microscope	[47]
1995	First use of the term MOF	[48]
1995	First use of charged linkers	[49]
1997	First sorption experiments involving PCPs	[50]
1998	First use of SBUs and synthesis of MOF-2	[51]
1999	Synthesis of MOF-5; Implementation of time-resolved SRS spectroscopy; 3D CARS imaging	[52]
2000	First Tip-enhanced Raman scattering (TERS) microscopes	[53]
2002	Realization of multiplex CARS	[54]
2002	First synthesis of MIL-53	[26n]
2003–2005	Principle of reticular chemistry	[1,22b,55]
2005–2007	First COF structures	[56]
2006–2008	First ZIF structures	[57]
2006	First Immuno-SERS microspectroscopy	[58]
2007–2012	Development of SRS imaging	[59]
2010	Shell-isolated nanoparticle-enhanced Raman spectroscopy (SHINERS)	[60]
2011	MOF investigation by spontaneous Raman	[61]
2011–2014	First MOF substrates for SERS	[62]
Since 2015	Far-field super-resolved coherent Raman imaging	[63]
2022	TERS on metal-organic coordination structures	[64]
2022–2023	CARS on MOFs	[65]

on different lengths scales, and time spans. We divided this review into three sections, which are self-coherent so that single sections can be skipped depending on the scientific background or interest of the reader. We start by explaining the fundamental principle underlying Raman scattering, its properties, and strategies to enhance the signal strength by resonance phenomena

Raman Spectroscopy			
Signal Enhancement	Excitation: Geometry and Polarization	Instrumentation	Detection Modality
Spontaneous Raman	Transmission	Spectroscopy	Fourier - Domain
Surface-enhanced Raman	Backscattering / Epi	Microspectroscopy	Time - Domain
Tip-enhanced Raman	Angle-dependence	Microscopy	Bulk
Nonlinear Raman	Polarization-dependence	,AFM'-type measurements	<i>In situ</i>
Resonance Raman	Optical Activity	Pump probe spectroscopy	<i>In operando</i>

Figure 3. Differences among Raman techniques. Raman techniques for time- and space-resolved measurements can be distinguished according to four categories: 1) their (potential) signal enhancement, 2) the way the laser excitation interacts with the sample, 3) the required instruments, and 4) the spatial and temporal range in which the sample shall be investigated.

in coherent or plasmonic processes. We then discuss different Raman methodologies and describe the technical instrumentations, their functionality, and their limitations. Afterward, we give a short overview, including recent applications on how Raman methodologies can be exploited to investigate MOFs. Lastly, we discuss future applications of Raman techniques for guiding and supporting the synthesis of MOFs for addressing societal needs, including environmental remediation.

2. Raman Spectroscopy: Principles

Raman spectroscopy has become a highly versatile analytical method with various technical realizations differing in their measurement mode, instrumentation, signal enhancement, or detected signature (Figure 3).^[33a] In this section, we will first give a short introduction to spontaneous Raman scattering, its working principle, and its dependencies upon laser excitation, polarization, and detection geometry. Afterward, we will look into strategies to enhance the intrinsically weak process based on electronic, plasmonic, or coherent resonances, which can be employed independently but also in combination. We will discuss Resonance Raman Scattering (RRS), near-field phenom-

ena underlying surface-enhanced Raman scattering (SERS) and tip-enhanced Raman scattering (TERS), and nonlinear Raman approaches including Coherent anti-Stokes Raman Scattering (CARS) and Stimulated Raman Scattering (SRS).

2.1. Spontaneous Raman Scattering

Light interacts with matter by three different processes: by transmittance, by absorption followed by emission, and by scattering. When incident photons interact with molecules or the crystal lattice, the photon is either scattering elastically or inelastically. During elastic light scattering, called Rayleigh or Mie scattering, no material excitation takes place. The scattered light has the same wavelength as the incident one (Figure 4A; Process 1). Inelastic scattering processes, such as Raman, Brillouin, or Compton scattering, excite the material and lead to isotropic radiation at different wavelengths as the incident light. Spontaneous Raman scattering describes the vibrational (de-)excitation of molecular entities in matter by inelastic light scattering (Figure 4A; Process 2–4).^[33a,68g,73] It was theoretically predicted in 1923 by Smekal^[74] and experimentally observed five years later by Raman and Krishnan in 1928,^[36,75] when they detected that the scattered light of different solutions was polarized. At the same time, Landsberg

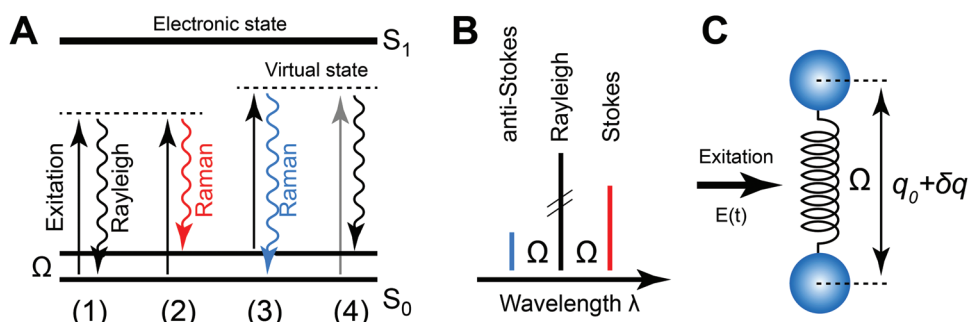


Figure 4. Spontaneous Raman scattering. A) Jablonski energy diagram showing transitions involved during 1) Rayleigh scattering, 2) Stokes scattering, 3) anti-Stokes scattering, and 4) Stokes Scattering with a different excitation wavelength. B) Spectral shift during Raman scattering. C) Classical description of a diatomic molecule excited by an incident light field $E(t)$.

and Mandelstam discovered the effect in crystals.^[76] Raman was honored with the Nobel Prize in Physics in 1930.

Raman scattering leads to an energy exchange between the incident photons and the material. In the case of solid-state samples such as MOF crystals, the energy exchange creates a vibrational quantum in the lattice, known as an optical phonon. Guest-molecules will change their rotational-vibrational state. During the Raman process, the photons either transfer energy into matter by exciting a molecular vibration Ω or receive energy from an existing phonon vibrating at Ω . The shift in angular frequency Ω is given by

$$\omega_{\text{Raman}} = \omega_p \pm \Omega \quad (1)$$

Here, the subscript p denotes the angular frequency of the incident photon radiated by the pump laser, i.e. the excitation source, and Raman refers to the scattered light. When the loss of energy results in a spectral red shift to longer wavelengths, the process is referred to as Stokes scattering (Figure 4B). Accordingly, when the gain of energy leads to blue-shifted photons, i.e., radiation at shorter wavelengths, we speak about anti-Stokes scattering. Raman scattering gives access to vibrational transitions between 10 to 5000 cm^{-1} . The spectral excitation range spans from UV to NIR (Figure 4A; Ex. 4). The scattering process does not require the presence of a molecular quantum state, i.e., an electronic energy level of the material. The interaction with the crystal lattice or molecule induces a distortion of the electron cloud and, hence, a change in polarizability involving virtual states, which are represented as dotted lines in the Jablonski diagram (Figure 4A).

To describe the physical origin of the Raman effect in a classic picture,^[77] let us consider two molecular entities that can oscillate against each other with an intrinsic vibrational frequency Ω (Figure 4C). The presence of the incident light is described by an oscillating electric field $E(t) = E_0 \cos(\omega_p t)$, which induces a dipole momentum μ per unit cell inside the material given by

$$\mu(t) = \alpha(t) \cdot E_0 \cos(\omega_p t) \quad (2)$$

Here, $\alpha(t)$ denotes the polarizability. It represents the deformability of the electron cloud or the ease of the material to build up a dipole moment once an electric field is applied. The nuclear distance q , also called normal mode, can change over time with the inherent Raman frequency Ω

$$q(t) = q_0 \cos(\Omega t) \quad (3)$$

Small changes δq in this distance q , however, affect the polarizability $\alpha(t)$ of the material, which can be approximated by a Taylor series around its equilibrium value α_0

$$\alpha(t) = \alpha_0 + \left(\frac{\partial \alpha}{\partial q} \right) \Big|_0 \cdot q(t) \quad (4)$$

By combining Equations 2–4, the macroscopic polarization of the material $P(t) = N \cdot \mu(t)$, given by all dipole moments per unit cell together, can be expressed as

$$P(t) = N \cdot \left[\alpha_0 + \left(\frac{\partial \alpha}{\partial q} \right) \Big|_0 \cdot q_0 \cos(\Omega t) \right] \cdot E_0 \cos(\omega_p t) \quad (5)$$

This expression comprises three terms in total:

$$P(t) = N \cdot \alpha_0 \cdot E_0 \cos(\omega_p t) \quad (1)$$

$$+ 0.5 \cdot N \cdot \left(\frac{\partial \alpha}{\partial q} \right) \Big|_0 \cdot q_0 E_0 \cdot \cos(\omega_p - \Omega) t \quad (2) \quad (6)$$

$$+ 0.5 \cdot N \cdot \left(\frac{\partial \alpha}{\partial q} \right) \Big|_0 \cdot q_0 E_0 \cdot \cos(\omega_p + \Omega) t \quad (3)$$

The first term describes the elastic Rayleigh scattering at the incident frequency ω_p with constant polarizability. The second and the third terms describe the inelastic Stokes (2) and anti-Stokes (3) scattering, respectively (Figure 4A). The frequencies of these two terms are shifted by $\pm \Omega$ with respect to the frequency of the incident light field. Both terms vanish if there is no change in polarizability $(\partial \alpha / \partial q)|_0$. Hence, vibrational modes, for which the polarizability at q_0 does not change, are called Raman inactive, and are not detectable by Raman spectroscopy.

The intensity of the scattered Raman light can be described by a Hertzian dipole, i.e., a radiating emitter.^[33a,68g,73] The intensity is proportional to the number of scattering molecules N , i.e., the concentration, and the excitation intensity I_p of the pump laser. It scales with the frequency of the scattered light at $\omega_p \pm \Omega$ to the fourth power, and the square of the change in polarizability $(\partial \alpha / \partial q)|_0$

$$I_{\text{Raman}} \propto N \cdot I_p \cdot \frac{(\omega_p \pm \Omega)^4}{\Omega \cdot \left(1 - e^{-\frac{h\Omega}{kT}} \right)} \cdot \left(\frac{\partial \alpha}{\partial q} \right) \Big|_0^2 \quad (7)$$

Enhanced Raman scattering is observed for exciting light sources at large frequencies, i.e., lower wavelengths in the blue to green spectral range. A major pitfall of this strategy is the rising contribution of fluorescence and enhanced photodegradation. Hence, the laser wavelength in the UV–Vis needs to be carefully chosen according to the sample system. Besides, the majority of molecules are in the vibrational ground state at room temperature. Following a Boltzmann distribution, the absolute signal is more intense on the Stokes than anti-Stokes side (Figure 4B). Lastly, the Raman intensity depends on the change of the polarizability α , which is a second-rank tensor. The polarizability depends upon the polarization state of the incident light source, the orientation of the crystalline material, and the detection geometry and polarization sensitivity. The polarization of the excitation source can be nonpolarized, linearly (s or p), or circularly (left-/right-handed) polarized (see Section 3.3.4). Besides the detection geometry under 0° , 90° , or 180° with respect to the propagation direction of the incident light, the measured Raman intensity depends on the polarization sensitivity of the detection scheme. It matters whether the signal is recorded with or without a polarizer in the detection path. A complete overview of the dependencies on polarization and geometry, including the associated selection rules is given by Derek Long in the reference tables for Chapter 5 of his book on Raman scattering.^[33a]

2.2. Signal Enhancement

Raman scattering is a rare process. Raman cross sections are in the range of 10^{-28} to 10^{-30} cm^2 and several orders of magnitude lower than cross sections observed for absorption processes in the IR (10^{-21} cm^2) or UV–Vis (10^{-18} cm^2), fluorescence

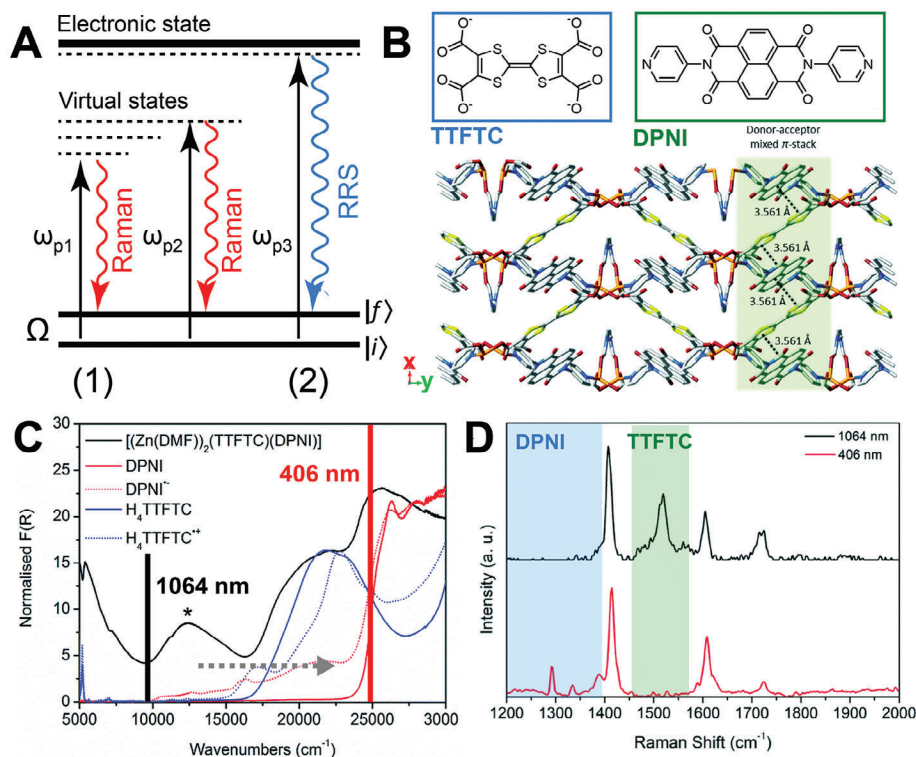


Figure 5. Resonance Raman scattering. A) Jablonski energy diagram of RRS in comparison to spontaneous Raman scattering. With increasing laser frequency $\omega_{p1} < \omega_{p2} < \omega_{p3}$, the excitation is more in resonance with an electronic state of the material. B) Crystal structure of the Zn-MOF $[(Zn(DMF))_2(TTFTC)(DPNI)]$ with the two naphthalene- (DPNI) and tetrathiafulvalene-based (TTFTC) linkers shown along the *c*-axis. The donor-acceptor pair is highlighted in green. C) UV-Vis absorption spectrum of the MOF (black), DPNI (red), its radical anion (dashed red), H_4 TTFTC (blue), and its cation (dashed blue). D) Raman spectrum of the Zn-MOF under 1064 and 406 nm laser excitation (as indicated in panel B). RRS due to both linkers is highlighted in blue and green. Panel B and D were reproduced under the terms of the Creative Commons CC-BY License 3.0.^[81] Copyright 2014, The Authors. Published by The Royal Society of Chemistry. Panel C was reproduced with permission.^[82] Copyright 2018, The Royal Society of Chemistry.

(10^{-19} cm²) or Rayleigh scattering (10^{-26} cm²).^[78] The Raman intensity scales linearly with the number of scatterers, limiting the detection at low concentrations to $\approx 10^{-2}$ M. Hence, increasing the Raman signal requires either elevated laser powers or prolonged measurement times, leading to poor time resolution, significant photo-induced stress, and potential damage to the sample. To overcome this limitation and to enhance the Raman signal, different strategies exploiting resonance phenomena have been introduced: they make use of 1) resonant enhancement of vibrations by coupling the vibrational transition to electronic states of molecules, 2) plasmonic enhancement of electric fields via plasmonic structures which lead to an enhanced excitation power and simultaneously enhanced signal detection and 3) coherent enhancement of the Raman transition by driving the molecular vibration in phase and frequency by external pulsed light sources. The following section describes the associated Raman processes, namely resonant Raman scattering, surface- and tip-enhanced Raman scattering, as well as coherent Anti-Stokes Raman scattering and stimulated Raman scattering.

2.2.1. Resonance Raman Scattering (RRS)

Raman scattering can be drastically enhanced if the energy of the involved photons is close to the energy of an electronic transi-

tion of the investigated material (Figure 5A). The enhancement factor can be up to 10^6 ,^[33a,79] enabling the recording of spectra from samples with concentrations as low as $\approx 10^{-7}$ M or significantly improving acquisition speed.^[80] Still, enhancements ranging from 3 to 4 orders of magnitude are more common depending on the specific sample system. In the case of Resonance Raman Scattering (RRS), the wavelength of the incoming laser source needs to overlap with an electronic transition. Vibrational modes of the material, associated with the absorbing center of the chromophore, will exhibit a greatly increased Raman scattering intensity compared to unrelated Raman modes of the same material or other molecules, such as guest molecules, which remain unaffected. So, the enhancement of specific bands strongly depends on the electronic and molecular structure.

An excellent example for the structural dependence of RRS is a tetrathiafulvalene-naphthalenediimide-based Zn-MOF $[(Zn(DMF))_2(TTFTC)(DPNI)]$; (DMF = *N,N*-dimethylformamide; TTFTC = tetrathiafulvalene-tetracarboxylate; and DPNI = *N,N'*-di(4-pyridyl)-1,4,5,8-naphthalene-tetracarboxy-diimide) (Figure 5B).^[81,82] The MOF structure is assembled from a mix of donor TTFTC and acceptor DPNI ligands showing partial through-space ligand-to-ligand charge transfer. While both molecules absorb in the UV, TTFTC absorbs already in the visible range below 580 nm ($>17\,500$ cm⁻¹; Figure 5C). Upon laser excitation at 1064 nm (≈ 9400 cm⁻¹; Figure 5D), the spontaneous

Raman spectrum of the Zn-MOF shows vibrations at 1413 cm⁻¹ (C = C stretch, TTFTC^{•+}), 1606 cm⁻¹ (C = O stretch, TTFTC⁰), and 1726 cm⁻¹ (C = O stretch, DPNI^{•+}). At 406 nm excitation, however, new transitions below 1400 cm⁻¹ appear due to RRS in the donor DPNI⁰, while the C = C stretch vibration of the neutral acceptor TTFTC⁰ around 1525 cm⁻¹ after RRS at 1064 nm is not visible any longer.

To describe RRS, Raman scattering needs to be at least treated in a semi-quantum mechanical picture: the molecule is described quantum mechanically while the radiation field, dipole moment, and scattering process are dealt with classically. Raman scattering involves two photons and, hence, must be handled via second-order time-dependent perturbation theory. A detailed derivation is beyond this tutorial review and can be found in recent work.^[37d,83] The traditional approach for describing RRS intensities involves a summation of all unperturbed eigenstates E of the resonant electronic state.^[83d] The change in polarizability $(\partial\alpha/\partial q)_0$ due to the vibrational mode q relates to the transition polarizability tensor between an initial vibrational state $|i\rangle$ and a final vibrational state $|f\rangle$ (Figure 5A) described by the Kramers Heisenberg Dirac equation^[83c,d] (a generalized Fermi golden rule)

$$(\alpha_{\rho\sigma})_{fi} = \sum_{E \neq i,f} \frac{\langle f | \hat{\mu}_\rho | E \rangle \langle E | \hat{\mu}_\sigma | i \rangle}{\hbar\omega_{Ei} - \hbar\omega_p - i\Gamma_E} + \frac{\langle f | \hat{\mu}_\sigma | E \rangle \langle E | \hat{\mu}_\rho | i \rangle}{\hbar\omega_{Ef} + \hbar\omega_p + i\Gamma_E} \quad (8)$$

Here, $\hat{\mu}_\rho$ and $\hat{\mu}_\sigma$ represent the dipole operators for the exciting and the emitted electric fields with their respective polarizations. ω_p is the angular frequency of the laser. ω_{Ei} and ω_{Ef} refer to the angular frequencies associated with transitions from the initial vibrational state $|i\rangle$ to any intermediate, excited state $|E\rangle$ of the unperturbed molecule (Figure 5A), followed by a second transition to the final, vibrational state $|f\rangle$. The damping factor Γ_E relates to the lifetime of the intermediate state $|E\rangle$ and is small compared to the involved frequencies of the transitions. $\langle f | \hat{\mu}_\rho | E \rangle$ annotates a transition element for the transition $E \rightarrow f$ due to the exiting electric field responsible for the transition dipole moment μ_p .

In this description, spontaneous Raman scattering is treated as a two-photon process, in which the virtual absorption of a photon from the initial state $|i\rangle$ leads to an entire set of Eigenstates of the molecule, followed by the virtual emission of a second photon and the return to the final state $|f\rangle$. Since Equation 8 describes the spontaneous Raman scattering process, where does the resonant enhancement come from? Let's assume, the laser system is tuned into resonance ($\omega_p \approx \omega_{Ei}$) to the absorption band of the molecule. In this case, the first term starts to dominate, and the equation simplifies to

$$(\alpha_{\rho\sigma})_{fi} \approx \sum_{E \neq i,f} \frac{\langle f | \mu_\rho | E \rangle \langle E | \mu_\sigma | i \rangle}{\hbar\omega_{Ei} - \hbar\omega_p - i\Gamma_E} \quad (9)$$

Since the change in polarizability is proportional to the transition probability, the scattered Raman intensity scales quadratically with the transition polarizability in this semi-classical ap-

proach, in which the scattering is described via an oscillating Hertzian dipole^[83d]

$$I_{\text{Raman}} = I_f \propto I_p \cdot (\omega_p \pm \Omega)^4 \cdot \sum_{\rho,\sigma} |(\alpha_{\rho\sigma})_{fi}|^2 \quad (10)$$

Here, the measured Raman intensity becomes vast when the laser frequency ω_p coincides with the transition frequency ω_{Ei} from the vibrational ground state to the intermediate State $|E\rangle$. Generally, RRS can occur for the incident field being resonant to the molecular transition but also for the scattered field, or both light fields (double resonant) simultaneously, depending on the molecular structure.

2.2.2. Surface Enhanced Raman Scattering (SERS)

Raman scattering of molecules close to a metal surface can be amplified up to 10–11 orders of magnitude depending on the chosen nanostructure.^[84] This phenomenon, called Surface-Enhanced Raman Scattering (SERS), is frequently observed on surfaces of coinage metals like gold, silver, and copper. The underlying enhancement decays fast with distance to the surface ($I_{\text{SERS}} \sim r^{-10}$).^[85] Hence, the range of SERS lasts only a few nanometers and depends on the size, shape, and composition of the plasmonic nanostructure (or surface).^[86] There are two contributions to the overall signal amplification: the chemical mechanism (CM) and the electromagnetic mechanism (EM).^[87] CM effects are based on specific interactions between the molecule and the surface that comprise 1) charge transfer reactions between metal and analytes, 2) transient transfer or hot electrons/holes from the metal, and 3) metal-ligand complex formation.^[88] The EM mechanism dominates and originates from the excitation of localized surface plasmons (LSP). These are light-induced coherent oscillating charges at the metal surface due to the resonant coupling of the metal to the electric field of the incident laser. LSPs result in a strong near-field enhancement (Figure 6). For this effect, it is necessary that the metal film is not continuously flat but locally rough and, therefore, consists of small islands facilitating a local enhancement of the electric field.^[89] Alternatively, (clustered) metal nanoparticles show LSPs allowing EM-enhanced SERS in adsorbed molecules. EM-enhanced SERS takes place in two steps (Figure 6B). In the first step, the incident light causes LSPs (which absorb in the same spectral range as the laser), leading to resonant amplification of the incident light field. Raman scattering in molecules close to the surface is already more intense. Further amplification of the scattered electric field by the LPS occurs in a second step. The enhancement of the two separate steps, G_1 and G_2 , and the total enhancement, described by the enhancement factor EF , are

$$G_1 = \left| \frac{E_{\text{loc}}(\omega_p)}{E_0(\omega_p)} \right|^2 \text{ and } G_2 = \left| \frac{E_{\text{loc}}(\omega_p - \Omega)}{E_0(\omega_p - \Omega)} \right|^2 \text{ with } EF = G_1 \cdot G_2 \quad (11)$$

The chemical enhancement, on the other hand, describes charge transfer mechanisms between the molecules and the metal surface, which then leads to a change in the polarizability derivative of the molecule and to an increase of the Raman cross section consequently.^[72a]

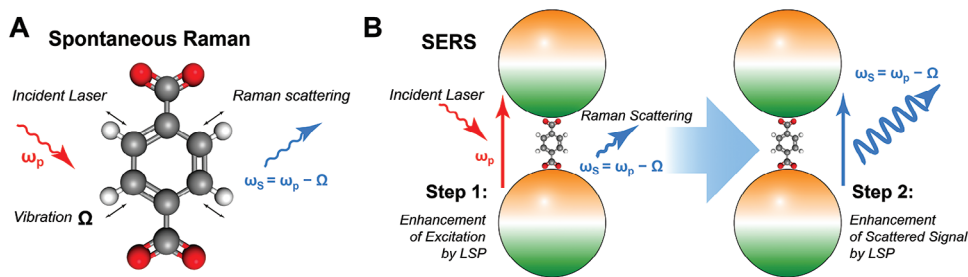


Figure 6. Schematics of the surface-enhanced Raman scattering by localized surface plasmons. A) Electric fields involved in spontaneous Raman scattering. B) Surface-enhanced Raman scattering of a molecule within a plasmonic hotspot. Step 1: The incident laser field induces localized surface plasmons (LSPs) in the metal particles, leading to an amplification of the incident electric field and facilitating Raman scattering. Step 2: The electric field of the scattered light couples again with the LSPs and becomes further enhanced.

The absolute signal amplification by SERS depends strongly on the optical properties of the metal surface or the nanoparticles, which usually interact with light in the visible to near-infrared regime. To understand the resonant coupling between plasmons and the incident light, we need to address the optical response of the metal itself. The following paragraph provides an introduction to the field of plasmonics and SERS. A detailed discussion can be found in recent, excellent reviews.^[72a,84b,90]

Bulk Plasmons: Following the Drude model, metals can be seen as a lattice of immobile positively charged ions and a freely moving electron gas between the lattice. The movement of the electrons is only damped by collisions with the lattice, which appears at a given frequency $\gamma = 1/\tau$, where τ denotes the relaxation time, i.e., the time between collisions. Thus, if an external electric field $E(t)$ interacts with the metal, electrons experience an additional oscillating force. The total force modifying the movement of the electrons (described by its mass m , and charge e) can be expressed as

$$m\ddot{x} - \gamma\dot{x} = -eE(t) \quad (12)$$

The differential equation can be solved for a harmonically driven electric field $E(t) = E_0 e^{-i\omega t}$, where E_0 is the amplitude and ω the angular frequency of the incident laser, which simultaneously acts as the Raman pump laser at $\omega = \omega_p$. The oscillating displacement is

$$x(t) = \frac{e}{m(\omega^2 + i\gamma\omega)} E(t) \quad (13)$$

and responsible for the polarization $P = -Nex(t)$. Overall, the electric field induces a dielectric displacement D in the metal, which is given by

$$D(t) = \epsilon_0 E(t) + P(t) = \epsilon_0 \left(1 - Ne \frac{e}{\epsilon_0 m(\omega^2 + i\gamma\omega)} \right) E(t) \quad (14)$$

where ϵ_0 is the permittivity of the vacuum, i.e., free space without material. If we now consider that the electric displacement field D in a material due to an external electrical field is further given by $D = \epsilon_0 \epsilon_r E$, we find that the dielectric constant ϵ_r is frequency dependent (**Figure 7**)

$$\epsilon_r(\omega) = 1 - \frac{\omega_{\text{Plasma}}^2}{\omega^2 + i\gamma\omega} \quad \text{with} \quad \omega_{\text{Plasma}}^2 = \frac{Ne^2}{\epsilon_0 m} \quad (15)$$

Here, N describes the electron density within the metal, and ω_{Plasma} is the so-called plasma frequency. It refers to the limit, where no electromagnetic waves lower in frequency can couple to the metal. The plasma frequency of many metals, including copper (142 nm), gold (139 nm), and silver (134 nm), lies in the UV range of the electromagnetic spectrum.^[91]

The scattering time at room temperature is on the order of $\tau \approx 10^{-14}$ s.^[92] Hence, in the UV-VIS range, the angular frequency ω is larger than the damping γ . The real part of the dielectric constant dominates over the imaginary damping part and, therefore $\epsilon_r(\omega) = 1 - \frac{\omega_{\text{Plasma}}^2}{\omega^2}$ becomes the dielectric function of the undamped electron gas. In this case, the dispersion relation for electromagnetic fields reads as

$$\omega(k)^2 = \frac{k^2 c^2}{\epsilon_r(\omega)} = k^2 c^2 + \omega_{\text{Plasma}}^2 \quad (16)$$

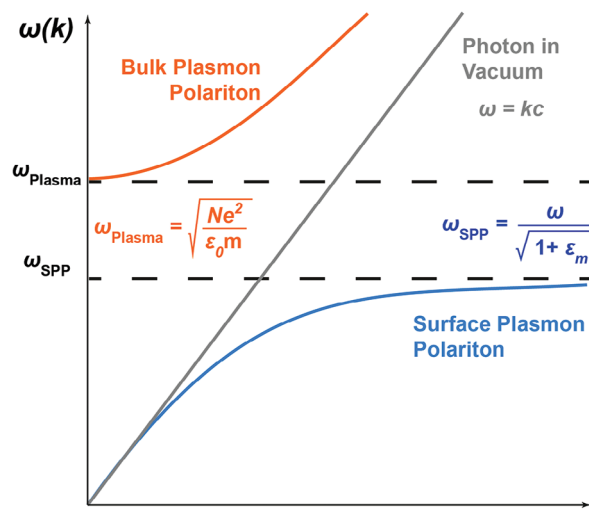


Figure 7. Dispersion relationship for plasmons. Bulk plasmons (red line) form when the dielectric constant becomes zero. The dispersion relationship for surface plasmons, which is discussed in the following section, is shown in blue. The grey line depicts the linear relationship between the angular frequency and the wavevector by the speed of light. The dotted lines mark the reference frequencies of the plasma and surface plasmon frequency.

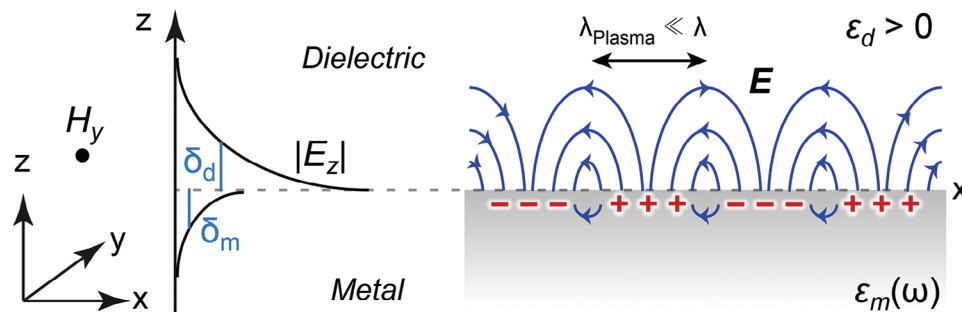


Figure 8. Propagating surface plasmon polariton at the interface of a metal and dielectric. Left: Evanescent electric field in the regions characterized by their decay constants $\delta_{d/m}$. Right: The surface plasmon polariton propagates in the X-direction and oscillates in the Z-direction; The propagation is wavelength-, i.e., frequency-dependent.

For $\omega > \omega_{\text{plasma}}$, the local excitation can propagate within the metal. For the case $\omega = \omega_{\text{plasma}}$, where $\epsilon_r(\omega)$ equals zero, collective longitudinal oscillations of the electron gas occur, which move against the fixed lattice of the positive atoms at the plasma frequency. These oscillations are called bulk plasmons and represent longitudinal waves that cannot couple to traverse electromagnetic fields (such as light). Bulk plasmons cannot be excited by direct or scattered light.

Surface Plasmons: Surface plasmons are collective electron oscillations that travel along a metal/dielectric interface without penetrating the metal's volume. These oscillations can be described for a metal/dielectric interface oriented in the XY plane ($z = 0$; **Figure 8**). For $z < 0$, we deal with metal described by its frequency-dependent dielectric function $\epsilon_m(\omega)$. For $z > 0$, $\epsilon_d > 0$ is a real dielectric constant of the dielectric material. We now consider an electromagnetic wave $E(r, t) = E(z)e^{ikx}$, that is only oscillating in the Z-direction, i.e., perpendicular to the XY plane, such as light. The oscillating wave is traveling exclusively in the X-direction. The Helmholtz equation of this wave simplifies to

$$\frac{\partial^2 E(z)}{\partial z^2} + (k_0^2 \epsilon - k^2) E = 0 \quad (17)$$

where k is the wave vector along the X-direction (or simply the inverse of the wavelength). As shown by Stefan Maier,^[90f] solutions for this simplified Helmholtz equation (where only E_x , E_z , and H_y are non-zero) only exist for transverse magnetic (p) polarized waves. As a result, it deals with a linked system of an electromagnetic wave that propagates in the dielectric medium and simultaneously an oscillating electron plasma at the metal surface. Here, the oscillating electric field decays exponentially into both spaces, the metal and dielectric medium (**Figure 8**; left). The quantum of this oscillation is called surface plasmon polariton (SPP).

How does the wave, i.e., the SPP, propagate at the interface depending on the frequency? It is described by its dispersion relation (**Figure 7**). Since the electric and magnetic fields at the boundary between both media need to be continuous, the dispersion relation of SPPs propagating at the interface is

$$k = \frac{\omega}{c} \sqrt{\frac{\epsilon_d \epsilon_m}{\epsilon_d + \epsilon_m}} \quad (18)$$

Following the Drude model in the absence of any damping, the metallic dielectric function becomes a real quantity (cf. Equation 15). For a nearly frequency-independent dielectric ($\epsilon_d = \text{Constant}$), the dispersion relation $\omega(k)$ for surface plasmon polaritons is shown in **Figure 7**. While the dispersion relation is nearly linear at small wave vectors k , it shows an asymptotic behavior for large values. The group velocity ($v_g = \frac{d\omega}{dk}$) approaches zero for large wave vectors k , i.e., the SPP features a local electrostatic character. For large values, frequencies come close to the surface plasmon frequency

$$\omega_{SPP} = \sqrt{\frac{\omega}{1 + \epsilon_2}} \quad (19)$$

which depends on the dielectric constant and, hence, on the type of metal. Since the dispersion curve of light $\omega = kc$ lies on the left compared to the SPP dispersion, the wavelength λ_{SPP} of the SPP, which reversely relates to the wavenumber $\lambda_{SPP} = 2\pi/\text{Re}[k]$ is much smaller than for an electromagnetic wave in a vacuum or a dielectric. The out-of-plane component of the electric field is purely imaginary. It exhibits an evanescent field in the Z-direction that decays exponentially in both the dielectric and the metal (**Figure 8**). The decay length δ_i in both media can be expressed as^[93]

$$\delta_i = \frac{\lambda}{2\pi} \sqrt{\frac{|\Re(\epsilon_m)| + \epsilon_d}{\epsilon_i^2}} \quad (20)$$

where i denotes the propagation medium. Since the absolute values of the dielectric constants for metals are larger than for dielectrics, the decay in the metal generally is faster than in the dielectric. At room temperature, typical values of penetration depth of SPP are ≈ 10 – 100 nm (in metals) and ≈ 100 – 1000 nm (in dielectrics), respectively, in the visible part of the spectrum.^[93] Equally, the wave vector k is a complex quantity with an imaginary part responsible for the damping in the X-direction. The resulting plasmon propagation length l_{SPP} in the X-direction is^[93]

$$l_{SPP} = \frac{1}{2\Im m(k)} \quad (21)$$

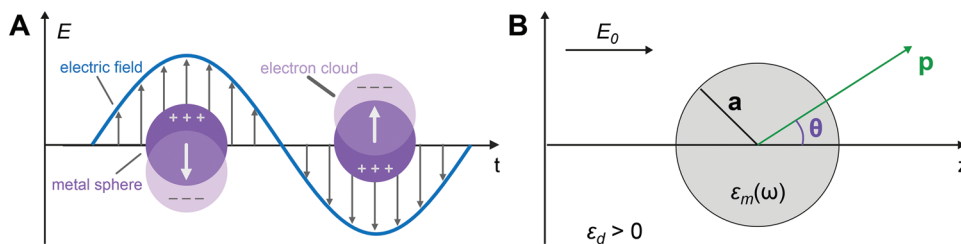


Figure 9. Localized surface plasmons in a nanoparticle. A) Delocalized electrons start to collectively oscillate as so-called localized surface plasmons in response to the external electric field of the excitation source if their hosting nanostructure is smaller than the wavelength of the incident light. B) Schematic for describing the induced dipole p inside a spherical metallic nanoparticle with radius a . The external electrostatic field E oscillates perpendicular to the direction of propagation along the Z -axis.

At room temperature, the propagation lengths l_{SPP} of SPP in metals is $\approx 0.5\text{--}5\ \mu\text{m}$ in the visible part of the spectrum and up to $50\ \mu\text{m}$ in the IR.^[90f] Overall, SPPs have a highly bound nature close to the interface. They cannot be excited by the illumination of light directly because the energy and the momentum cannot be conserved at the same time. Hence phase matching techniques like prisms or gratings are required to excite SPPs on flat metal/dielectric interfaces.

Localized Surface Plasmons: If neither bulk plasmons nor surface plasmon polaritons can directly interact with an external electric field, which interaction is responsible for surface-enhanced Raman scattering? Localized Surface Plasmons (LSPs). LSPs are non-propagating plasmon excitations in metal nanostructures that are smaller than the wavelength. These nanostructures can be nanoparticles but also locally rough surfaces. An electric field outside the nanostructure can penetrate the small volume and, hence, shift the electron gas collectively relative to the static ions (**Figure 9A**). Consequently, a dipole moment in the nanostructure is induced, acting as a local emitter. In contrast to SPPs on flat surfaces, LSPs can be excited by the illumination of light directly without any coupling/phase matching techniques.^[90g]

The simplest example of such a nanostructure is a metallic nanosphere (**Figure 9B**) with radius $a \ll \lambda$ surrounded by an isotropic, non-absorbing dielectric (with dielectric constant ϵ_d). Because of the small radius of the nanosphere compared to the wavelength of the electric field $E = E_0 e^{i\omega t} \hat{e}_z$, the field can be seen as quasistatic over the NPs volume. To determine the electric field $E = -\nabla\Phi$ inside and outside of the sphere, first, the corresponding electric potentials $\Phi_{in/out}$ need to be derived, which can be obtained by solving the Laplace equation ($-\nabla^2\Phi = 0$) for a nanosphere at the origin of the spherical coordinate system. A stepwise derivation can be found elsewhere.^[90e,g] The electric potential is given by

$$\Phi_{in} = -\frac{3\epsilon_d}{\epsilon_m + 2\epsilon_d} \cdot E_0 \cdot r \cdot \cos(\theta) \quad (22a)$$

$$\Phi_{out} = -E_0 \cdot r \cdot \cos(\theta) + \left[\frac{\epsilon_m - \epsilon_d}{\epsilon_m + 2\epsilon_d} \right] \frac{a^3}{r^3} E_0 \cdot r \cdot \cos(\theta) \quad (22b)$$

where ϵ_d is the dielectric constant of the dielectric, ϵ_m is the dielectric function of the sphere, θ is the angle between the electric

field E , and the position vector r or dipole p . The derived electric fields are

$$E_{in} = \frac{3\epsilon_d}{\epsilon_m + 2\epsilon_d} \cdot E_0 \hat{e}_z \quad (23a)$$

$$E_{out} = E_0 \hat{e}_z + \left[\frac{\epsilon_m - \epsilon_d}{\epsilon_m + 2\epsilon_d} \right] \frac{a^3}{r^3} E_0 (2 \cos(\theta) \hat{e}_r + \sin(\theta) \hat{e}_\theta) \quad (23b)$$

The electric field outside the metal nanoparticle is a superposition of the incident electric field (first term) and the scattered field (second term). Both electric fields are maximally enhanced if $\epsilon_m + 2\epsilon_d$ approaches zero. The scattered field is identical to the field of a dipole p at the center of the sphere described by^[94]

$$p = \epsilon_0 \epsilon_m \alpha E \quad \text{and} \quad \alpha = 4\pi a^3 \frac{\epsilon_m - \epsilon_d}{\epsilon_m + 2\epsilon_d} = 4\pi a^3 g_m \quad (24)$$

with α being the polarizability of the small nanosphere, which depends on both dielectric constants and the volume of the particle. g_m denotes the gain factor frequently introduced in SERS. The local field of the induced dipole is cylindrically around the z -axis (**Figure 10A**) and reads as

$$E_{local} = \frac{p}{4\pi\epsilon_0\epsilon_m} \frac{a^3}{r^3} (2 \cos(\theta) \hat{e}_r + \sin(\theta) \hat{e}_\theta) \quad (25)$$

The field enhancement will occur around the poles parallel to the incident field and amount to 10^6 to 10^7 for colloidal silver and gold spheres.^[90c] If two nanoparticles form dimers, the external electrical field will interact with each of the nanoparticles individually (**Figure 10B**). For an electrical field perpendicular to the dimer axis, both nanoparticles will act as independent emitters showing an individual enhancement around their poles. If the electrical field, however, is parallel to the dimer axis, the electric fields of the dipole emitters will superimpose and create so-called hot spots between them (**Figure 10C**). Strong field enhancement does not solely occur in isolated or aggregated spherical nanoparticles but in nanostructures of all kinds of shapes or cavities and various arrangements. In the case of more complicated SERS substrates, the field enhancement has usually to be calculated numerically. Judith et al. give a comprehensive overview of several structures that provide near-field enhancement and hotspots through LSPs.^[72a] Besides the geometry and orientation of the nanoparticle, the enhancement depends on the excitation wavelength and polarization of the optical fields. Moreover, it strongly

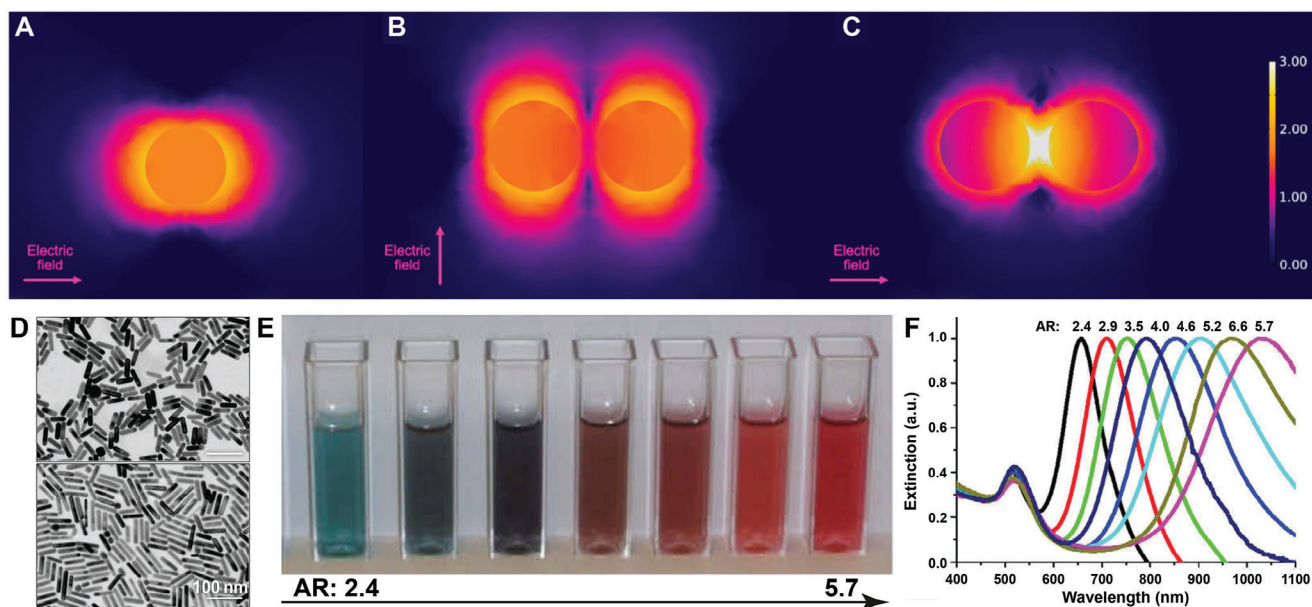


Figure 10. Interaction between light and nanostructures. A) Local field enhancement in 10 nm Ag nanoparticles as a monomer, and B,C) dimer depending on the direction of the external electric field being B) perpendicular and C) parallel to the dimer axis. Reproduced with permission from [96] Copyright 2022, American Chemical Society. D-F) The optical properties of Au nanorods change with aspect ratio. D) TEM images of Au nanorods. E) The color change is due to a redshift of the longitudinal LSPR, shown in (F). F) Corresponding optical response due to absorption and scattering of these structures. Panel D-F was reproduced under the terms of the Creative Commons CC-BY-NC-ND 3.0 License. [95] Copyright 2010, The Authors. Published by Elsevier B.V. on behalf of Cairo University.

depends on the size of the involved nanostructures, which is in line with the observation that polarizability depends on the volume of the employed nanoparticles. Figure 10D–F shows an example of Au nanorods with varying aspect ratios, i.e., increasing length. [95] The larger the longitudinal axis, i.e., the aspect ratio of the particles, gets, the more the longitudinal LSP resonance will shift to longer wavelengths. This is seen as a color change from cyan toward berry red (Figure 10E) and a shift of the extinction maximum from the visible to the infrared spectral region (Figure 10F). The optical response of the nanostructure decides how well the LSP can couple to the electric field of an external excitation source, leading to a local enhancement.

When applied for surface-enhanced Raman scattering, the enhancement process of the Raman scattered light is two-fold: in the first step, the field enhancement by the LSP applies to the field of the exciting laser at the angular frequency ω_p , leading to an enhanced excitation of molecular structures in proximity to the hotspots. In the next step, the field of the Raman scattered light at the Stokes- or anti-Stokes side at the frequency $\omega_p \pm \Omega$ will be enhanced. Since the vibrational shift, $\Delta\omega = \omega_p \pm \Omega$ is small compared to the line width of the LSP mode, the total enhancement factor EF simplifies to [84b]

$$EF = \left| \frac{E_{loc}(\omega_p)}{E_0(\omega_p)} \right|^2 \left| \frac{E_{loc}(\omega_p - \Omega)}{E_0(\omega_p - \Omega)} \right|^2 = \left| \frac{E_{loc}(\omega_p - \Omega)}{E_0(\omega_p)} \right|^4 \quad (26)$$

where E_{Loc} is the field at the Raman active site, and E_0 is the field without enhancement. The measured SERS signal is linked to the spontaneous Raman intensity via the enhancement factor di-

vided by the ratio between the number of molecules in the Raman and SERS experiment and reads as

$$I_{SERS} = \frac{EF}{N_{RS}/N_{SERS}} \cdot I_{Raman} \quad (27)$$

SERS with MOFs: SERS surfaces, or nanoparticles, are usually made of gold, silver, or copper. [97] SERS requires a close proximity of the analyte to the metal surface/hotspot. Hence, the poor affinity and/or selectivity between the metal substrates and many analytes drive the constant development of new SERS substrates and composite materials. [66] In the past years, metal-organic frameworks have shown to be a promising material for SERS applications due to their high affinity and selectivity to specific analytes that are adsorbed onto or inside the MOF. Even though some MOFs provide chemical SERS enhancement, [98] most MOFs are SERS-inactive. [66] The major strategy is to combine plasmonic nanoparticles (PNPs) directly with MOFs. There are three approaches to achieve electromagnetic enhancement for the SERS signal (Figure 11): 1) PNPs are embedded on the MOF surface, [62c,99] or a thin MOF film is grown on 2) a SERS active metal surface [100] or 3) around SERS active NPs. [29f,101]

2.2.3. Tip Enhanced Raman Scattering (TERS)

Since the discovery of SERS in the mid-1970s, [43] many other surface-enhanced Raman techniques have been implemented that are summarized nowadays under the term plasmon-enhanced Raman spectroscopy (PERS). One development path is the combination of different enhancement mechanisms,

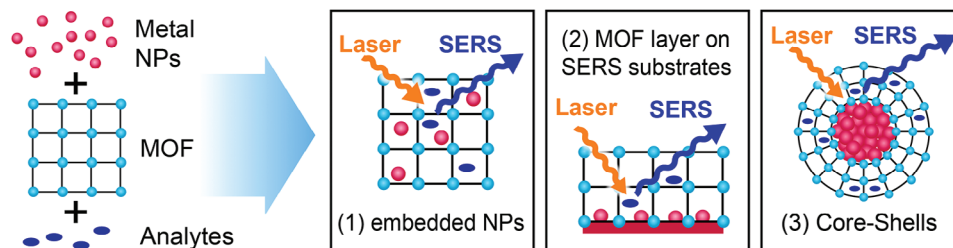


Figure 11. Strategies for enhancing the sensitivity of SERS by MOFs. Metallic nanoparticles (red), responsible for sensing of analytes (dark blue,) are combined with MOFs via three strategies: 1) they are embedded inside MOFs during the synthesis, 2) MOFs are used as a coating on SERS substrates or aggregated nanoparticles, 3) nanoparticles are incorporated inside MOFs as core-shell structures. Please note that the schematic drawing is not to scale. Large enhancement is usually observed for ≈ 50 nm full Ag particles,^[102] which are – by far – larger than the pore size of the MOF.

leading, for instance, to RRS/SERS as UV-SERS,^[103] NIR-SERS,^[104] or surface-enhanced nonlinear Raman spectroscopic techniques.^[105] The other strategy is to further extend the application of SERS beyond conventional substrates, aiming to separate their dimensions, enhancement, and achievable resolution. This goal can be reached by manipulating near-field enhancement to improve spatial resolution or by optimizing the distance between analytes and the enhancing surface, achieved through silica or aluminum coatings for signal improvement (SHINERS; shell-isolated nanoparticle-enhanced Raman spectroscopy). The invention of tip-enhanced Raman spectroscopy (TERS) at the beginning of the 2000s was a breakthrough concerning spatial resolution and its general applicability to substrates and surfaces.^[53c,106] The spatial resolution of optical microscopy is limited by the Abbe limit, which predicts a spatial resolution of ≈ 200 to 400 nm for excitation wavelengths in the visible range. TERS overcomes this limitation. Here, the sample surface is scanned by a sharp tip, enabling the excitation of LSPs. The interaction with the laser leads to an enhancement of the near-field close to the tip (Figure 12) and consecutively to enhanced Raman scattering of molecules close by. The resolution of TERS is not limited anymore by diffraction but by the decay of the near-field enhancement and, hence, the size and shape of the metal tip. Routinely, TERS enables chemically sensitive surface scanning with 20 to 30 nm resolution and a signal enhancement of ≈ 6 orders of magnitude.^[107] When matching the resonance of the nanocav-

ity in low temperature and ultra-high vacuum conditions, even sub-nm resolution can be archived.^[108]

2.2.4. Coherent Raman Scattering (CRS)

Coherent Raman scattering (CRS) is the third strategy for enhancing the signal of Raman processes. CRS comprises several nonlinear Raman approaches relying on the light-matter interaction between the sample and at least two high-intensity lasers. The term ‘coherent’ refers to the material response to light: the molecular signature oscillates in phase with the incident light. The frequency of two laser sources is chosen such that the coherent Raman excitation of the material $\Omega = \omega_1 - \omega_2$ matches the difference frequency of the two exciting fields (Figure 13A), which are driving the oscillation of the material. This interaction leads to a nonlinear response of the material, which generates new spectral signatures. The main processes, implemented today, are stimulated Raman scattering (SRS) and coherent anti-Stokes Raman scattering (CARS). Coherent Stokes scattering (CSRS), analog to CARS, is less frequently employed as its signature is red-shifted into the IR (Figure 13B). It is difficult to be detected by conventional silicon-based detectors. Stimulated Raman scattering leads to a signal change at the same wavelength as the incident light fields. It modulates the intensity of both light fields: the stronger pump pulse will decrease in intensity (Stimulated Raman Loss; SLR; Figure 13B), and the Stokes field will increase

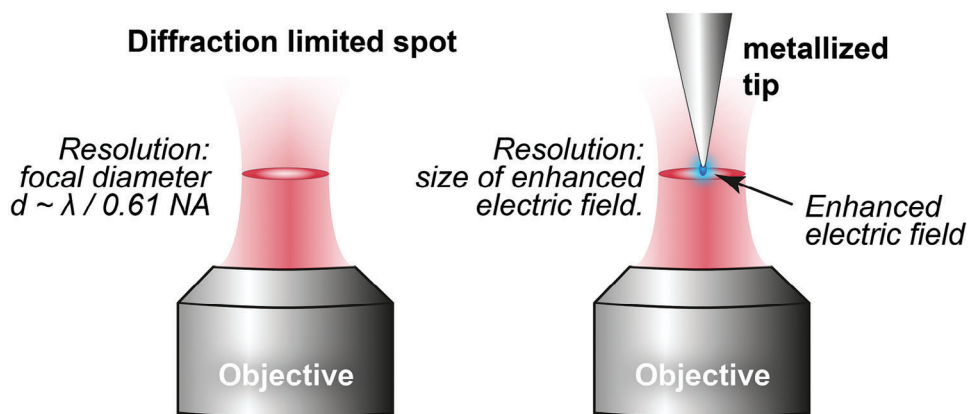


Figure 12. Field enhancement in TERS. (Left) The spatial resolution in conventional, far-field approaches is limited by the diffraction of light. The diameter of a focused laser source is ≈ 200 to 400 nm large. (Right) Light can couple to a metallized tip, leading to a strong near-field enhancement of the local electric field around the tip.

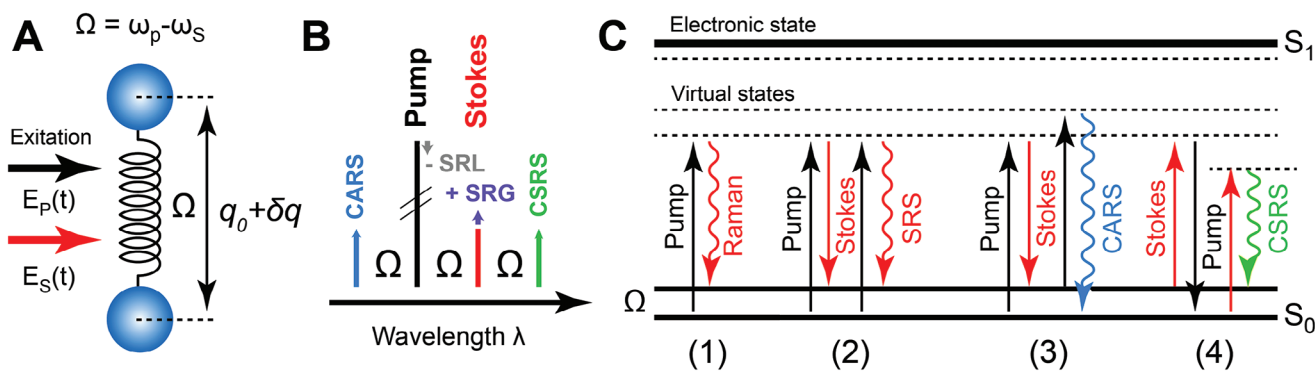


Figure 13. Coherent Raman processes are driven by at least two light fields. A) Classical description of a diatomic molecule excited by two incident light fields. The difference-frequency between both fields matches the molecular vibration Ω . B) Spectral position of the coherent Raman processes with respect to the incident light fields of the pump and Stokes laser. C) Jablonski energy diagram showing transitions involved during 1) spontaneous and 2) stimulated Raman scattering at the Stokes side, 3) coherent anti-Stokes Raman scattering, and 4) coherent Stokes Raman scattering.

(Stimulated Raman Gain; SRG). All four nonlinear Raman processes are physically four-wave mixing processes (Figure 13C), i.e., three electric fields interact with the sample, generating a fourth one (as discussed in the next sections). They provide elevated vibrational signals compared to the spontaneous scattering process and hence increased imaging speed or sensitivity, respectively. CRS microscopy and spectroscopy are established techniques for many areas, including live-cell imaging, biomedical research,^[109] material science,^[110] pharmaceutical,^[111] and environmental applications.^[64] A detailed description of developments in CRS microscopy is given in recent reviews.^[68d,e,72c,112]

Coherent Anti-Stokes Raman scattering (CARS): Coherent anti-Stokes Raman Scattering (CARS) is a nonlinear technique offering enhanced signal levels of up to 8 orders of magnitude compared to spontaneous Raman scattering.^[72b,113] A further advantage of CARS is its blue-shifted signature compared to the incident light fields, which allows for separating its signal from the spurious background due to fluorescence and scattering, for example, by conventional dichroic filters. CARS was introduced in 1965 by Terhune and Maker^[42] and was soon established as a spectroscopic technique for investigating chemical reactions during combustion.^[114] CARS imaging was pioneered by Duncan^[45] in 1982 and established by Zumbusch^[52c] in 1999 when combining confocal microscopy with collinear laser excitation. This seminal work triggered the rapid development of different technologies over the last two decades, e.g., based on polarization, frequency modulation, or spectral mixing to extract pure Raman signature from CARS at video-rate (20 frames per second) imaging speed.^[115]

CARS is a nonlinear optical process of third order and can be treated as a special case of four-wave mixing (FWM). It is a passive, nonlinear process with no energy deposition in the material. The initial and final states after the interaction are identical. CARS relies on the interaction with three light fields: the pump pulse at ω_p , the Stokes pulse at ω_s , and the probe pulse ω_{pr} . The first interaction with the pump laser (Figure 14; Ex. 1) together with the Stokes laser leads to a coherent excitation of the material. The third interaction with the probe laser stimulates the emission of the CARS field (Figure 14; Ex. 1). The enhancement of the Raman process results from the resonant, coherent excitation of the sample Ω that coincides with the difference frequency be-

tween the pump and Stokes field. Although the probe field allows for tuning the spectral range at which the CARS process occurs, CARS is frequently implemented as degenerated CARS, relying only on two lasers (Figure 14; Ex. 2). This is often the case for CARS microscopy when two light fields are coupled collinearly into the microscope.

CARS can be seen as a resonant FWM process mediated by the third-order nonlinear susceptibility of the medium. While CARS shows a signal enhancement, if the difference frequency between the pump and Stokes field matches a vibrational transition, the frequency-mixing process also occurs if there is no molecular resonance (Figure 14, Ex. 3). These FWM processes lead to the so-called non-resonant background, which alters the spectral signature compared to spontaneous Raman scattering, which we will discuss at the end of this section.

As described for spontaneous Raman, the interaction between light and the material leads to a time-dependent polarization $\tilde{P}(t) = \epsilon_0 \chi \tilde{E}(t)$ of the medium. For CARS, three light sources with strong electric fields are in place. To understand the nonlinear response of the material in the presence of an intense electric field $\tilde{E} = \tilde{E}_p + \tilde{E}_{pr} + \tilde{E}_s$ composed by the three incident light fields (Figure 14, Ex. 1), we describe the polarization as a function of the electric field via a Taylor expansion^[67]

$$\tilde{P} = \epsilon_0 \chi^{(1)} \tilde{E} + \epsilon_0 \cdot (\chi^{(2)} \tilde{E} \tilde{E} + \chi^{(3)} \tilde{E} \tilde{E} \tilde{E} + \dots) = \tilde{P}_L + \tilde{P}_{NL} \quad (28)$$

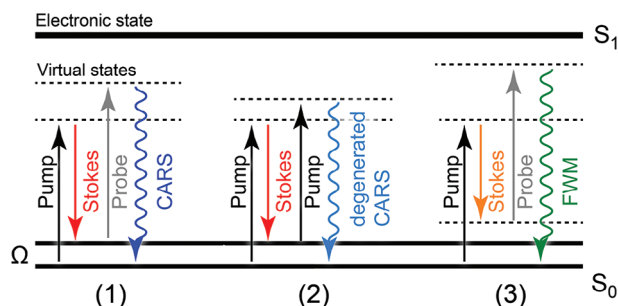


Figure 14. Energy diagram. Schematic energy diagram for 1) CARS, 2) degenerate CARS, and 3) FWM. Virtual states are depicted as dashed lines. Solid lines represent electronic or vibrational states. The electronic ground state and first excited state are denoted S_0 and S_1 .

with $\chi^{(n)}$ being the electric susceptibility tensor of the n^{th} order. ϵ_0 denotes the dielectric constant, and \tilde{P}_L and \tilde{P}_{NL} are the linear and nonlinear contributions to the polarization, respectively. FWM and CARS are third-order effects and are described by the $\chi^{(3)}$ term, i.e., $\chi^{(2)}$ does not contribute. We assume that the electric fields of the three laser pulses $i \in \{P; Pr; S\}$ are plain waves $\tilde{E}_i(z, t) = E(\omega_i) \cos(\omega_i t - k_i z)$ with wave vector \vec{k}_i and frequency ω_i , that propagate in the Z-direction. All light fields exhibit a constant amplitude $E(\omega_i)$ and are linearly polarized in the X-direction. The time-dependent nonlinear polarization \tilde{P}_{NL} responsible for CARS at position z and frequency $\omega_{CARS} = \omega_p - \omega_s$ + ω_{Pr} can be expressed as

$$\tilde{P}_{NL}^{(3)}(z, t) = \frac{1}{2} \left\{ \epsilon_0 \chi^{(3)}(-\omega_{CARS}; \omega_p, -\omega_s, \omega_{Pr}) E_p(\omega_p) E_s^*(\omega_s) E_{Pr}(\omega_{Pr}) \right. \\ \left. \times \exp [i(k_p - k_s + k_{Pr})z - i\omega_{CARS}t] + c.c. \right\} \quad (29)$$

Here, the notation for the nonlinear susceptibility $\chi^{(3)}(-\omega_{CARS}; \omega_p, -\omega_s, \omega_{Pr})$ indicates the interaction order of the laser fields with the sample from left to right, i.e., the pump pulse interacted first with the medium, followed by the Stokes and probe field to induce the light field at ω_{CARS} . The negative sign at the Stokes frequency, as well as the complex conjugated notation for the Stokes field, take into account that quantum-mechanically the Stokes field releases energy while interacting with the medium (Figure 14). The new electric field can be obtained by solving the nonlinear wave equation^[67]

$$\left\{ \nabla^2 - \left(\frac{n}{c} \right)^2 \frac{\partial^2}{\partial t^2} - \frac{\alpha \cdot n}{c} \frac{\partial}{\partial t} \right\} \tilde{E}_{CARS}(z, t) = \frac{1}{c^2 \epsilon_0} \frac{\partial^2 \tilde{P}_{NL}^{(3)}(z, t)}{\partial t^2} \quad (30)$$

where c denotes the speed of light, n is the refractive index, and α the absorption coefficient of the sample. Equation 30 identifies the induced, nonlinear polarization of 3rd order $P_{NL}^{(3)}$ as the source responsible for generating the electric field E_{CARS} of the CARS signal. It is a differential equation of 2nd order, which can be reduced to first order under a slowly varying envelope approximation of the electric field. For linearly polarized laser fields that travel in the Z-direction, the nonlinear wave equation reduces to

$$\left(\frac{\partial}{\partial z} + \frac{n_{CARS}}{c} \frac{\partial}{\partial t} \right) E_{CARS}(z, t) = \frac{i}{2\epsilon_0 c} \frac{\omega_{CARS}}{n_{CARS}} P_{CARS}^{(3)} e^{-ik_{CARS}z} \quad (31)$$

By solving Equation 31, we obtain the measured CARS intensity, which relates to the square of the electric field $I_{CARS} \propto |E_{CARS}|^2$. It is, therefore, proportional to

$$I_{CARS} \propto |E_{CARS}|^2 = \left(\frac{\omega_{CARS}}{c n_{CARS}} \right)^2 \cdot \left| \chi^{(3)}(\omega_{CARS}) \right|^2 \cdot I_p I_s I_{Pr} \cdot L^2 \\ \cdot \left(\frac{\sin(\Delta k L / 2)}{\Delta k L / 2} \right)^2 \quad (32)$$

The measured signal depends on the intensity of all three fields, the sample thickness L , the phase mismatch $\Delta \vec{k} = \vec{k}_p - \vec{k}_s + \vec{k}_{Pr} - \vec{k}_{CARS}$, and quadratically on the nonlinear susceptibility and detection frequency ω_{CARS} . For degenerated CARS ($\omega_p = \omega_{Pr}$), the measured signal scales quadratically with the intensity

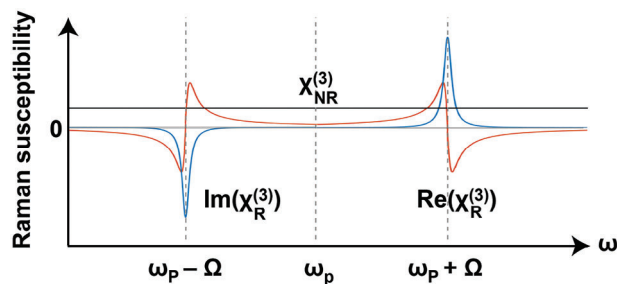


Figure 15. Contributions to the nonlinear susceptibility $\chi^{(3)}$. The nonlinear susceptibility $\chi^{(3)}$ is a complex quantity with three contributions: 1) a constant, non-resonant term which is real, and a frequency-dependent, resonant term which is complex. The real part of 2) the resonant contribution is responsible for a dispersive line shape, while the imaginary part 3) encodes the Lorentzian shape.

of the pump pulse. While the phase mismatch leads to a space-dependent signal modulation due to destructive interference in the context of CARS spectroscopy, it plays no significant role in CARS microscopy due to the short interaction length in the sample of a few micrometers. To summarize, CARS is observed at $\omega_{CARS} = \omega_p - \omega_s + \omega_{Pr}$ for intense laser fields. If the frequency difference $\omega_p - \omega_s$ matches the frequency of a Raman active vibration of the sample (Figure 14), the signal will be significantly enhanced (similar to RRS, however, without the need for an electronic resonance) while contributions due to four-wave mixing occur at the same time. Why is that?

The material-specific nonlinear susceptibility $\chi^{(3)}$ depends on two terms: a resonant and non-resonant contribution.

$$\chi^{(3)} = \chi_R^{(3)} + \chi_{NR}^{(3)} \quad (33)$$

The non-resonant part is real and approximately constant (Figure 15).^[67] The resonant nonlinear susceptibility $\chi_R^{(3)}$ is frequency-dependent and directly proportional to the Raman cross section σ and the number of excited molecules N .^[67] It is maximal at frequencies that coincide with vibrational transitions Ω of the sample and zero elsewhere.^[67] For a heterogeneous sample, the resonant nonlinear susceptibility is a superposition of response functions for each molecular species i with a vibrational transition Ω_i close by

$$\chi_R^{(3)}(\omega) = \sum_i \frac{N_i \sigma_i}{\omega - \Omega_i - i\Gamma_i} \quad (34)$$

Here, N_i denote the number of Raman active scatterers, i.e., the concentration, σ_i the Raman cross-section of the molecule, and Γ_i the linewidth of specific vibrational transition. While the imaginary part describes the Lorentzian profile of vibrational transitions, the real part is responsible for dispersive line shapes. The quadratic dependence of the CARS signal of the intensity on $\chi^{(3)}$

$$I_{CARS} \propto \left| \chi^{(3)}(\omega_{CARS}) \right|^2 = \left| \chi_R^{(3)} + \chi_{NR}^{(3)} \right|^2 \\ = \left| \chi_R^{(3)} \right|^2 + \left| \chi_{NR}^{(3)} \right|^2 + 2\chi_{NR}^{(3)} \Re \left(\chi_R^{(3)} \right) \quad (35)$$

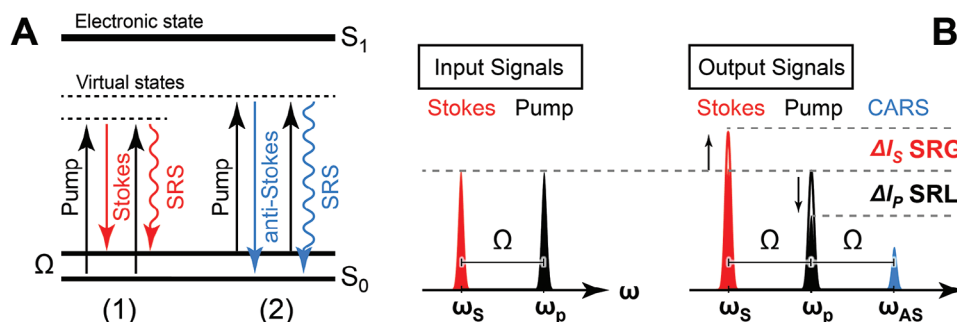


Figure 16. Stimulated Raman Scattering. A) Jablonski energy diagram of the (1) Stimulated Stokes Scattering and (2) inverse anti-Stokes scattering. B) Measurement scheme of Stimulated Raman Gain (SRG) and Loss (SRL) of the pump and Stokes pulse.

mixes the contributions due to enhanced Raman (resonant term) with an unspecific, non-resonant background due to FWM, leading to dispersive interference. CARS spectra, therefore, exhibit strongly distorted non-Lorentzian line shapes in contrast to spontaneous Raman scattering. Together with the quadratic dependence on the concentration, this property hampers quantitative measurements with CARS in multi-component systems. By exploiting the physical dependencies of the resonant and non-resonant contribution, different methods have been developed based on polarization, directionality of the signals, frequency modulation, or spectral mixing to extract pure Raman signatures from CARS.^[115]

Stimulated Raman Scattering (SRS): Stimulated Raman scattering (SRS) is experimentally observed in two forms, as Stimulated Raman Loss (SRL) or as Stimulated Raman Gain (SRG), although both observations have the same underlying mechanism. SRS was discovered in 1962.^[40] Its working principle was theoretically investigated in the early 1960s,^[41a] and summarized in several reviews of the 1970s.^[41b,67a] In 1999, the Yoshizawa group introduced SRS for time-resolved experiments.^[52b] Its application in microscopy was first published in 2007.^[59a-c] Like CARS, stimulated Raman scattering overcomes limitations of spontaneous Raman scattering by providing enhanced signal levels of up to 7–8 orders of magnitude.^[110b,116]

SRS is a third-order nonlinear optical process. It is an active process in which energy is exchanged with the material, i.e., the initial and final states differ after the interaction. SRS relies on the interaction with three electric fields, usually derived from two laser fields: the pump pulse at ω_p and the Stokes pulse at ω_s . Analog to CARS, the SRS process can be treated as a four-wave mixing process. The first interaction with the pump laser (Figure 16A; Process 1) and the Stokes laser leads to a coherent excitation of the material, which can decay with a dephasing time τ_2 on the picosecond time scale. If the third interaction comes immediately after the coherent excitation, the pump laser will stimulate the molecule to emit a Stokes photon. The enhancement of the Raman process results from the resonant excitation of a vibrational transition Ω in the sample that coincides with the difference frequency between the pump and Stokes field $\omega_p - \omega_s$. During SRS, energy is transferred from the pump beam to the Stokes beam, leading to a measurable Stimulated Raman Gain (SRG) of the Stokes intensity, while the energy of the pump is decreased, resulting in a Stimulated Raman Loss (SRL) of the pump intensity.^[59b,117] The SRS signal can be, therefore, either derived

from the change of the pump or the Stokes field. When measuring on the anti-Stokes side (Figure 16A, Process 2), referred to the pump pulse ω_p , SRS leads to a decrease of the anti-Stokes field and an increase in the red-shifted pump field. During SRS, energy is always transferred from the beam at a higher frequency to the red-shifted beam at a lower frequency.

Experimentally, SRS is measured by exciting the sample with two co-aligned lasers providing the pump and Stokes pulses (cf. Figure 25). SRS takes place 1) if both pulses overlap at the sample in time and space and 2) if the difference frequency of both lasers matches a vibrational transition in the sample Ω (Figure 16B). By turning the pump beam ‘on’ or ‘off’ by an acousto-optic device, the intensity of the Stokes laser source can be monitored in the absence and presence of the pump beam over time. Using de-modulation techniques based on a photodiode and a Lock-In amplifier, as we will see in the instrumentation section, the SRS-induced signal change can be extracted and recorded as a function of space (microscopy), or as a function of time (spectroscopy). The change of the Stokes field ΔE_S is

$$\Delta E_S = -i \frac{3\omega_S}{4cn_S} \chi^{(3)} |E_P|^2 E_S L \quad (36)$$

where L is the interaction length of the Raman active medium, E_S and E_P the electric fields of the two laser pulses, c being the speed of light, and n_S the refractive index at the frequency ω_S . The SRS signal can be derived as the difference signal between Stokes intensity in the presence and absence of the pump pulse

$$\Delta I_S(\omega_p - \omega_s) \propto |E_S + \Delta E_S|^2 - |E_S|^2 = |E_S|^2 + 2E_S \Re(\Delta E_S) + |\Delta E_S|^2 - |E_S|^2 \quad (37)$$

Since the third term vanishes compared to all other terms, the measured Stimulated Raman Gain reads as

$$\Delta I_S(\omega_p - \omega_s) \propto 2E_S \Re(\Delta E_S) = \frac{3\omega_S}{4cn_S} \Im m(\chi^{(3)}(\omega_p - \omega_s)) I_P I_S L \quad (38)$$

It scales linearly with the laser intensities, the sample thickness L , and only with the imaginary part of the nonlinear susceptibility $\chi^{(3)}$. Why is this advantageous? This term describes the Lorentzian-shaped contribution of the nonlinear susceptibility responsible for the sharp line shape of Raman transitions. The inherent SRS signal is background-free^[118] and does not depend on

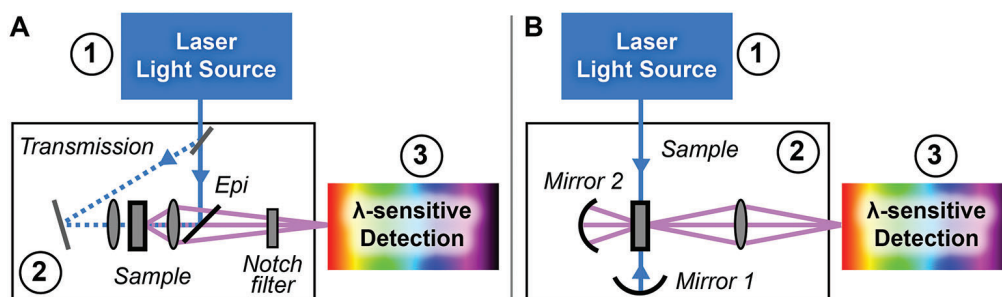


Figure 17. The Instrumentation required for Raman spectroscopy. All Raman techniques rely on three major units: 1) the excitation light source, 2) the optical instrument, e.g., a microscope or a sample unit including optics to focus the light onto the sample and to collect the Raman scattered light and 3) a detection unit, which allows for recording the Raman signature in a spectrally resolved manner. A-B) The detection geometry for spontaneous Raman spectroscopy, for instance, can be either A) under 0 and 180 degrees, i.e., in the forward direction through the sample or in back-reflection (epi-direction), or B) under 90 degrees. The exciting and scattered light are depicted in blue and purple, respectively.

any unspecific non-resonant and real background. It matches the one of spontaneous Raman spectra. The SRS signal scales also linearly with the sample concentration c and Raman cross section σ (described by the nonlinear susceptibility; cf. Equation 34). Hence, SRS can be utilized for fast quantitative chemically sensitive measurements at low concentrations of the analyte, with relative change in intensity that can be measured down to a range of 10^{-8} .^[68d,110b]

3. Instrumentation

Raman spectroscopy has been implemented in several approaches, differing in the measurement mode (transient/in operando/in situ), their spatial resolution (bulk spectroscopy, microscopy, nearfield microscopy), detection (single color detection, broadband detection in the time and frequency regime), detection geometry (transmission, back-reflection and under 90 degree) and lastly their enhancement strategies (RRS, SERS/TERS, CRS and combinations thereof). Despite the large variety of Raman methodologies available, the instrumentation of every Raman system relies on three modules (**Figure 17**): it consists of 1) an excitation light source (nowadays a laser system), 2) a sample unit, such as a microscope, including optics for the excitation of the sample and collection of Raman scattered light and 3) a detection unit which monitors the Raman signature from the sample. Additionally, optical filters are in place in the excitation and detection path for spectral narrowing the excitation and for optically blocking a Rayleigh scattering, respectively. Polarization optics are added accessorially in the excitation as well as in the detection path to probe for polarization selection rules or Raman optical activity. The following section aims to give an overview of the required instrumentations, technical realizations, and measurement modes that are possible based on Raman scattering.

3.1. Light Sources

While setups for spontaneous Raman scattering, RRS, SERS, and TERS usually employ continuous wave (CW) lasers in the visible range, nonlinear Raman techniques require high-power laser

sources, such as fs- and ps- pulsed lasers in the near-IR range. For time-gated Raman spectroscopy in the ps-ns regime, pulsed solid-state lasers, for instance, based on Nd:YVO (532 nm) or Nd:YAG (1064 nm) find application, but these are more used for custom setups rather than for routine measurements.

3.1.1. CW Laser Sources

Spontaneous Raman spectroscopy requires a high-power, monochromatic light source. While mercury arc lamps were still in place until the 1960s,^[119] they were quickly replaced by laser sources in the late 1960s due to their coherence, high stability, higher intensity, and low divergence.^[120] At first, gas lasers, like helium-neon (He-Ne; 632.8 nm), Krypton (530.9 nm), or Argon ion lasers (488 and 514.5 nm), were implemented due to their intrinsically narrow excitation bandwidth of 0.001 nm, i.e., $< 0.5 \text{ cm}^{-1}$. These lasers feature a Gaussian beam profile (TEM₀₀ mode) and support a diffraction-limited confocal volume when being focused on the sample. However, more economic solid-state and diode lasers in combination with 10 cm^{-1} band-pass filters have been used in commercial setups lately. Their non-gaussian-shaped beam profile is cleaned up by coupling the laser into the microscopes via optical fibers using the fiber entrance as pinhole. Besides the spectral and spatial resolution, a further benefit of these laser sources is their frequency stability. Although spectral shifting occurs with temperature and applied current, frequency-stable lasers ($< 0.01 \text{ cm}^{-1}$) are available, for probing strain and stress in materials. They further possess a fixed polarization and stable intensity ($< 1\% \text{ RMS}$) that enables polarization-dependent and quantitative concentration measurements. Lastly, the choice of laser wavelength depends on the required application and sample. While lower wavelengths in the UV-Vis can be beneficial for RRS and SERS measurements, they often induce photoluminescence that interferes with the Raman signature itself. For MOFs, wavelengths in the visible to NIR range might be more suitable for studying organic linkers and composite materials. Hence, Raman spectroscopy is often performed at 633 nm and 785 nm as a compromise between signal strength (which is inversely proportional to the the wavelength to the fourth power), minimized background, and adequate sensitivity of silicon-based detection systems.

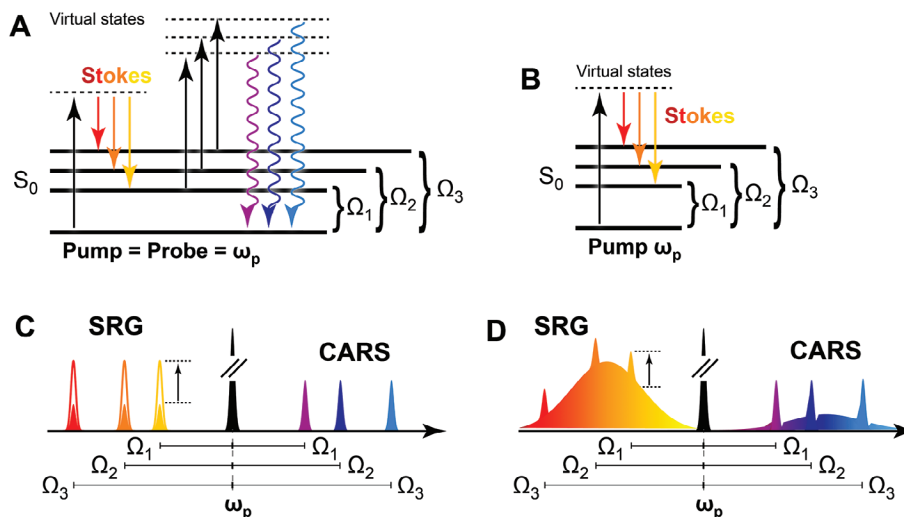


Figure 18. Excitation schemes for Coherent Raman Scattering. Single-frequency CRS microscopy based on a fixed pump pulse and a tunable Stokes pulse. By tuning the Stokes wavelength, all Raman resonances Ω_i of the material can be addressed either via A) single-frequency CARS or B) as single-frequency SRS. C) Single-frequency CRS is detected as a blue-shifted signal on the anti-Stokes side due to CARS. SRS can be monitored as a gain in the intensity of the Stokes pulse or loss of the pump pulse. D) When using broadband laser pulses as Stokes pulse, all Raman resonances can be excited at once via CRS.

3.1.2. Pulsed Laser Sources for Nonlinear Raman Approaches

Coherent Raman scattering mainly relies on ultrashort fs- or ps-laser pulses with high energy densities to generate nonlinear processes. There are two approaches when using CRS: 1) Single-frequency CRS and 2) broadband CRS spectroscopy or microscopy. In the first configuration, one specific vibration is analyzed in time, frequency, or space, while in the second configuration, the entire spectrum of the sample is examined at once. Single-frequency coherent Raman scattering (CRS) is commonly combined with microscopes to monitor the spatial distribution of a species with distinct spectral characteristics. When dealing with samples exhibiting unknown behavior over time, e.g., during chemical reactions, or in terms of their chemical composition and distribution in space, broadband approaches are used. If only single-frequency CRS is available, at least one of the lasers has to be tuned to record a spectrum or to address multiple vibrational transitions in the same sample. Both approaches employ pulsed light sources in the NIR range between 700–1200 nm, to minimize photodamage.^[121] Nonetheless, setups operating in the UV–Visible range have also been developed.^[122] Their laser power at the sample varies between 5 to 50 mW depending on the material.

Single-frequency CRS microscopy employs at least two synchronized laser pulses (pump and Stokes pulses for degenerated CRS). The frequency of the first light source is typically fixed, while the second light source is spectrally broad or tunable. (Figure 18A,B). Why is this? For a fixed pump laser, e.g., in the NIR at 780 nm, and a spectrally narrow Stokes laser, the wavelength of the Stokes pulse has to be adjustable between 810 and 1130 nm to address vibrational transitions between 500 and 4000 cm^{-1} given by their difference frequency $\omega_p - \omega_s$. In this scenario, single Raman transitions Ω of the material are selected by tuning the Stokes laser to the corresponding wavelength in resonance. For single-frequency CRS, both laser pulses should

have a transform-limited pulse duration of 1–2 ps, matching the bandwidth of a vibrational transition on the order of 10 cm^{-1} (Figure 18C). For imaging, the pulse repetition rate is around 10–100 MHz to provide maximal acquisition speed at minimal dwell time for a pixel. For multiplex CRS spectroscopy applications, a repetition rate in the kHz regime is selected. Instead of tuning one of the lasers, spectrally broad fs-laser pulses allow for exciting all Raman resonances at once (Figure 18D). This approach requires either a broadband detection scheme (as discussed in Section 3.4.5) or pre-chirping, which involves temporal stretching of the broadband laser pulse. In this way, a limited temporal overlap between the pump pulse and a narrow spectral window of the broadband pulse is achieved. This enables targeting specific vibrational transitions and using point detectors, as in the case of single-frequency CRS. The technical requirements of the pulsed laser sources make CRS technically more challenging compared to spontaneous Raman scattering, RRS or SERS. Yet, CRS techniques allow for Raman experiments at enhanced signal levels with fast acquisition at higher sensitivity as required for monitoring chemical reactions. Further details on the principles and instrumentations of CRS can be found elsewhere.^[68d,g,72c,112c,123]

3.2. Setups

Depending on the desired spatial resolution, there are three different configurations for the sample unit. 1) Conventional Raman spectroscopy on bulk or powder samples that are carried out on commercial setups provides a relatively low spatial resolution of $<1 \text{ mm}^2$ (‘Macro’-Raman; Section 3.2.1). 2) ‘Micro’-Raman setups with sub- μm resolution are in place for studying single MOF crystals with adiameter down to about 500 nm.^[64a] While there are several methodologies implemented, all systems rely on diffraction-limited optical microscopes (Section 3.2.2). 3) For Raman measurement with spatial resolutions below 500 nm, TERS

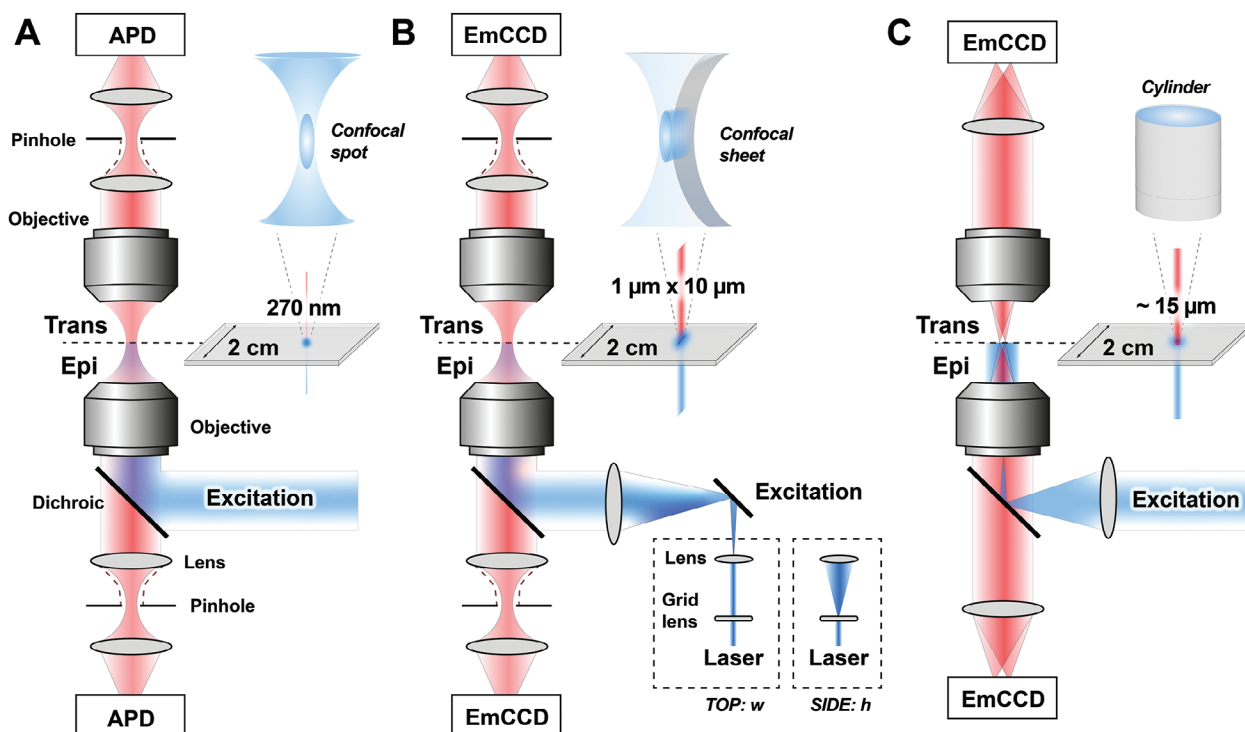


Figure 19. Common microscopes employed for Micro-Raman spectroscopy. Schematics of setups with detection in transmission or back-reflection (epi). A) Confocal microscope with point excitation. Pinholes remove any out-of-focus light in the detection pathway. The laser excitation is Gaussian-shaped and focused on a diffraction-limited spot on the sample/the coverslide (as shown in the inset). For a given objective (NA 1.27) and laser excitation at 532 nm, the spatial lateral resolution is ≈ 270 nm. B) Confocal microscope with line excitation. The laser excitation was given an ellipsoidal beam profile using a special lens (grid, cylindrical, Powell), which results in a line focus, i.e., a confocal excitation sheet, as shown in the inset. The line dimensions are on the order of $1 \times 10 \mu\text{m}^2$. C) Schematics of a widefield microscope. The excitation light is focused onto the back focal plane of the objective to illuminate a wide area on the sample with a size of 10–20 μm .

microscopy comes into play. This scanning near-field technology uses a physical metal tip to confine the spectroscopically probed volume (Section 3.2.3). Routinely, lateral resolutions down to 20–30 nm have been reported.^[107,124]

3.2.1. Spectrophotometer

When measuring Raman scattering in bulk without any requirements for spatial resolution, mainly spectrophotometers are employed. These can be either stationary lab-based devices or portable (hand-held devices for field measurements). Time-dependent measurements, such as transient coherent Raman experiments or time-gated Raman experiments, are usually carried out on custom setups. All devices have in common that the laser excitation is focused onto the sample by lenses with longer working distance (>5 mm), leading to a probed sample area on the order of $<1 \text{ mm}^2$.

3.2.2. Microscopes

For measurements with sub-micron resolution, optical light microscopes are in place. They differ in the geometry of the excitation volume in which Raman scattering occurs and, hence, in the way, the scattered signal is detected. The most common ar-

angement for spontaneous as well as nonlinear Raman scattering is a confocal microscope, where the laser is focused down to a diffraction-limited spot or a line. Consecutively, scanning of the sample is carried out if spatial information is required. To probe the spectral signature within an area without scanning, widefield and light-sheet microscopes have been realized.^[125] For all types of setups, the lateral resolution is bound by the diffraction of light, i.e., given by the numerical aperture NA of the microscope objective and the selected excitation wavelength λ . By choosing an objective without immersion (0.6–0.8), a lateral resolution $d_{xy} = 0.61 \cdot \lambda/NA$ on the order of 0.5–1 μm can be easily achieved (for wavelengths between 488–1064 nm). Using high-NA objectives with water (1.27) or oil immersion (1.4), a lateral resolution between 200–300 nm is reachable in the visible range, yet, at the expense of potentially disturbing background contributions due to Raman scattering in the immersion fluid. The depth resolution or axial resolution $d_z = 2 \cdot \lambda/NA$ is less than 1 μm .

Confocal Scanning Microscope: Micro-Raman spectroscopy based on spontaneous Raman scattering, RRS, and SERS is commonly performed on confocal microscope setups for recording complete Raman spectra at the confocal volume. Similarly, setups for CRS imaging are predominantly built around confocal microscopes. Usually, the laser excitation is focused on the sample by a microscope objective as a point (Figure 19A). The size of the confocal volume is ≈ 200 –300 nm in the lateral direction

and $\approx 1 \mu\text{m}$ in the axial direction. The scattered light is collected either via the focusing microscope objective in back-reflection (epi-mode) or via a condenser lens in transmission. In both configurations, only scattered light that originates from the confocal volume will be collected via the objective. In the case of MOF samples, which are not transparent, the back-scattered light is typically collected using the same objective used for excitation. Excitation and scattered light are spectrally separated afterward by a dichroic mirror. Next, the scattered light is filtered to eliminate Rayleigh scattering and background via a Notch filter, and its distinctive signature is recorded after the pinhole either via a spectrometer in combination with a detector array or via point detectors like avalanche photodiodes (APDs) in combination with a Michelson-interferometer in FT-Raman setup (Section 3.3.3).

A confocal configuration enables the recording of Raman spectra with sub-micrometer resolution in situ. For spatial information, scanning of the sample or the light source is required. During image acquisition, the sample can be moved using a piezo-stage while the laser excitation remains static, or the laser beam can be scanned over the stationary sample using galvanometric mirrors. The image is reconstructed afterward from the hyperspectral data cube by chemometric methods, or by univariate data analysis, i.e., the spatial representation of single vibrational transitions. The biggest downside of a confocal scanning microscope is the long-lasting data acquisition. The data acquisition can last several hours to even days in the case of spontaneous Raman scattering, depending on the desired size and resolution of a raster-scanned image. To increase the data acquisition speed, the laser light is often focused as a line onto the sample (Figure 19B), e.g., through a grid lens, cylindrical lens, or Powell lens.^[126] In this arrangement, sample areas along that line on the sample are simultaneously excited. The scattered light is detected afterward on a line-detector (single wavelength) or 2D detector like an electron multiplying Charge-Coupled Device (emCCD) camera (Section 3.3.1), which decodes the spectral information as a function of position.

Widefield Microscope: Widefield microscopes are another possibility to increase the data acquisition speed (Figure 19C). Here, a micron-sized area of the sample is illuminated. The scattered light from different points in the illuminated area is measured afterward via a detector array (e.g., a CCD camera) simultaneously. No scanning is required. The data acquisition of the camera could be easily on the ms-time scale. It only depends on the measured signal strength. The spatial resolution for widefield imaging is also $\approx 250\text{--}300 \text{ nm}$ in the visible range. A potential downside of this approach is the lack of spectral information when exciting with a CW laser since the CCD camera only measures the intensity at different pixels without wavelength separation. To get spectral information, a combination of suitable bandpass filters is commonly used for probing one specific Raman transition on the camera. A more advanced way is tunable filters that measure the intensity at different wavelengths successively.^[125a-c] Alternatively, one can also use a static filter and a tunable laser for excitation^[125f] since the absolute wavelength of the Raman scattered light shifts with the laser wavelength (cf. Equation 1). Lastly, one can use an array of optical fibers instead of a single CCD camera, where each fiber is connected to a spectrometer and detector separately.^[125d,e] Here, one spectrometer records the spectra of multiple fibers, i.e., of multiple pixels, simultaneously. While

spectra information of the detected light is separated horizontally by the grating, light by different fibers can be stacked in the second dimension and detected together on a single CCD camera. Widefield microscopy is primarily applied for spontaneous Raman RRS and SERS.^[127] Nevertheless, the feasibility of wide-field CARS was shown despite the inconveniently high power densities.^[128]

3.2.3. Nearfield Microscope: Tip-Enhanced Setups

To probe Raman scattering at the nanometer regime, SERS is coupled with a scanning microscope for realizing tip-enhanced Raman scattering (TERS) as a nearfield scanning probe method. Here, the plasmon resonance located at the apex of a noble metal scanning tip is utilized to probe the surface and to enhance the Raman signal, which is detected afterward via an optical microscope (Figure 20A). Because of the fast decay of the field enhancement in the tip, TERS is sensitive to the sample surface and allows for imaging samples in 2D. The three most frequently used configurations to keep the tip close to the sample surface are based on Atomic Force Microscopy (AFM), Shear Force Microscopy (SFM), and Scanning Tunneling Microscopy (STM; Figure 20B–D),^[129] all of which are well-established techniques in independent microscopes. The sample then is moved with a piezo stage to scan the illuminated tip over the sample. The TERS instrumentation is described in more detail in.^[107,129]

3.3. Detection

There are various methods available for recording the spectral signature of Raman scattering processes, which can be classified into five different detection schemes. The first consideration is whether the entire Raman spectrum is captured simultaneously or if only a single Raman resonance is targeted. This differentiation determines whether a point detector or a line detector will be employed. The second aspect to consider is the signal strength of the different types of Raman scattering. This plays a crucial role in selecting a suitable detector with the required sensitivity. Different types of detectors, such as photomultiplier tubes or charge-coupled devices (CCDs), can be chosen based on the Raman signal. The third consideration involves the requirement for wavelength sensitivity, i.e., the ability to differentiate spectral contributions. This guides the selection of the detection scheme, which can be dispersive or nondispersive. Dispersive approaches based on prisms or gratings spatially separate the spectral components, allowing for wavelength discrimination. On the other hand, interferometers, such as those used in Fourier Transform Raman spectroscopy, provide access to spectral information without the need for any dispersive element. The fourth aspect to consider is whether polarization optics are incorporated to examine Raman spectra in a polarization-dependent manner. By introducing polarization elements, researchers can gain insights, e.g., into the crystal orientation or depolarization ratio of Raman transitions. Lastly, the detection setup can include additional elements, such as Lock-In amplifiers, which enable synchronized detection of Raman scattering relative to the laser excitation of the sample. This facilitates time-resolved spectroscopy assays, allowing the

study of dynamic processes. By considering these different aspects, researchers can choose the appropriate detection scheme tailored to their specific experimental needs.

3.3.1. Detectors

Point Detectors: The advancement of Raman spectroscopy was strongly driven by the development of highly sensitive detectors like photomultiplier tubes (PMT), which revolutionized the recording of Raman spectra by replacing photographic documentation.^[120] In the early stages, point detectors such as thermoelectrically cooled PMTs and photodiodes (PD) were introduced to capture the signatures of single vibrational transitions. PMTs are known for their exceptional sensitivity and high quantum efficiencies of up to 80% due to the photo effect within a scintillating layer.^[130] When exposed to light, PMTs amplify the resulting electronic signal by up to 8 orders of magnitude,^[131] enabling the detection of weak signals. They are particularly well-suited for low-scattering samples and incoherent radiation, such as spontaneous Raman scattering. Photodiodes offer advantages over PMTs, including their compact size, lower cost, and the availability of array configurations that allow for simultaneous monitoring of multiple Raman transitions. Photodiodes are semiconductor detectors based on pn junctions. When light interacts with the photodiode, it excites minority charge carriers in the pn junction, resulting in a measurable current proportional to the number of photons detected. While photodiodes are generally less sensitive than PMTs (≈ 2 – 3 orders), they still offer sufficient sensitivity for Raman experiments with strong enhancement and are commonly used for stimulated Raman-based assays. To enhance the sensitivity of photodiodes further, avalanche photodiodes (APDs) represent an advanced detection system. APDs utilize more complex doping profiles of the semiconductor and a strong electric field to trigger a secondary ‘avalanche’ of electrons, significantly amplifying the signal. APDs achieve $\approx 50\%$ of the detection efficiency of PMTs over the visible and near-infrared (NIR) range. In addition to their higher sensitivity, APDs also offer faster response times on the nanosecond scale, making them well-suited for time-resolved measurements. They are commonly employed as point detectors in confocal microscopes. Overall, the choice between photodiodes, APDs, and PMTs depends on the specific requirements of the Raman experiment. While PMTs provide the highest sensitivity, photodiodes, and APDs offer cost-effective alternatives with sufficient sensitivity for many appli-

cations. APDs offer exceptional sensitivity, rapid response time, and suitability for time-resolved measurements.

Detector Arrays: The second group of detectors was developed for broadband detection. Charge-coupled device (CCD) sensors exist as one- and two-dimensional detector arrays. They consist of a doped layer of semiconducting material, typically p-doped silicon, and a thin layer of optically transparent but electronically insulating material on top. Gating electrodes connected to the insulating layer can create local ‘traps’ for electrons at the interface between the semiconductor and the isolator. By applying a positive gate voltage, electrons are accumulated within individual pixels during the integration time when exposed to light. Afterward, the accumulated electrons are read out, providing information about the intensity at each pixel. Electron multiplying CCDs (emCCDs) take the concept further by incorporating post-enhancement of light-induced charges within the sensor. This technology enables chip designs with pixel sizes typically in the range of a few micrometers in diameter.^[132] emCCDs exhibit high quantum efficiency, reaching over 90% in the visible range. They are particularly well-suited for applications that require sensitive detection for low-scattering samples. Silicon-based CCD detectors are commonly employed in conjunction with lasers operating in the visible to NIR range. However, for wavelengths beyond $1 \mu\text{m}$, semiconductor CCD detectors with low band-gap materials such as Germanium (Ge) or Indium-Gallium-Arsenic (InGaAs) are utilized. Time-gated experiments can be realized using detectors like time-resolved photomultiplier tubes, CCDs, as well as complementary metal-oxide semiconductor single-photon avalanche diodes (CMOS SPADs), as frequently used in time-resolved fluorescence measurements. SPADs are special APDs based on silicon that allow for counting single photons, where each photon-induced electron triggers an avalanche of $\approx 10^8$ electrons, hence its name. In combination with CMOS chips, these sensitive point detectors allow for recording full spectral or spatial information with sub-nanosecond time resolution.

3.3.2. Synchronization

For time-resolved and coherent Raman spectroscopy, synchronizing devices are essential to ensure accurate timing and synchronization between the laser excitation of the sample and the detection system. These devices help to record time-dependent Raman signatures and enable studying dynamic processes.

Time Delays: The crucial aspect to control is the temporal overlap between laser pulses. This alignment can be achieved

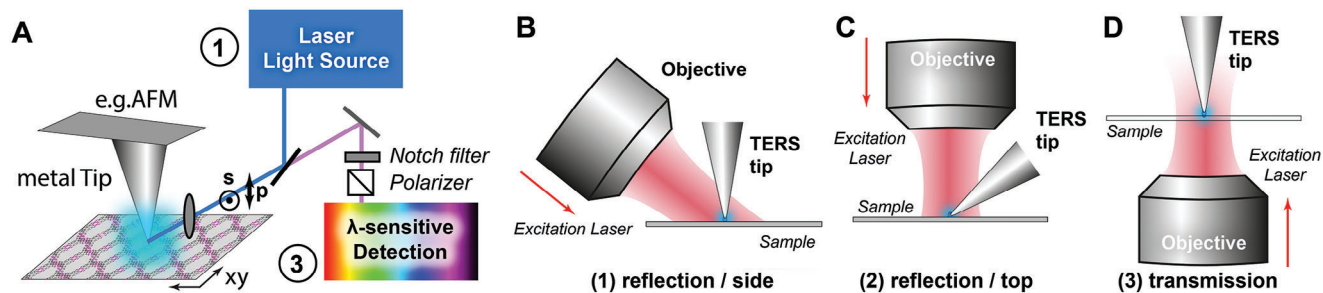


Figure 20. Configurations of nearfield microscopes for TERS. A) Schematic implementation of a TERS microscope based on AFM. B–D) Most frequently used configurations based on i) STM i), ii) SFM, and iii) AFM.^[129]

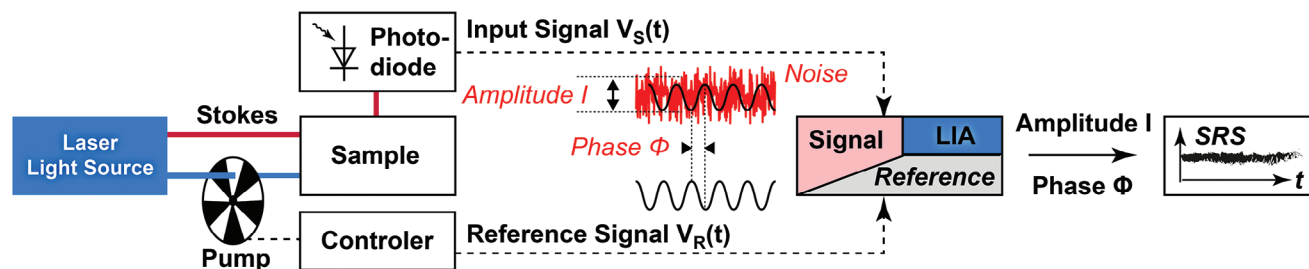


Figure 21. Working principle: Lock-In Amplifier. Two lasers are focused on a sample, while the pump beam (depicted in blue) is periodically blocked at a fixed frequency. The signal of the Stokes pulse is detected via a photodiode and analyzed by the LIA. It recognizes the periodic signal increase due to SRS on top of a constant signal by the Stokes pulse. The LIA extracts the small signal due to SRS, suppresses noise, and amplifies the extracted signal afterward.

using optical delay lines or mechanical translation stages. These components introduce controlled differences in the optical path length, resulting in precise temporal delays on the femto- to picosecond time scale between the laser excitation and the detection system. They allow for the measurement of Raman signals, e.g., at different time intervals after a trigger pulse, and ensure the temporal overlap between different laser pulses from separate beam paths used in nonlinear Raman approaches (Section 3.4.5).

Timing Electronics: Timing electronics play a crucial role in synchronizing a Raman setup, ensuring the precise coordination of various components, including delay stages, sample stages, automated optics, the synchronization of laser pulses, and timed readout via the detection system. The electronics is usually controlled via software, i.e., it is built-in or connected to a PC. The experiment is started by triggering the laser excitation, controlling the integration time of the detection, coordinating the data acquisition as a function of space (in situ/imaging) or as a function of time (transient/in operando), and is followed by a repositioning of either the XYZ sample stage (for space resolved Raman spectra) or the temporal delay (for time-resolved Raman spectra) before a new measurement cycle is carried out. Alternatively, a series of Raman spectra is taken for in operando measurements of for probing chemical reactions in situ.

Lock-In Amplifier: A Lock-In Amplifier (LIA) plays a crucial role in detecting a single-frequency SRS signal generated by fs- or ps-lasers operating at MHz repetition rates (as described above and in Sections 2.2.4 and 3.1.2). The challenge lies in measuring the weak SRS signal, which is accompanied by a much stronger signal from the Stokes laser at the same wavelength. How is this accomplished? The LIA utilizes low-pass filtering and amplification to isolate and enhance the SRS signal (Figure 21). This implies that the time-varying Stokes signal, after passing through the sample, is detected using a photodiode. The photodiode captures the overall intensity of the combined Stokes and SRS signal.

For SRS to occur, the pump pulse is focused onto the sample. Its signal does not reach the detector directly. In the excitation beam path of the pump laser, there is an electro-optic modulator (EOM) or acousto-optic modulator (AOM) which blocks or unblocks the laser excitation at a constant frequency on the order of 5–10 MHz. At this specific frequency, SRS leads to a stimulated Raman gain (SRG) in the Stokes pulse. Consequently, the photodiode detects a constant intensity from the Stokes laser, which is superimposed with a small, periodic signal increase at the frequency of the EOM/AOM due to SRG. This combined signal

serves as the input for the LIA. Additionally, the sinusoidal signal generated by the AOM/EOM controller is provided as a reference to the LIA. This reference signal aids the LIA in determining the precise frequency and phase of the original signal modulation compared to the signal recorded on the photodiode.

In the next step, the LIA performs two operations. Firstly, it mixes/multiplies the two input channels, i.e., the input signal from the photodiode with the reference frequency of the EOM/AOM. Secondly, it directs the multiplied signal to a low-pass filter, where the signal is integrated over time. One can think of this process as a Fourier transformation combined with a frequency filter. The low-pass filter allows only those signals (components coming from the photodiode) to pass through the filter, which have the same frequency and phase as the reference frequency. All other contributions are not amplified, leading to attenuation and effective suppression of noise and non-SRS signals. As a result, the LIA only filters out modulated photons due to SRS while attenuating the actual, constant signal contribution of the Stokes beam. In the final step, this filtered signal is further amplified.

3.3.3. Wavelength Sensitivity

All detector systems convert the intensity of photon fluxes into measurable electronic signals. They do not exhibit any spectral sensitivity. To distinguish between different vibrational modes of the Raman spectrum, we still need a technical device that provides wavelength sensitivity. Here, two methods are in place: 1) dispersive devices such as spectrometers using prisms or gratings to detect the spectrum in the time domain and 2) nondispersive approaches, based on interferometers to detect single transitions in the frequency domain via Fourier transformation.

Dispersive Approaches: Most systems for Raman spectroscopy rely on a dispersive approach, i.e., they use a spectrograph in combination with a detection system to separate and detect the scattered light according to its wavelength.

Here, a dispersive element like a prism or optical grating diffracts the light under different angles depending on the wavelength (Figure 22A,B). In a prism, diffraction happens because the refractive index of the material is wavelength-dependent. According to Snell's law, the diffraction of light will occur under multiple angles at the prism interfaces when light with different wavelengths enters and leaves the prism. For optical grat-

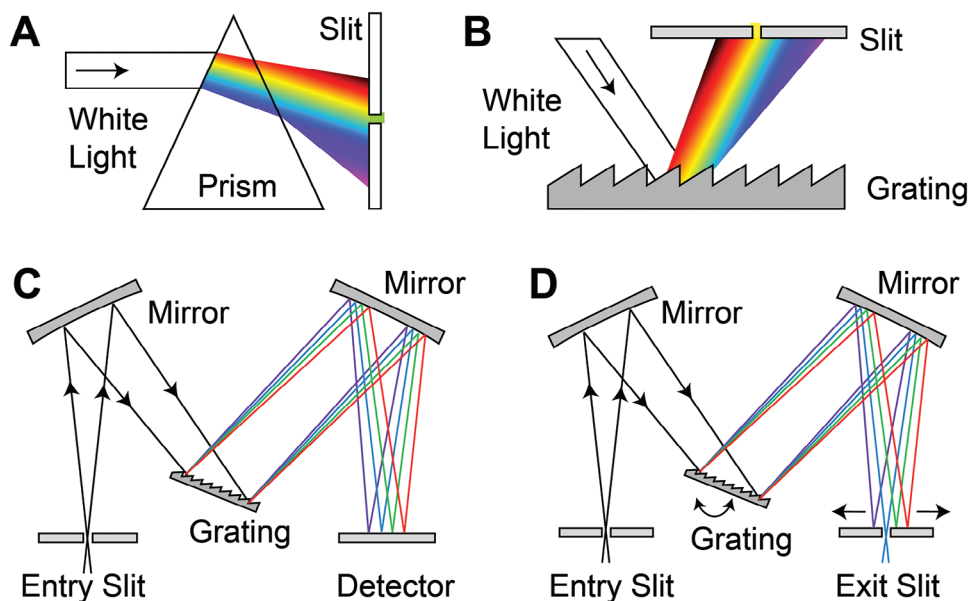


Figure 22. Diffraction of light as a source for wavelength sensitivity. A-B) Light with different spectral components can be spectrally decomposed either by using A) a prism or B) a grating. C) Czerny-Turner-Spectrometer. D) Monochromator.

ings commonly used in Raman spectroscopy, light is reflected at a plain surface covered by multiple grating lines, usually between 600 to 1800 lines per millimeter. Each of the reflecting lines can be considered as a point-like light source, that ‘emits’/reflects the incident light. Constructive interference between the reflected light fields occurs at different angles depending on the wavelength and distributes different spectral components spatially, which can be chosen geometrically.

To measure the spectrum of the light leaving a spectrometer, we place a detector array (e.g., a CCD camera) in the focal plane and measure the intensities at different angles that correspond to specific wavelength ranges. A widely used configuration is the Czerny-Turner design (Figure 22C).^[133] Here, the signal light is focused on an entrance slit, then a concave mirror collimates the light and reflects it on the grating. The grating spreads the light into its spectral components, and a second concave mirror focuses the light on the detector. Spectrometers are also frequently used as monochromators (Figure 22D) in combination with point detectors. Here, a slit is placed in the focal plane after the spectrometer, so most of the light is blocked, besides a small wavelength range. This nearly monochromatic light can be detected afterward as a function of space in CRS microscopy, for example.

Nondispersive Approaches Using Interferometers: The second possibility for resolving polychromatic light into a spectrum is an interferometric spectrometer, which is available but rarely used for linear Raman spectroscopy. The most common interferometer type is a Michelson interferometer. Here, the collected light is separated into two beams, and the path length of one of them is changed over time before both detection paths are re-combined. The resulting intensity after the interference of both beams is then measured for varying differences in path lengths. A Fourier Transformation of the resulting interference pattern provides the spectrum. While Fourier-Transform (FT) Spectroscopy works best for NIR and MIR radiation, the intensity of the Raman

signal drops with $1/\lambda^4$. Hence, linear Raman is mostly carried out in the visible range with dispersive spectrometers. FT Interferometric Raman microscopes rely on Nd:YAG lasers (1064 nm) for excitation.^[134] Fourier-transform-based approaches were further reported for specialized CARS setup with a spectral resolution of less than 5 cm^{-1} .^[135]

3.3.4. Polarization Sensitivity

Polarization control in Raman setups provides access and information on the symmetry of vibrational bonds and consecutively of crystal orientations. The more symmetric a specific vibrational mode is, the more it will couple to the incident polarized light, and be suppressed if the polarization of the incident and observed detected light are perpendicular to each other. The symmetry of the vibrational mode is characterized by the depolarization ratio ρ

$$\rho = \frac{I_{\text{Raman},\parallel}}{I_{\text{Raman},\perp}} \quad (39)$$

where $I_{\text{Raman},\parallel}$ and $I_{\text{Raman},\perp}$ denote the measured intensity of a Raman transition for parallel and perpendicular polarization of the incident and Raman scattered light (Figure 23), respectively. A mode is considered polarized for values between 0 and 0.75. Technically, measuring the depolarization ratio is helpful to quantify the precision and sensitivity of linear polarization that a setup can measure.

To exploit the polarization dependence of Raman scattering, we need optical elements, that control the polarization of the exciting laser source(s) and scattered light. For crystalline materials, such as MOFs the measured intensity of a Raman transition will depend on the crystal orientation, i.e., how well a specific vibration can couple. As a consequence, if we measure MOF powders,

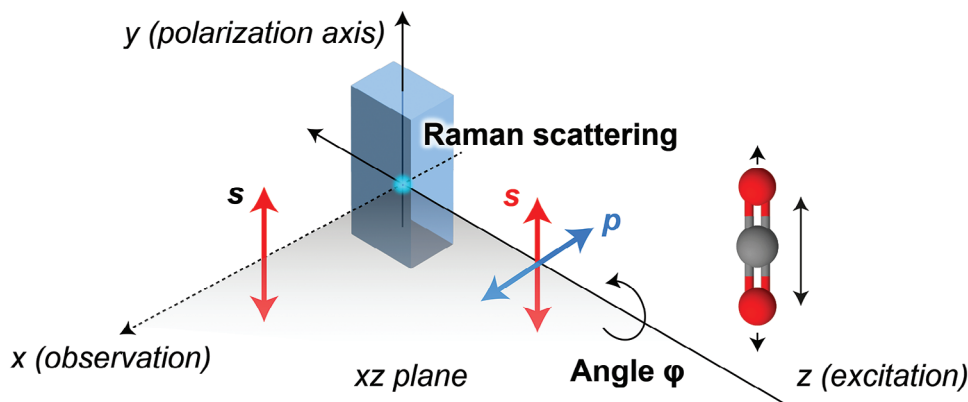


Figure 23. Polarization-dependent Raman scattering for linear polarized excitation and detection. Raman scattering depends on the orientation of the sample with respect to the direction of the incident laser light and the detector position as well as the polarization of the incident and Raman-scattered light. P polarization refers to a polarization parallel to the plane ($\varphi = 0^\circ$) built by the excitation and detection axis, here the XZ plane. S polarization refers to a perpendicular polarization ($\varphi = 90^\circ$; S from the German word 'senkrecht') with respect to the surface.

where multiple crystals with different orientations will contribute to the total signal, the variations in intensities for different vibrational modes due to different orientations will average out. Hence, for polarization-dependent measurements, it is important to have a uniform sample or a single monocrystalline MOF particle in a fixed orientation. Only in this case, changes in the depolarization ratio can report defects, local changes in the orientation of the framework, or chirality.

Linear Polarization: The majority of lasers emit linearly polarized light. Let's consider their emission along the Z-axis as illustrated in Figure 23. In this case, the orientation of the polarization can be controlled by a $\lambda/2$ waveplate after the laser. This component enables the gradual rotation of the polarization axis by the angle φ . If the laser output is unpolarized, an additional polarizer is required, which defines the parallel (p) or perpendicular (s) polarization. The orientation of polarization is defined with respect to the plane spanned by the excitation and detection direction, which is the XZ plane in this example. Raman scattered light is collected afterward for a chosen geometry (along the X-axis; Figure 23). A polarizer (analyzer) before the detector makes sure that only light along the desired polarization is detected. By simply rotating the exciting laser light and the polarizer in front of the detector, one can probe for rotational selection rules and crystal orientation in angle-dependent spontaneous Raman spectra. Polarization-sensitive measurements can be equally implemented in other Raman setups, including TERS, CARS, and SRS instruments by controlling the polarization in the excitation and detection path.^[136] With this simple approach, Ciupa et al. could determine the symmetry of Raman modes in ethyl ammonium metal-formates with cadmium ions (EtACd) via spontaneous Raman scattering.^[137]

Circular Polarization: If the measured Raman intensity by chiral molecules depends on whether the incident or scattered light is left- or right-handed circularly polarized, it is called Raman optical activity (ROA). To measure ROA, we need to control the polarization in the excitation or detection path. Starting from a parallel polarized laser (Figure 23), we need a $\lambda/4$ waveplate in the excitation path to produce circular polarized light. For the detection, a $\lambda/4$ plate and an analyzer are further required. The

polarization can be turned from left- to righthanded by adding a $\lambda/2$ waveplate in the respective beam path. The degree of circularity DOC, analog to the depolarization ratio ρ defined in Equation 39, measures the same tensor invariants of the polarizability (see Section 2.1) but for polarized laser excitation. It is given as the ratio between the intensity difference and the sum of Raman scattered intensities I_R and I_L measured for right-handed and left-handed laser excitation, respectively.

$$DOC = \frac{I_R - I_L}{I_R + I_L} = \frac{ROA}{I_R + I_L} \quad (40)$$

Here, ROA is derived as the difference between the right- and left-handed intensity. It can be measured in two experimental schemes: in the first one, the incident light is circularly polarized, and the scattered light of any polarization is detected. In the second one, the incident light is depolarized or linearly polarized, and right- and left-handed components of the scattered Raman light are detected. Together with different measurement geometries, different terms of the polarizability tensor will contribute to the detected signal. A detailed review of ROA can be found elsewhere.^[138] ROA can be implemented in spontaneous as well as coherent Raman setups.^[139] It was recently proposed as a strategy for achieving enhanced Raman scattering by chiral SERS substrates to probe Raman-inactive molecules.^[140]

3.4. Measuring Reactions In Time and Space

So far, we have discussed all-optical devices and instrumentations necessary to implement the different Raman methods. Raman spectroscopy, however, is even more versatile and can be carried out in different measurement modes on the various setups to investigate MOFs and their properties with high temporal resolution (transient spectroscopy), as a function of space (in situ), during actual operation and/or under working conditions (in operando). The temporal resolution depends on the employed instrumentation used for steady-state and transient Raman spectroscopy or Raman microscopy, as described below. We

will first describe the three measurement modes and summarize the most frequent setups for state-of-the-art Raman spectroscopy and imaging afterward.

3.4.1. *In Situ Raman spectroscopy*

In situ Raman spectroscopy refers to Raman-based techniques performing spectroscopic measurements directly on a sample in its natural or undisturbed state, without any sample preparation or extraction. It usually employs confocal Raman microscopes to probe the sample with sub-micrometer resolution. In situ Raman spectroscopy is used for various applications to probe the response of MOFs upon exposure to an external trigger, such as light or an electromagnetic field,^[141] to monitor the MOF framework during host-guest interactions, but also for catalytical reactions. It plays an important role, in particular, in catalysis, where both the nature of the catalytic surfaces and the surface reaction steps involved in the catalytic process depend on, or may be modified by, the presence of the reaction mixture, i.e., the chemical environment around the MOF. Hence, it is imperative to study catalytic reactions in situ, under environments mimicking those encountered during catalysis, or, better yet, using an in operando approach, following the time evolution of the catalytic system as the reactions take place.

3.4.2. *In Operando Raman spectroscopy*

In operando spectroscopy refers to measurements that are carried out in real-time, allowing researchers to observe and monitor changes that occur in a sample under specific working conditions. It is carried out in combination with in situ approaches and used for studying dynamic processes, such as chemical reactions, surface reactions, phase transitions, or structural reactions, where the sample may change over time. This holds, in particular, true for catalytical applications of MOFs, in which the surface of the MOF crystals defines the nature of the species involved in the process. Operando methodologies that provide structural and chemical sensitivity, such as Raman/IR, UV-Vis, NMR, Mössbauer, or X-ray absorption spectroscopy XAS, follow the time evolution of the catalytic system as the reactions take place.^[142] In operando Raman spectroscopy records consecutively spectra of the sample system. It can probe changes in the host framework as well as interacting guest molecules, reactants, and intermediates. Temporal shifts of Raman bands report on 1) changes in concentration (amplitude), 2) tension in the material or presence of guest molecules (vibrational shifts), 3) newly formed intermediate species, bond formation, or adsorption of guest molecules (appearance of new Raman resonances/disappearance of former transitions), 4) the degree of crystallinity (spectral width of MOF associated phonons) and 5) the crystal orientation and symmetry (e.g., by the depolarization ratio).

3.4.3. *Transient Raman Spectroscopy*

Transient Raman spectroscopy studies short-lived, transient chemical intermediates that occur in a sample after an external stimulus is applied, such as a pulse of light or an electrical current. It provides information about the dynamic processes

(and relaxation timescales within a material. Transient Raman spectroscopy captures the property changes over extremely short timescales ranging usually from femtoseconds to microseconds by using time-resolved spectroscopy or pump-probe spectroscopy schemes (see Section 3.4.5).^[143] It provides insights into processes, such as energy transfer reactions, charge carrier dynamics, molecular vibrations, bond formations, and chemical reactions. Transient Raman spectroscopy is often used to study the excited state dynamics in photochemical reactions or the relaxation processes in semiconductors after a sudden change in applied voltage.

3.4.4. *State-of-the-art Setups for Linear Raman techniques*

State-of-the-art Raman setups for spontaneous Raman, RRS, and SERS, which do not require any spatial resolution (Macro-Raman setups), are based on spectrophotometers in combination with several fixed CW lasers to select a wavelength that matches the resonance conditions or causes less autofluorescence in the sample. The spectrograph contains the sample holder and optics to focus the laser onto the sample and to collect the Raman-scattered light for detecting it on a diode array in a wavelength-depending manner. In all cases, Rayleigh scattering is blocked in the detection path by several Notch filters.

Time-gated Raman spectroscopy (Figure 24) in combination with a spectrophotometer allows for circumventing a common problem in spontaneous Raman spectroscopy:^[144] the autofluorescence of samples, such as UiO-66-NH₂ or MOFs with photoactive compounds. Time-resolved techniques are an elegant way to avoid fluorescence contributions. In time-gated Raman Spectroscopy, a pulsed laser (150 ps; 40 MHz) is employed for exciting the sample. It is coupled to a standard spectrometer, where the scattered light is detected via a spectrograph and a SPAD CMOS array detector that provides sub-nanosecond time resolution and nearly single-photon sensitivity. This way, single photons can be detected according to their arrival times with respect to the laser pulse. Since Raman scattering occurs on the sub-nanosecond time scale, while luminescence usually has a longer lifetime, both contributions can be separated by selecting a time window with primarily Raman scattering. By use of an electronic delay generator, the position of the time gate can be chosen such that only Raman scattered photons can be detected before fluorescence occurs. In a recent work,^[144] spectra were recorded up to 5 ns after the laser.

Micro-Raman Spectroscopy, also called Raman microspectroscopy or Confocal Raman spectroscopy, offers sub-micron resolution and distinguishes itself primarily by incorporating a light microscope instead of a spectrophotometer. Usually, it relies on a confocal microscope, which allows for carrying out Raman mapping experiments, so-called Hyper-spectral imaging. It enables in situ and in operando measurements as a function of different working parameters, such as external triggers like voltage, heat, or humidity.

Nano-Raman Spectroscopy, based on TERS, is meanwhile commercially available. The most common implementation is based on an AFM-type setup with CW laser excitation and spectrometer-based detection. Due to the plasmonic nature of the metal tip, TERS is commonly configured with polarization-

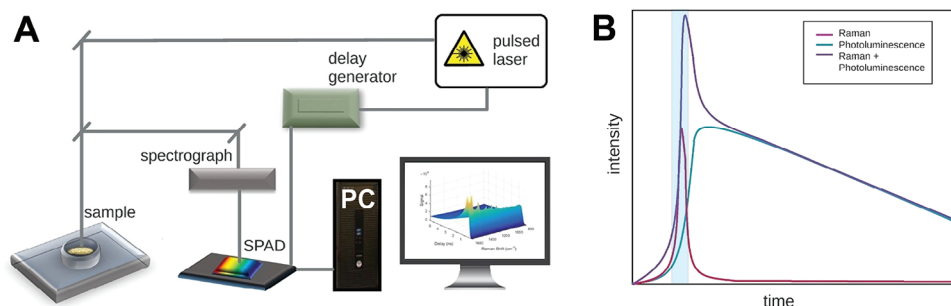


Figure 24. Time Gated Raman spectroscopy. A) Schematics of a time-gated Raman setup. The light of a pulsed laser focuses on the sample. Raman scattered light is detected via a spectrometer and a highly sensitive SPAD CMOS array detector and recorded on the computer. The timing between excitation and detector can be varied using a delay generator. B) Since Raman scattering occurs on the sub-nanosecond time scale, the time-dependent Raman signal can be separated from the disturbing background of photo luminescence occurring on the later nanosecond time scales upward. Panel A-B was reproduced under the terms of the Creative Commons CC-BY 4.0 License.^[144] Copyright 2018, The Authors. Published by the American Chemical Society.

sensitive excitation and detection. Examining Raman spectra under different polarizations allows us to investigate whether the shape of the AFM tip affects the recording of Raman spectra by mode-specific coupling, which can be monitored by changes in the depolarization ratio. For imaging, the sample is moved via a piezo stage for scanning the illuminated AFM tip over the sample surface.^[107,129]

3.4.5. State-of-the-art Setups for Coherent Raman Techniques

Single Frequency and Hyperspectral CRS Spectroscopy: Coherent Raman spectroscopy relies on the interaction of at least two light fields with the sample. As described in Section 3.1.2., state-of-the-art single-frequency CRS approaches employ two spectrally narrow ps laser pulses (**Figure 25A**) in the NIR. Here, the

pump beam is usually chosen at a fixed wavelength of around 800 nm, while the Stokes beam is tunable starting at the pump to a longer wavelength. To synchronize both laser pulses, they are usually derived from a single laser source, split after the laser to be individually modified as required, and recombined both in time and space at the sample using a dichroic mirror and a delay stage. Raman scattering in the sample at a confocal microscope occurs whenever the difference in frequency between both lasers $\omega_p - \omega_s$ matches a vibrational transition of the sample Ω . For CRS microscopy, the sample is scanned at a given vibrational transition afterward. The full spectrum of the sample is recorded per point by tuning the Stokes laser over the full range. For detecting the scattered light, SRS and CARS employ two different approaches. For CARS, a Notch and short-pass filter is employed to separate the signal from the Stokes and pump pulses before detecting it via an APD. In the case of SRS, an acousto-optical

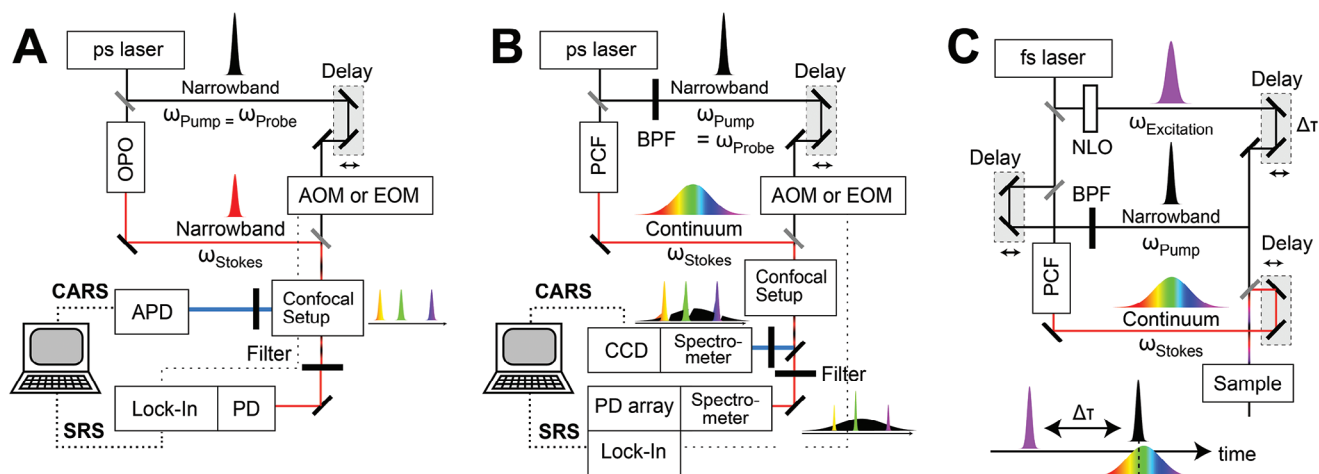


Figure 25. Schematics of Coherent Raman Scattering setups. A) Single Frequency or Hyperspectral CRS setups are based on ps or fs lasers, an optical parametric oscillator (OPO) for tuning the Stokes wavelength, and an acousto optical modulator (AOM) or electro-optical modulator (EOM) for switching the pump pulse. The CARS or SRS signal is detected using an APD or PD (photodiode), respectively. B) For broadband CRS, the spectrally broad Stokes pulse is derived, e.g., by nonlinear optics inside a photonic crystal fiber (PCF). The CARS or SRS signals are recorded via multi-channel detection, either by a CCD or multi-channel Lock-In detection system. C) Time-resolved CRS spectroscopy relies on the interaction with a third excitation pulse responsible for triggering the reaction. CRS is used to probe the spectral signal as a function of the delay time $\Delta\tau$ after the excitation pulse. The excitation is usually derived by nonlinear optics (NLO), e.g., by frequency doubling or tripling to generate light in the UV-Visible range.

device modulates the pump beam in the MHz regime and serves as a reference frequency for the Lock-In amplifier in the detection path. Stimulated Raman Gain (SRG) of the Stokes beam is usually measured via a photodiode (PD) and Lock-In after blocking the pump pulse with a Notch filter. Both CRS signals are recorded afterward as a function of space or time on a computer. Single frequency CARS or SRS allows for fast chemical sensitive imaging with pixel dwell times in the low microsecond regime.^[112c]

For *Hyperspectral CRS*, which monitors the full spectrum per pixel of the sample, the narrowband Stokes is successively tuned over a certain wavelength range. Enhanced Raman scattering is observed for those frequencies of the Stokes pulse, for which the resonance condition $\omega_p - \omega_s = \Omega_i$ is fulfilled. If the CRS signal at the APD (for CARS) or the PD/LIA (for SRS) is measured as a function of the frequency difference between the pump and Stokes pulse, a full Raman spectrum can be acquired. The scanning times for Hyperspectral CRS depend on the desired spectral range and resolution. Garbacik et al. measured 4 frames of a 512×512 -pixel spectral image with 2 cm^{-1} resolution over a spectral range of 140 cm^{-1} in roughly 300 s using hyperspectral CARS.^[145] Ozeki et al. obtained spectral images with 500×480 pixels over a spectral range of 300 cm^{-1} and a resolution of 3 cm^{-1} at a frame rate of 30 images/s by using Hyperspectral SRS.^[146]

Multiplex CRS Spectroscopy: Multiplex CRS is another approach besides Hyperspectral CRS to obtain full spectra per pixel. A more detailed discussion about the instrumentation for multiplex CARS or SRS can be found in.^[68d] Briefly, state-of-the-art multiplex CRS setups rely on fs lasers to generate the spectrally broad femtosecond Stokes beam (Figure 25B), e.g., by white light generation in a photonic crystal fiber (PCF; MHz laser) or nonlinear crystals like a sapphire in the case of lasers with kHz repetition rate. The pump pulse is still spectrally narrow and defines the spectral resolution. When both light fields interact with the sample with spatiotemporal overlap, CRS will occur for all frequencies of the Stokes pulse with temporal overlap, which fulfills a Raman condition $\omega_{\text{pump}} - \omega_{\text{stokes}} = \Omega_i$, for any of the vibrational modes Ω_i in the sample. CARS leads to strongly enhanced, blue-shifted signatures $\omega_{\text{CARS}} = 2\omega_{\text{pump}} - \omega_{\text{Stokes}} = \omega_{\text{pump}} - \Omega_i$ with dispersive line shapes on a broad, blue-shifted background due to unspecific four-wave mixing at $\omega_{\text{FWM}} = 2\omega_{\text{pump}} - \omega_{\text{Stokes}}$ (Figure 25B). FWM simply mirrors the Stokes continuum compared to the Raman pump pulse into the blue-shifted spectral range. SRS, on the other hand, increases the intensity at frequencies of the Stokes spectrum, fulfilling the Raman condition, and leads to sharp peaks on top of the original Stokes continuum. CRS spectra are both detected via a spectrograph and a line detector. Multiplex CARS is recorded via a (em)CCD camera, while multiplex SRS can be read out via a multichannel Lock-in amplifier (LIA) or a dedicated broadband detector. Typical pixel dwell times for Multiplex CARS are on the order of several 10–100 milliseconds. Czerwinski et al. measured full SRS spectra with a broadband detector from 900 cm^{-1} to 3200 cm^{-1} within 100 μs .^[147] There are two strategies to avoid expensive multichannel detectors for recording SRS spectra: first, they use a monochromator in combination with a point detection scheme and tune the spectrum in the monochromator. Second, the Stokes continuum is temporally stretched to several tens of picoseconds, e.g., by traveling through highly diffractive materi-

als, such as SF6 glass. In this case, the narrow pump pulse will only temporally overlap with spectral snippets of $\approx 15 \text{ cm}^{-1}$ of the Stokes field, which can be detected using a single-frequency detection scheme. The full spectrum can be recorded by changing the time delay between the pump and Stokes pulse.

Time-Resolved CRS Spectroscopy: Transient CRS spectroscopy relies on the interaction of at least three light fields (Figure 25C). In addition to the pump and Stokes field, responsible for probing the Raman transition, an excitation pulse in the UV–Visible range is employed to address the electronic structure of the sample. To select the precise wavelength of the third pulse, different nonlinear strategies are in place, ranging from sum frequency and third harmonic generation over to noncollinear optical parametric amplifiers (NOPA) to generate tunable wavelengths to induce a photochemical reaction. Transient coherent Raman spectra are recorded as a function of the delay $\Delta\tau$ between the excitation laser and the pump and Stokes lasers. Transient spectra are usually recorded using fs lasers with a kHz repetition rate and selected steps of several femtoseconds up to tens of picoseconds. For nanoseconds upward, delay-generators are used.

4. Probing MOFs by Raman Techniques

Raman techniques provide a highly versatile set of tools for investigating metal–organic frameworks (Figure 26A). They can be chosen according to 1) the required sensitivity of Raman scattering, i.e., between spontaneous and enhanced Raman techniques, 2) the measurement mode, and 3) the preferred resolution in time and space. Raman techniques allow for characterizing MOFs in 2D and 3D geometry with static/structural or dynamic fashion but also for monitoring dynamic processes, identifying and quantifying different molecular entities according to their vibrational fingerprint. The following sections provide an overview of the abilities of Raman techniques for investigating metal–organic frameworks, their benefits, and pitfalls as well as a short guide on how to choose the design of the Raman experiment.

4.1. In Situ Measurements In Static MOF Systems

Raman scattering gives insights into the symmetry of MOF structures, and the nature and strength of chemical bonds. It is sensitive to surface functionalization by probing functional groups, and their interplay with the framework or guest molecules and allows an assessment of phase purity (Figure 26B). In a typical MOF spectrum, the vibrations of the organic linker are predominantly observed within the range of ≈ 500 – 1800 cm^{-1} , while the modes associated with metal–ligand interaction or lattice vibrations appear at lower frequencies below 200 cm^{-1} . This property of Raman scattering proves superior to infrared (IR) absorption, as IR spectroscopy cannot access the low-frequency region. A notable example highlighting this advantage is the study conducted by Kumari et al., where Raman spectroscopy allowed monitoring of the MOF-508 structure during CO_2 uptake under different stimuli. The authors identified a cooperative adsorption mechanism of CO_2 at 149 cm^{-1} to the framework.^[148] Furthermore, Raman spectroscopy proves useful in exploring low-frequency lattice vibrations involved during phase transformations in flexible

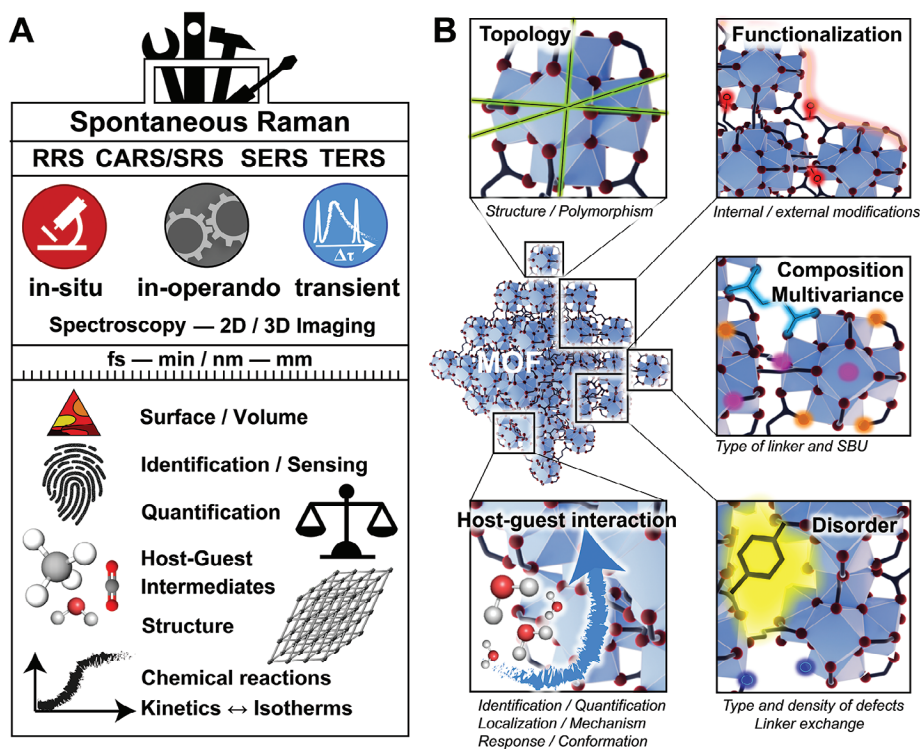


Figure 26. Raman scattering meets metal–organic frameworks. A) The Raman toolbox offers different methods for probing materials in situ, in operando, and with time resolution. It gives access to different lengths and time scales. Raman scattering is sensitive to surfaces and 3D samples and allows the identification and sensing of molecules quantitatively based on their vibrational fingerprint. It provides structural information in crystalline material and sensitivity for probing mixed samples and reactions. B) Raman-based techniques can elucidate the topology and potential polymorphism of MOFs. They can identify and localize an internal or external functionalization since they provide chemical sensitivity to the composition of the MOF system, in particular, with respect to defects and multivariance. Raman techniques can investigate MOFs beyond their composition during interaction with guest molecules and help to decipher the molecular working mechanism of sorption and response of metal–organic frameworks.

MOFs (Figure 26B). Krylov et al. employed THz Raman spectroscopy to distinguish between two forms of DUT-8(Ni), its rigid and flexible conformation, at 23 and 60 cm^{-1} .^[149] The Kitagawa lab employed Raman scattering to identify structural transformations of the zinc clusters in a switchable MOF, which explained the multi-step behavior of CO_2 uptake.^[150] Raman scattering is not only able to probe CO_2 in a switchable MOF system but also a temperature-dependent uptake in MOFs, as demonstrated in ZIF-8 between 75 and 325 K.^[151] Besides the remarkable chemical sensitivity, Raman techniques with variable observation volumes are available, reaching down to a few hundred nanometers. This capability allows for investigating local alterations in the framework, providing insights into the interaction with guest molecules or defect sites.^[152] Experimentally, Raman spectroscopy can be conducted across a wide spectral range between the UV to NIR/IR, providing flexibility in wavelength selection based on the sample system. This way, fragile MOFs can be examined at wavelengths longer than 785 nm at moderate to high laser powers with decreased risk of photodamage.

4.2. Host-Guest Interactions

One of the notable features of Raman spectroscopy is its non-destructive and non-invasive nature, making it an ideal technique

for the direct observation of adsorption processes. With its chemical sensitivity, Raman spectroscopy can monitor the uptake of various species like CO_2 ,^[61a,b,151] N_2 ,^[151] O_2 ,^[153] or CH_4 ,^[154] and many more.^[29c,e] For instance, Andrade et al. used vibrational spectroscopy to investigate the iodine uptake in Zr-UiO-66 and different ratios of Hf substituted UiO-66 (25, 51, 75, and 100% Hf).^[155] The crystals were first characterized by PXRD, SEM, and sorption measurements, yielding a smaller lattice, bigger crystal, and smaller Brunauer-Emmett-Teller (BET) area with increasing amounts of Hf. Additionally, the substitution induced significant shifts and relative intensity changes for Raman and IR bands attributed to a higher acidity of hafnium and stiffening of the framework. This study demonstrated that UiO-66(Hf) exhibited a preference for capturing iodine, which was confirmed by the emergence of new Raman transitions in the range of 100–210 cm^{-1} (Figure 27A). Through the application of Raman spectroscopy and chemometrics, the species responsible for the observed bands were identified as I_3^- , perturbed I_2 , and free I_2 . Additionally, FTIR measurements yielded alterations in the oxo and hydroxyl groups of the cluster upon iodine adsorption into UiO-66(Hf).

Although the adsorption process of mixed gases is important, the determination of mixed gas isotherms remains challenging. Nath et al. used Raman spectroscopy to determine binary gas adsorption isotherms at the single crystal level.^[156] The

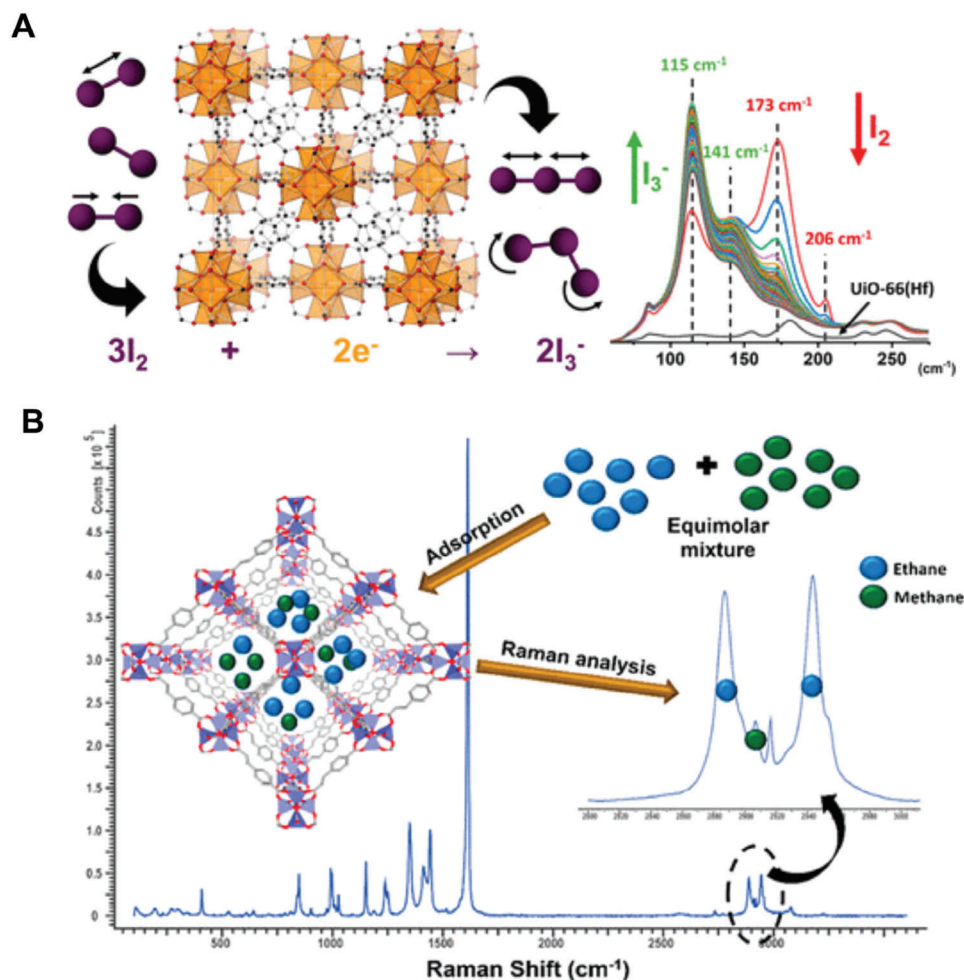


Figure 27. Investigation of adsorption processes. A) Iodine uptake in UiO-66. Reprinted with permission.^[155] Copyright 2022, American Chemical Society. B) Mixture adsorption of methane and ethane gas. Reproduced with permission from.^[156] Copyright 2022, American Chemical Society.

different adsorbents can be chemically distinguished by their specific Raman transitions, and allow for observing multiple host-guest interactions simultaneously. Methane features a strong band at 2916.8 cm⁻¹, and ethane has a doublet of maxima at 2897.7 and 2953.4 cm⁻¹. The bands shift to lower wavenumbers upon adsorption and display a broadening that is tentatively assigned to a combination of confinement effects, multiple adsorption sites, and mode coupling. The linear dependence of the Raman signal on the number of molecules allows to quantitatively monitor the gas uptake via the integrated intensity of adsorbent-associated peaks compared to Raman resonances of the MOF. No visible changes upon gas exposure indicate a rigid framework. Since the above-mentioned bands of CH₄ and C₂H₆ do not spectrally coincide, both gases can be monitored simultaneously, revealing a competitive binding to the framework (Figure 27B). Confocal Raman microspectroscopy generates sorption isotherms on the sub-milligram scale. It characterizes the sorption of mixtures of gases with high sensitivity and chemical information and can disentangle the individual sorption contributions of both gas species, giving an advantage over gravimetric and volumetric methods.

4.3. Responsive MOF Systems

Raman spectroscopy is an excellent tool for investigating the response of frameworks to external stimuli, particularly in the case of photoswitchable MOFs. These MOFs are well-suited for Raman-based investigations as the light stimulus is often implemented in the Raman instrument, e.g., when multiple lasers are integrated into one single microscope setup. Such an approach was, for example, used to investigate MOFs based on an azobenzene photoswitch. The incorporation leads to a light-induced structural contraction along with gas sorption. The release of the adsorbent is done via negative gas adsorption by light-gated breathing. Krause et al. conducted Raman measurements on DUT-163 under a dry nitrogen atmosphere during exposure to light at 365 nm.^[141] The purpose of the irradiation was to promote the E/Z-isomerization, but no significant changes were observed in the Raman and DRIFT spectra. This absence of E/Z-isomerization was further confirmed by nitrogen adsorption measurements. However, a bathochromic shift was observed in the DRUV-VIS spectrum after 365 nm irradiation, indicating a dynamic response of the framework to the gas adsorption

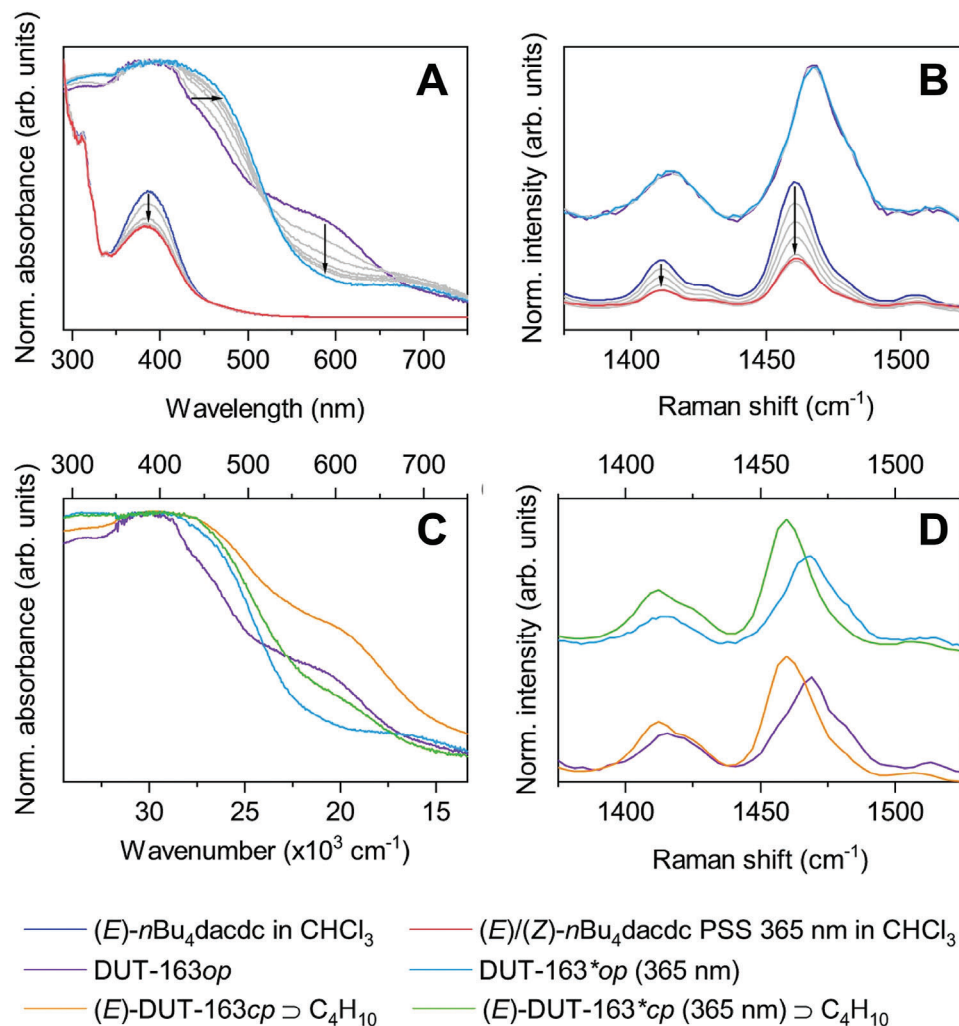


Figure 28. Spectroscopic investigation of DUT-163 and its linker reacting to light in situ. A) UV-Vis absorption spectra upon 365 nm irradiation of the *n*-butyl derivative of the linker molecule $n\text{Bu}_4\text{dacdc}$ in CHCl_3 (blue to red) and DRUV-Vis absorption spectra of DUT-163 (purple to light blue), B) Corresponding Raman spectra of compounds in (A) upon 365 nm irradiation, C) DRUV-Vis absorption spectra of DUT-163 (purple) upon loading with *n*-butane (orange), 365 nm irradiation (light blue) and irradiation at 365 nm in the presence of 2-methylpropane (green), D) and associated Raman spectra upon loading with 2-methylpropane and irradiation at 365 nm. Adopted and reproduced under the terms of the Creative Common Attribution 4.0 Int. (CC-BY 4.0) License.^[141] Copyright 2022, The Authors. Published by Springer Nature.

(Figure 28). The contraction occurring within the MOF is based on the buckling of azobenzene.

4.4. In Operando Measurements

Raman spectroscopy offers high sensitivity via enhanced processes, which enables the detection of small concentrations of molecules in single crystals. It eliminates the need for labeling, and the samples require minimal preparation, allowing measurements to be taken in any physical state. Raman spectroscopy can monitor even reactions inside MOFs. For instance, alkene-based light-driven molecular motors can be incorporated in zinc pillared-paddle wheel BrYO-MOFs (moto-MOF).^[157] These motors exhibit large-amplitude, repetitive unidirectional rotations (Figure 29A). The photochemical and thermal isomerization of these motors was investigated both in solution and solid state. In

solution, UV-VIS measurements revealed a bathochromic shift after irradiation with 395 nm, confirming the formation of the metastable isomer. Raman spectra recorded in CH_3Cl displayed a sharp band at 1562 cm^{-1} attributed to the olefin stretch vibration. Following irradiation at 395 nm, a new band appeared at 1550 cm^{-1} , arising from the stretch vibration of the central double bond of the metastable isomer. Raman measurements allowed for monitoring the decrease of this band due to thermal helix inversion over time (Figure 29B). The activation barrier could be calculated from the rate constant, yielding a value in good agreement with the UV-VIS calculations. The desymmetrized analog of the motor system was also followed quantitatively by Raman scattering, identifying the E/Z-isomer at 1290 cm^{-1} .

Measurements performed at the solid-state samples detected changes in the framework in situ. Irradiation with light at 395 nm led to a decrease of the signal at 1562 cm^{-1} , coupled with a simultaneous increase at 1550 cm^{-1} . This behavior mirrored the

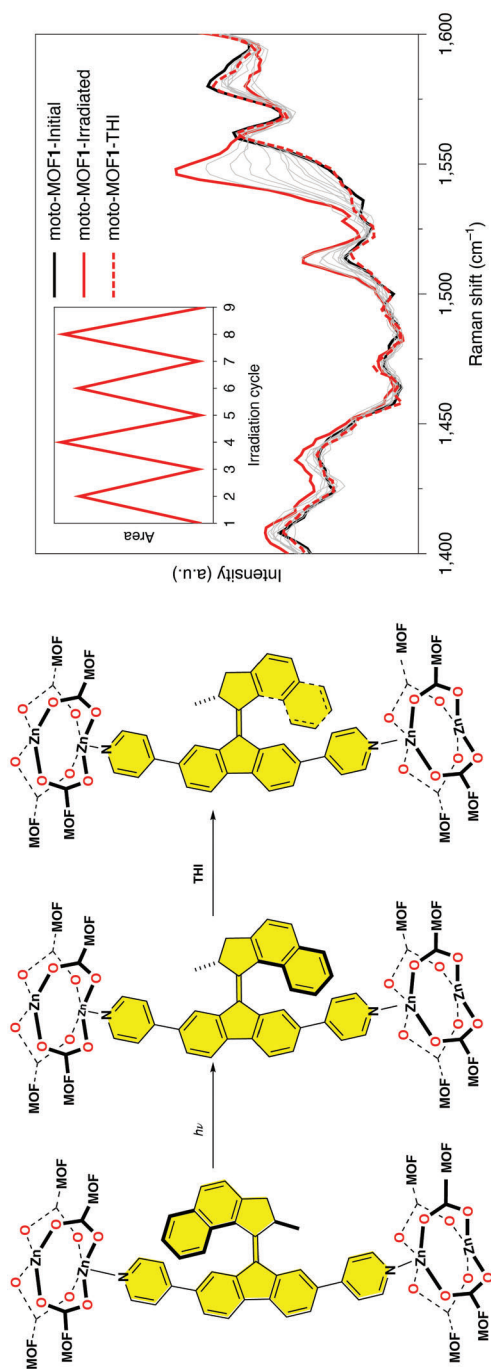


Figure 29. Raman investigation of molecular motors inserted in a zinc pillared paddle wheel MOF. Left) Schematic representation of structural changes during the photochemical and subsequent thermal isomerization (half of the rotary cycle) of 1 incorporated in moto-MOF1. Right) Changes in the Raman spectrum of moto-MOF1 (black solid line, initial) following irradiation at 395 nm (red solid line) and upon subsequent thermal isomerization (red dashed line) at 20 °C. Inset, Multiple irradiation/thermal helix inversion cycles. All Raman spectra were recorded at 785 nm with a power density sufficient to avoid sample heating. [157] Copyright 2019, Springer Nature Limited.

observations made in the solution, confirming the occurrence of the same isomerization process. At -5 °C, a high ratio of the metastable to stable isomer, similar to that observed in solution, was obtained, indicating that the motors undergo photoisomerization inside the MOF. Upon discontinuing the irradiation, the metastable isomer disappeared due to thermal relaxation. Furthermore, the entire process was found to be repeatable. The desymmetrized sample exhibited similar behavior. In this example, Raman spectroscopy provided valuable insights into photochemically and thermally driven rotary motion in solution and solid state. The measurements confirmed an unhindered 360° rotation for molecular motors incorporated into MOF systems.

In another, notable study, Jeong et al. leveraged the spatial resolution offered by confocal Raman microscopy to investigate the distribution of two linker molecules, azobis(4-pyridine) (AP) and trans-1,2-bis(4-pyridyl)ethane (BE), within a three-dimensional MOF denoted as $[\text{Ni}(\text{HBTC})(\text{XX})]$ (where HBTC = benzene-1,3,5-tricarboxylate and XX represents either AP or BE). The researchers showed that the linker distribution can be modulated by exchanging the pillars (AP and BE) depending on the temperature.^[23b] To accomplish this, $\text{Ni}(\text{HBTC})(\text{AP})$ was immersed in a solution of BE-Dimethyl-formamide (BE-DMF) at two temperatures: 5 °C and at 100 °C. In both cases, the AP pillars in the MOF were gradually replaced by BE pillars over time. However, the exchange process occurred more rapidly at high temperatures. Raman maps clearly illustrated the spatial evolution of the exchange process. At 100 °C, the AP pillars close to the surface were first replaced by BE, resulting in the formation of core-shell structures (Figure 30A,C). Conversely, at 5 °C, the exchange process uniformly replaced AP with BE throughout the crystal, leading to the formation of uniformly distributed crystals (Figure 30B,D). To differentiate both types of pillars, Raman peaks at $1150 - 1180 \text{ cm}^{-1}$ and $1630 - 1650 \text{ cm}^{-1}$ were employed. Jeong et al. attributed the observed behavior to different diffusion and exchange rates at different temperatures. At high temperatures, the exchange rate surpassed the diffusion rate, causing BE pillars to replace AP pillars before reaching the center of the crystal. Conversely, at low temperatures, the diffusion rate exceeded the exchange rate, resulting in the uniform distribution of BE pillars inside the crystal before the exchange took place. This study highlights the power of Raman microscopy to elucidate spatially resolved molecule transformations within MOFs.

4.5. Sensing Applications

Using MOFs in combination with SERS offers two significant advantages: 1) MOFs exhibit selective adsorption properties, leading to an increased concentration of the desired target molecules within the framework. 2) The combination of MOF with SERS results in a strong signal enhancement due to the chemical and electromagnetic mechanism. This combination enables highly sensitive, selective, and rapid sensing of molecules, even down to picomolar (pM) concentrations.^[158] This improvement in sensitivity is particularly valuable for detecting and analyzing multiple chemicals simultaneously. The strong signal enhancement of SERS (compared to spontaneous Raman scattering) also allows for significantly shorter integration times while still maintaining sufficient signal intensity. This advantage

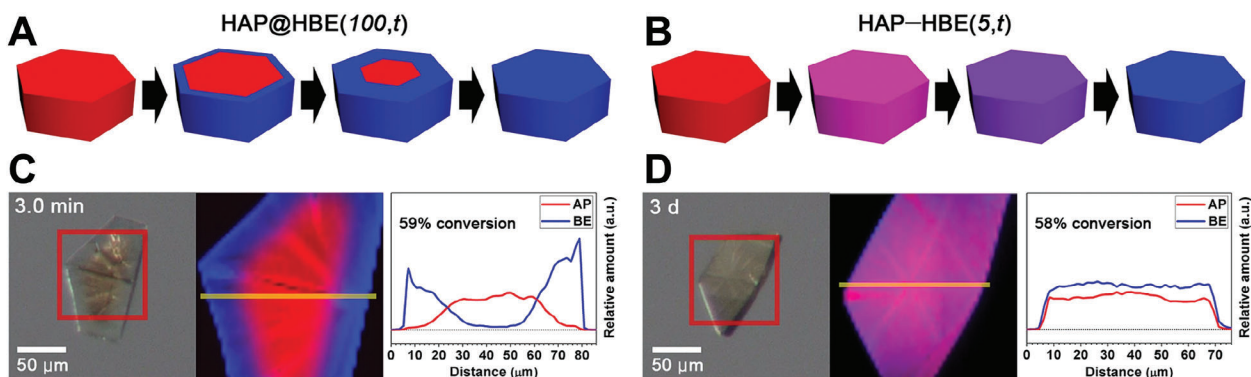


Figure 30. Raman maps of AP and BE pillars during exchange processes. A) Schematic diagram illustrating the distribution of AP (red) and BE (blue) during the exchange at 100 °C. It shows a concentric pillar distribution, representing core-shell intermediates formed as BE gradually replaces AP. B) Schematic diagram of AP (red) and BP (blue) distribution during the exchange at 5 °C showing uniform pillar distributions. C) Optical Photographs, Raman maps, and relative amounts of AP and BE pillars after 3 min at 59% conversion showing a concentric pillar distribution and core-shell conformation. D) Optical photographs, Raman maps, and relative amounts of AP and BE pillars after 3 days at 58% conversion showing a uniform pillar distribution. Adopted and reproduced under the terms of the Creative Common Attribution 4.0 Int. (CC-BY 4.0) License.^[25b] Copyright 2022, The Authors, Published by Springer Nature.

facilitates time-resolved measurements with reasonable resolution, enabling the study of dynamic processes. For the detection of low-concentration species in gas mixtures, Yang et al. developed a special prism array with Ag@ZIF-8 core-shell nanocubes deposited on the prism surfaces for SERS detection (Figure 31).^[101a] The prism array drastically increased the number of collisions of gas molecules with other prisms and the Ag@ZIF-8 nanocubes on the prisms' surface. The porous ZIF-8 layer slows down the gas molecules, while a thin layer of recognition molecules (e.g., cysteamine) around the Ag core binds the analyte molecules to the Ag nanocubes, enabling SERS measurements.

With this approach, the researchers could simultaneously measure the concentration of benzaldehyde, 3-ethyl-benzaldehyde, and glutaraldehyde species in a gas mixture. The lower detection limit for benzaldehyde and 3-ethyl-benzaldehyde reached as low as 1 part per billion (ppb).

4.6. Non-Invasiveness

Stand-off Raman spectroscopy can analyze dangerous or fragile untreated samples via physically separated instrumentation,

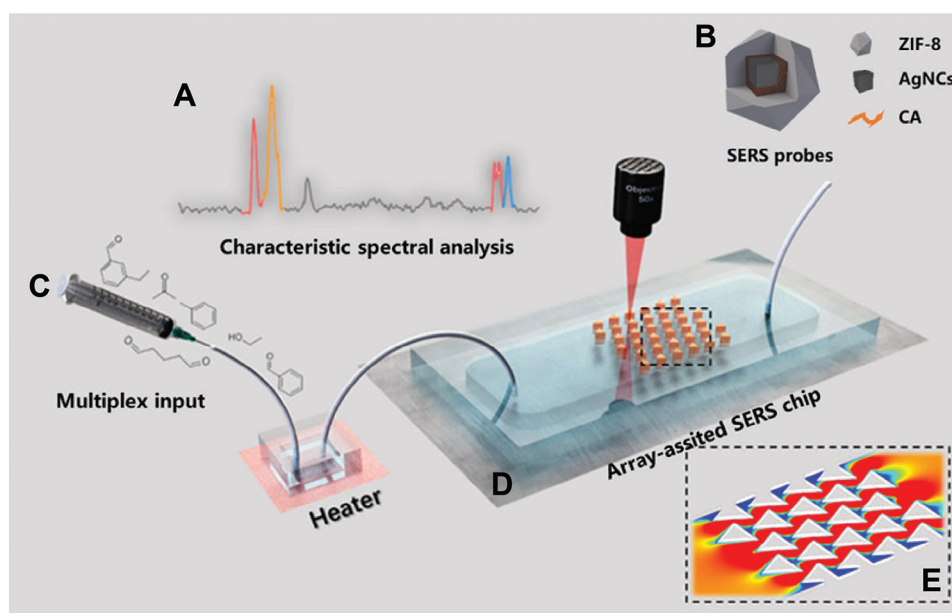


Figure 31. Schematic of the array-assisted SERS chip for gas sensing. A) Spectrum depicting the detection of multiplex aldehydes using the label-free SERS method. B) Design of Ag@ZIF-8 nanocubes. C) The mixture of analytes is pumped into a slot anchored on a heating plate to evaporate the compounds. D) Gaseous analytes flow through the SERS array chip. E) Simulations show the gas flow in a co-directional triangular prism array. Reproduced with permission.^[101a] Copyright 2020, American Chemical Society.

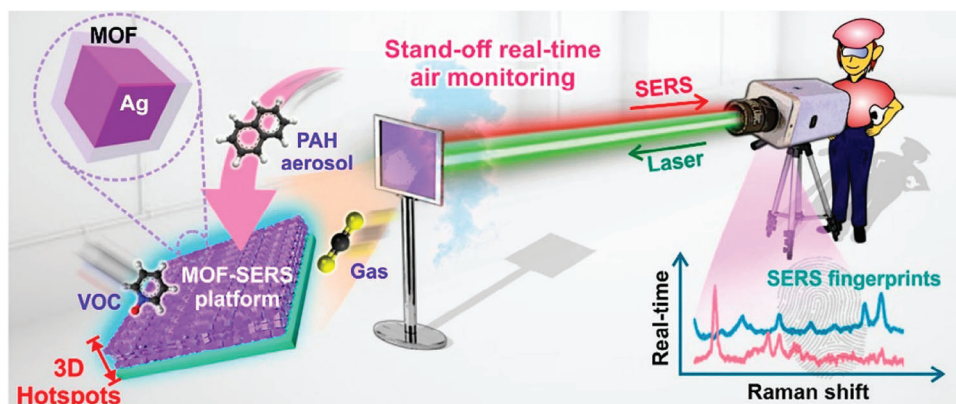


Figure 32. Overview Schematic Display of The Stand-Off MOF-SERS Platform for Real-Time Air Monitoring. Left: Schematic of the SERS active substrate and a zoom-in to a single Ag-ZIF-8 core-shell cube. Middle: The SERS substrate being measured from a safe distance. Right: Exemplary SERS fingerprint spectra. Reproduced with permission.^[101b] Copyright 2019, American Chemical Society.

providing a safe distance between the sample and the measurement system.^[158a] Phan-Quang et al. implemented a novel approach by growing a 44 nm thick layer of ZIF-8 around 120 nm long gold nanocubes, forming Ag-ZIF-8 core-shell tubes.^[101b] These core-shell structures were then self-assembled into 1.3 μm thick substrates comprising 10–15 layers of the single core-shell units. This assembly technique resulted in the formation of multiple “hotspots” of the electromagnetic field between the gold nanocubes and consequently led to a significant EM SERS enhancement. The functionality of the SERS substrate was initially validated by measuring the spectra of 4-methylbenzenethiol at different concentrations. The results demonstrated good linearity between the SERS intensity and the concentration of the analyte within the range of 50 to 0.5 parts per billion (ppb). This indicated the substrate’s capability for sensitive and quantitative analysis. Moreover, the researcher successfully applied their substrate to monitor CO_2 , (poly)cyclic aromatic hydrocarbons (PAH), naphthalene, and toluene in the air at distances of up to 10 m (**Figure 32**). Remarkably, these measurements were conducted during the day despite the substantial background due to daylight.

4.7. Guidelines

So, how do we choose a Raman technique for our MOF system? The applicability of Raman techniques depends on the precise MOF structure, its optical responses, stability, and the scientific question that shall be answered. Generally, all Raman techniques provide chemical sensitivity to the framework, metals, ligands, and functional groups of MOFs. They will monitor the interaction and response of a MOF system with guest molecules by observing the shifting, appearing, and disappearing of bands in the spectrum, however, under specific requirements. A quick overview of the prerequisites, advantages, and limitations of each technique is given in **Table 3** and discussed in the following section. For more details, please refer to Sections 2 and 3.

Spontaneous Raman scattering signal scales linearly with the number of molecules present inside the observation volume, making it a quantitative alternative to gravimetric and volumet-

ric techniques at high concentrations. Additionally, Raman scattering provides a spatial resolution down to 200 to 400 nm, depending on the excitation wavelength. The main drawback of spontaneous Raman scattering is the low scattering cross section and the resulting low signal. Consequently, it is difficult to detect molecules that are exceptionally weak Raman scatterers, and/or present in low concentration. This limitation can be partially ameliorated through an increase in laser power, sample volume/concentration, and/or an extension of measurement duration, which is usually in the second to minute range limiting in operando applications. Similarly, increased laser power can lead to photo-induced stress, structural damage to the MOF framework, protracted measurement durations, and compromised temporal resolution.

For little scattering MOF systems or applications that require high time resolution and/or increased concentration sensitivity, enhanced Raman processes are necessary. The first mechanism that can alleviate this problem is RRS since it employs the same equipment as used for spontaneous Raman measurements. A major requirement, however, is that the MOF system under investigation exhibits suitable electronic transitions that are energetically close to the exciting laser frequency. This can be achieved by tuning the wavelength of the Raman laser close to the electronic resonance. In a noticeable study by Petersen et al., RRS could elucidate the crystal growth of a MOF system $[\text{Co}_2(\text{bpy})_3(\text{NO}_3)_4]_n$ made of cobalt(II) nitrate and 4,4'-bipyridine (bpy) by monitoring the nucleation process.^[159] The researchers demonstrated that RRS is applicable for investigating MOFs made by bpy or related pyridyl-based ligands since their $\pi\text{-}\pi^*$ electronic transition in the UV provides strong RR enhancement for excitation in the UV (≈ 220 nm). Interestingly, larger amounts of soluble Co^{2+} -bpy species were formed in the solution prior to crystal growth. While an electronic resonance can lead to enhanced signals, it is frequently connected to enhanced fluorescence, obscuring the Raman transitions. Furthermore, it can disturb the linear dependence on laser intensity and concentration. For quantitative measurements, it is advisable, in particular, for photo-active MOFs to monitor the signal dependence with respect to wavelength, excitation power, and sample concentration.

If there are no suitable electronic transitions for RRS available or if single-molecule sensitivity is required, SERS spectroscopy is the method of choice. While SERS is usually recorded on a conventional Raman system, it demands advanced sample preparation techniques to bring the analyte (MOF or guest molecule) in close proximity to a SERS active material, limiting its application. Further on, the SERS signal dependence on the concentration is not always quantitative at first due to the nonlinear enhancement of Raman resonances depending on their spectral proximity to the plasmon resonance of the employed substrate and requires careful calibration. An advantage of MOFs is their function as local concentrators. SERS can benefit from MOFs with high affinity and specificity that provide high concentration while bringing the analyte close to the active material on the metal surface (see Section 2.2.2) to reach high sensitivity and time resolution as a prerequisite for sensing measurements. This sensitivity could be theoretically further linked with high spatial resolution when using TERS. As described in Section 3, TERS enables chemically sensitive scanning of surfaces with 20 to 30 nm resolution and often a signal enhancement of up to 6 orders of magnitude. To the best of our knowledge, TERS was not utilized to measure MOFs yet, which may be due to the specialized instrumentation.^[65]

Lastly, CRS provides significant signal enhancement independent of electronic or plasmonic resonances, however, at the expense of advanced and costly instrumentation. CRS is suitable for fast chemical sensitive 2D or 3D imaging to highlight, e.g., the heterogeneity of crystals or the distribution of guest molecules or defects within.^[64] The frame rate of CRS compared to conventional Raman mapping is increased from hours per frame to multiple frames per second with comparable spatial resolution (see Section 2). While fluorescence is usually a minor issue for CRS, CARS suffers particularly from a strong non-resonant background due to the solid-state nature of MOFs. Lastly, it is important to note that the high-power laser pulses that are required for CRS excitation may lead to damage in the MOF for some samples.

5. Applications of Raman Imaging to Address Societal Needs

Given the challenges we currently face in our world, such as climate change, resource scarcity, and environmental pollution,

there is a growing need for sustainable chemistry and applications for addressing societal needs. MOFs have captured the attention of researchers and scientists as a potential solution due to their tunable properties, high selectivity, and potential for environmentally friendly applications. In this section, we wish to outline how Raman spectroscopy contributes to the characterization and design of new MOF-based materials for environmental remediation, healthcare, and energy storage. A short overview of applications is given in **Table 4** and discussed in detail in the following section.

5.1. MOFs for Generating Pure Water

Water is an essential part of life. Organisms are made of it, live in it, or drink it. Yet access to clean, fresh, and safe water remains a challenge for a significant portion of the global population. MOFs exhibit high porosity, large surface areas, and exceptional adsorption capabilities, making them ideal candidates for water treatment applications. The unique properties of MOFs allow for the selective removal of contaminants,^[169] such as heavy metals,^[170] antibiotics and pesticides,^[171] dyes,^[172] and even microorganisms^[173] from water sources. Catalysis is another strategy to generate clean water. Here, MOFs can support the purification mechanism by adsorption and photocatalytic decomposition.^[174] One of the key advantages of MOFs is their regeneration and reusability, making them economically viable and sustainable for long-term water treatment solutions.^[170b] In addition to their adsorption selectivity, MOFs can be tailored to specific pore sizes, turning them into excellent materials for membranes with nano-, meso- and macropores. These membranes can be utilized for the removal of contaminants but also desalination and nanofiltration.^[173,175] A recent study by Han et al. developed MOF-Graphene composite membranes that allow for solar-driven seawater desalination with nearly 98% solar-to-thermal efficiency.^[175] Confocal Raman microspectroscopy could confirm that the graphene layer was correctly embedded within the MOF.

Other exciting directions are water harvesting applications from the air. Water scarcity is a pressing issue in arid regions such as Africa and the Middle East, where access to clean and drinkable water is limited. Here, groundwater, the main source of drinkable water, is often contaminated with salt, heavy metals, chemicals, and pollutants from industrial and agricultural

Table 3. Raman techniques overview. Advantages and limitations. Abbreviations: Background (Bg); Not applicable (N.A).

	spRaman	RRS	SERS	TERS	CARS	SRS
Enhancement	–	10^{3-4} ($<10^6$)	10^{4-10} ($<10^{11}$)	$\approx 10^6$	$\approx 10^{7-8}$	$\approx 10^{7-8}$
Fluorescence	High Bg	Electronic transition required	High Bg	High Bg	Usually None	Usually None
Setup complexity	Simple	Simple	Simple	Advanced	Advanced	Advanced
Sample preparation	Simple	Simple	Advanced	Advanced	Simple	Simple
Scanning	3D	3D	N.A.	2D	3D	3D
Spatial resolution	200–400 nm	200–400 nm	200–400 nm	20–30 nm	200–400 nm	200–400 nm
Acquisition time / pixel	≈ 1 min	≈ 1 ms			$\geq \mu$ s	$\geq \mu$ s
Quantitative	Yes	Mainly	Mainly	Yes	Usually not	Yes

Table 4. Summary of MOFs probed by Raman techniques.

Applications	Year	MOF structure	Analytes	Key-findings	Method	Source
Water harvesting	2023	Zr MOF-801	H ₂ O	AWH performance is affected by intra- and interparticle effects	CARS	[64b]
	2022	Zr MOF-801	H ₂ O	Missing metal clusters are a further source of localized water adsorption and condensation	spRaman	[64a]
Gas separation	2012	RPM3-Zn	Paraffin	Selective separation of C1-C4 paraffin and two pairs of C2 isomers	spRaman	[61c]
Gas storage	2022	UiO-66(Cu)	NH ₃	Enhanced ammonia adsorption on defective UiO-66-Cu(II)	spRaman	[160]
Photo-catalytic reduction	2023	AgNC + MOF-801	CO ₂	Nanocomposites for photocatalytic reduction	spRaman	[161]
Biomedical degradation	2017	MIL-100(Fe)	MIL-100(Fe)	Degradation of carboxylate nano- and microparticles in simulated body fluid	spRaman	[162]
	2020	MIL-100(Fe)	–	Extracellular pH influences the speed of NP degradation leading to pyroptosis	spRaman	[163]
Drug release	2019	Au-nanostar + ZIF-8	HOECHST	Delivery of bioactive molecules via a thermoplastic-driven release mechanism	SERS	[164]
Energy storage	2020	Ni/MOFDC	–	Defect introduction after removal of passive Ni(OH) ₂ for aqueous battery-type energy storage	spRaman	[165]
	2021	ZIF-8	–	Solid-state gas-steamed MOF approach, designed to fabricate carbon cages	spRaman	[166]
Hazardous substance sensing	2021	UiO-67	Nitro-analytes	Detection of nitro-based explosives from vapor	spRaman	[167]
	2018	ZIF-8	Organic compounds	Detection of volatile organic compounds and polycyclic aromatic hydrocarbons	SERS	[100]
Biomedical sensing	2014	AuNPs/MIL-101	α -Fetoprotein	Nanocomposites for detection of α -Fetoprotein	SERS	[62c]
	2018	Core-Shell GSP/ZIF-8	4-Ethylbenz-aldehyde	SERS detection of 4-Ethylbenzaldehyde	SERS	[29f]
	2015	AgNPs@MIL-101	Dopamine	SERS detection of dopamine	SERS	[168]
	2016	Au tetrapods @IRMOF-3	Peptides	SERS detection of N-terminal pro-brain natriuretic peptide	SERS	[158b]
Food safety	2014	AuNP/MIL-101	p-Phenylene-diamine	SERS detection of p-phenylenediamine	SERS	[62c]
	2018	Core-Shell	Methenamine	SERS detection of methenamine	SERS	[101c]
	2020	Au/MIL-101 AuNPs@UiO-66-NH ₂	Coccine Dye Orange II	SERS detection of New Coccine and Orange II Dyes	SERS	[99]

activities. MOFs offer a versatile solution to address these challenges. MOF materials can absorb water in a low-humidity environment and harvest water from the air. Until now, more than 20 types of MOFs, including MOF-303, MOF-801, or MOF-808, showing high affinity to H₂O molecules were reported.^[170b] MOF-801 [Zr₆O₄(OH)₄(fumarate)₆] established itself due to excellent water adsorption properties and high chemical stability.^[176] It is meanwhile used in different water harvesting devices, some even relying on fluidized bed reactors that facilitate water desorption.^[177] Another technical development to increase water production could be core-shell MOF composites, such as CaCl₂-encapsulated Fe-ferrocene MOF hollow microspheres.^[178] This arrangement facilitates the photothermal release and the overall adsorption of water molecules.

Compared to other materials, MOF-801 has an outstanding water adsorption capacity of 0.28–0.4 g of water per g of dry MOF between 20–90% RH. Benchmarking the uptake of crys-

talline material, however, is commonly done at the bulk level by gravimetric assays. These characterizations can be extended with Raman spectroscopy and CARS microscopy to monitor individual particles in situ, generating valuable insights into the behavior at the single crystal level. Fuchs and Knechtel et al. developed a novel methodology based on Raman spectroscopy (**Figure 33**), enabling the acquisition of single-particle water adsorption isotherms and kinetic curves with sub-micrometer resolution.^[64b] The noninvasive nature of correlative Raman imaging and spectroscopy revealed that the water harvesting performance of MOF-801 is strongly affected by intra- and interparticle effects. Four-Wave-Mixing (FWM) and CARS imaging could localize water molecules and identify interparticle condensation as a major contribution. Spontaneous Raman scattering determined quantitatively a significantly faster kinetic for single crystals. These studies indicate an upper limit of around 91.9 L/kgMOF/day for MOF-801.

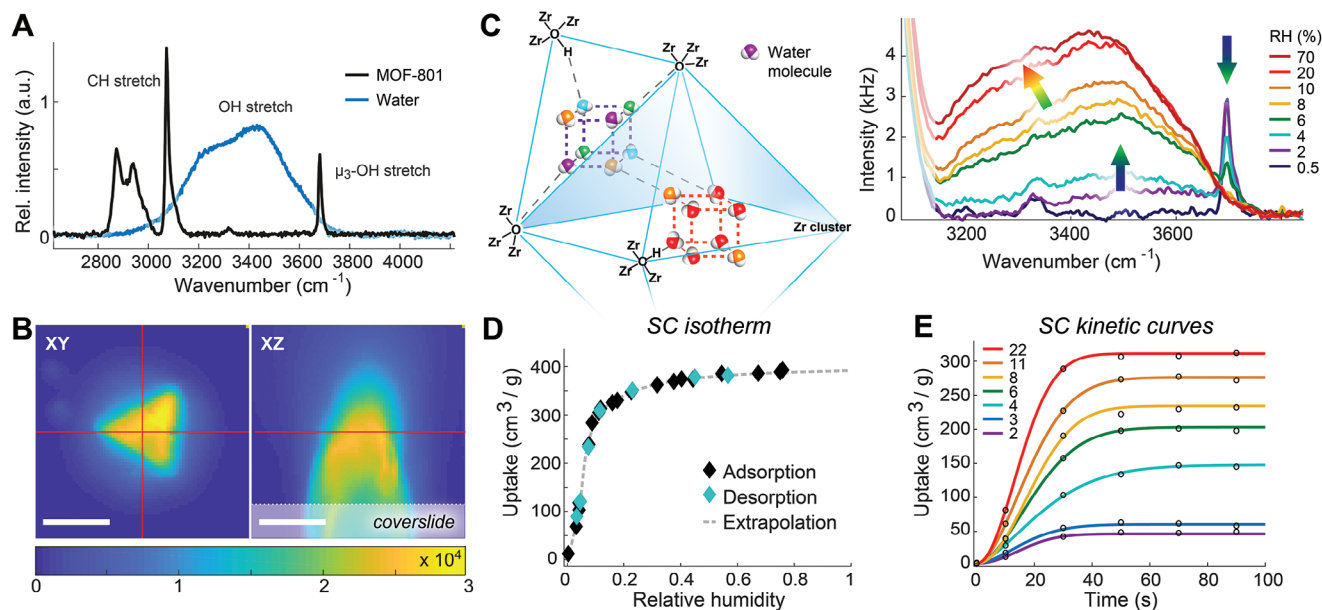


Figure 33. Water uptake in MOF-801 crystals was monitored by Raman spectroscopy. A) Raman spectra of dry MOF-801 and water. B) Raman image based on the C=C stretch vibration at 1670 cm^{-1} in XY and XZ plane showing an isolated single MOF-801 crystal. Red lines mark the position for recording SC isotherms and kinetics in (D). Scale bar: $5\text{ }\mu\text{m}$. C) Raman spectra of MOF-801 at increasing relative humidity (RH) confirm consecutive binding of water molecules in the tetrahedral (purple dotted cube) and octahedral (red dotted cube) binding sites of the crystal structure. D) Absolute water uptake of single crystal (SC) MOF-801 derived from the ratiometric Raman analysis at varying humidity. Adsorption (black) and desorption (cyan) are reversible. E) Kinetic of water uptake within the same crystal after exposure to selected relative humidities. The uptake saturates in less than 60 s. Adopted and reproduced under the terms of the Creative Common Attribution 4.0 Int. (CC-BY 4.0) License.^[64b] Copyright 2023, The Authors, Published by the American Chemical Society.

In another study by Fuchs et al., spontaneous and coherent Raman spectroscopy were employed in a correlated fashion to investigate the distribution of adsorbed H_2O molecules inside MOF-801.^[64a] Clusters of single crystals showed an inhomogeneous distribution caused by defect sites inside the material. As a result, missing linkers played only a minor role in the heterogeneity. Missing metal clusters could be identified as the source and trap of localized water adsorption and condensation (Figure 34) as seen by shifts in the Raman spectrum toward the free linker spectrum.

5.2. MOFs for Generating Pure Air

Gases play an important role in pollution, chemicals- and energy-producing industries and can threaten life. Gas separation is an essential step for capturing, purifying, and isolating specific molecules. For instance, the energy-demanding olefin/paraffin dissection is a key process in the industry for the production of chemical precursors. Hydrocarbon molecules are separated in great scales to produce fuels and chemical feedstock. MOFs, with their unique properties, show potential for energy-efficient disintegration of a high number of gases.^[179] Furthermore, the high porosity and surface area make these materials interesting candidates for storage of polluting and hazardous gases like carbon mono/dioxide or ammonia. For the efficient use of the MOF systems, an understanding of the selection mechanism and influence of the framework components is important. These parameters are accessible with Raman techniques.

5.2.1. Gas Separation

Nijem et al. investigated the selective separation of C1-C4 paraffin and two pairs of C2 isomers ($\text{C}_2\text{H}_2\text{-C}_2\text{H}_4$ and $\text{C}_2\text{H}_4\text{-C}_2\text{H}_6$) in the flexible framework RPM3-Zn with Raman spectroscopy (Figure 35). Flexible MOFs display promising hydrocarbon selectivity based on gate-opening pressures. This mechanism is observable in the Raman spectrum by H-bonding between terminal groups and the C=O bond of the BDC linker. As a result, stronger H-bonding reduces the gate-opening pressure.^[61c]

5.2.2. Gas Storage

The understanding of interactions between guest molecules and metal-organic frameworks (MOFs) at an atomic level is crucial for optimizing their adsorption and catalytic performance. Ma et al. employed Raman spectroscopy to investigate the binding of ammonia (NH_3) to different types of UiO-66 MOFs, specifically UiO-66-Cu(I) and UiO-66-Cu(II) (Figure 36).^[160] Despite having similar properties, such as the area and the amount of -OH functional groups, the defective UiO-66-Cu(II) crystals exhibited enhanced ammonia adsorption compared to their counterparts. The enhanced adsorption was attributed to a dynamic adsorption mechanism involving a $[\text{Cu(II)} \cdots \text{NH}_3]$ interaction within the defective crystals. This mechanism is challenging to observe using conventional techniques due to the invisibility of protons in NH_3 for X-ray analysis and the complex and rapid host-guest dynamics involved in adsorption. Raman spectroscopy revealed changes

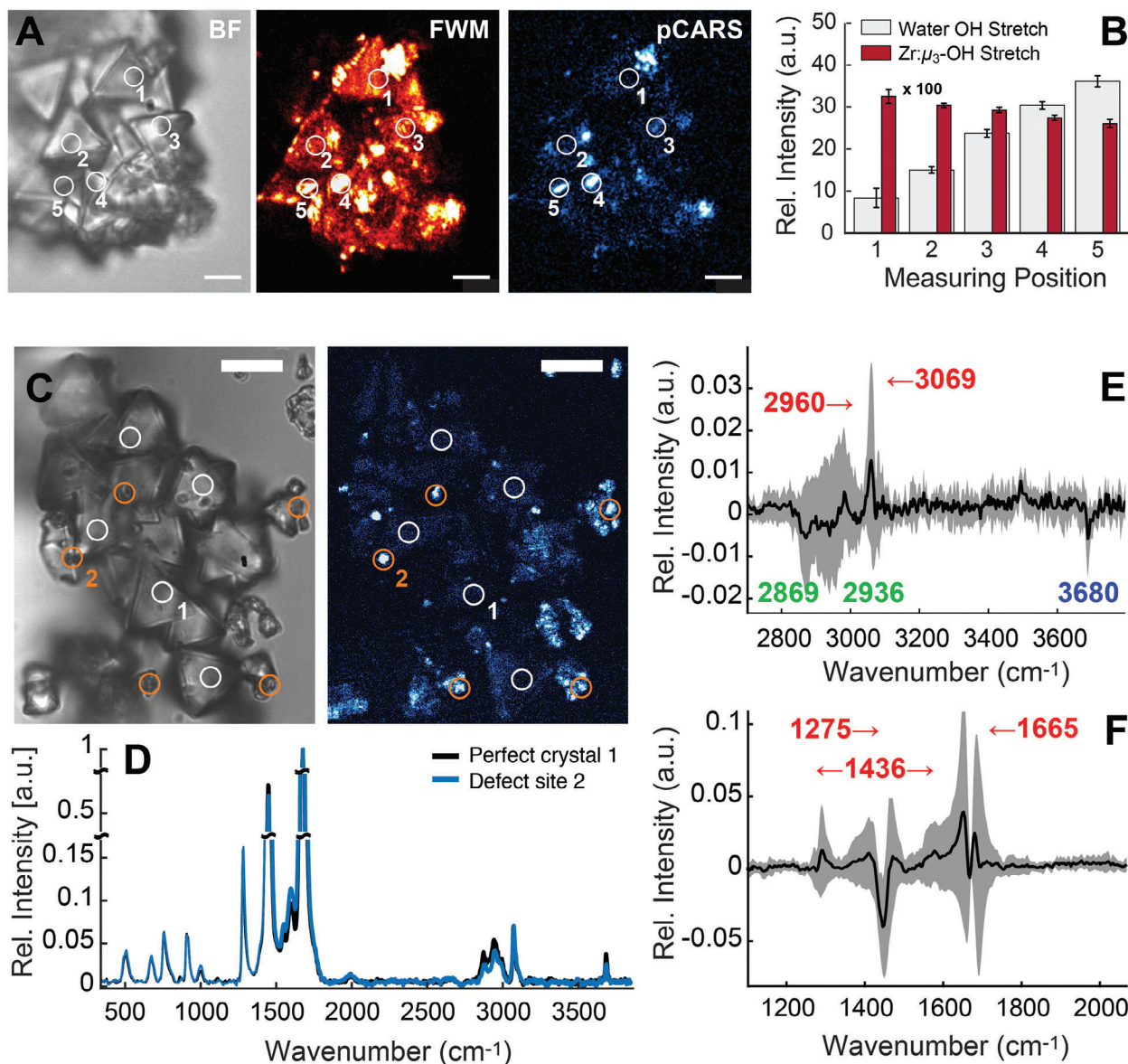


Figure 34. Chemical characterization of water clusters in MOF-801. A) Water distribution in MOF-801 crystals visualized by brightfield, FWM, and pCARS imaging at 10%RH. Numbered circles indicate measurement points in (B). Scale bar: 2 μm. B) Relative amount of adsorbed water observed by Raman spectroscopy at selected areas in panel (A). C–F) Correlative characterization of areas with enhanced water incorporation by (C) pCARS imaging and (D–F) spontaneous Raman spectroscopy. C) Water cluster sites in regular crystals were identified by pCARS imaging at 38.5%RH. D) Raman spectra at positions 1 and 2 marked in (C). E, F) Difference spectra between the Raman signature at defect sides and sites of normal crystal growth in the fingerprint region (F) and C–H stretch to water region I. Differences due to missing clusters (blue) and concomitant reduction in residual DMF (green) and uncaging of fumaric acid (red) are marked for the corresponding resonances. Arrows indicate the direction of spectral shift. Adopted and reproduced under the terms of the Creative Common Attribution 4.0 Int. (CC-BY 4.0) License.^[64a] Copyright 2022, The Authors, Published by Wiley-VCH.

in the OH-stretch band at 3673 and 3646 cm⁻¹, indicating depletion upon increasing ammonia adsorption. The NH₃ molecules were found to bind to the μ₃-OH and defect-OH sites within the MOF structure. Notably, a new band appeared at 1617 cm⁻¹, representing the asymmetric vibration of the adsorbed NH₃. This study highlights the power of Raman spectroscopy in elucidating the intricate molecular interactions within MOFs, offering valuable insights for optimizing their adsorption and catalytic properties.

5.2.3. Photocatalytic reduction

The capture and conversion of greenhouse gases, particularly CO₂, plays a crucial role in combating pollution and reducing emissions. Noble metal nanocrystals have shown remarkable potential for efficient conversion through localized surface plasmon resonances, which can trigger or accelerate a wide range of reactions. Liu et al. combined the high CO₂ reduction reactivity of silver nanocrystals (AgNC) with the good CO₂

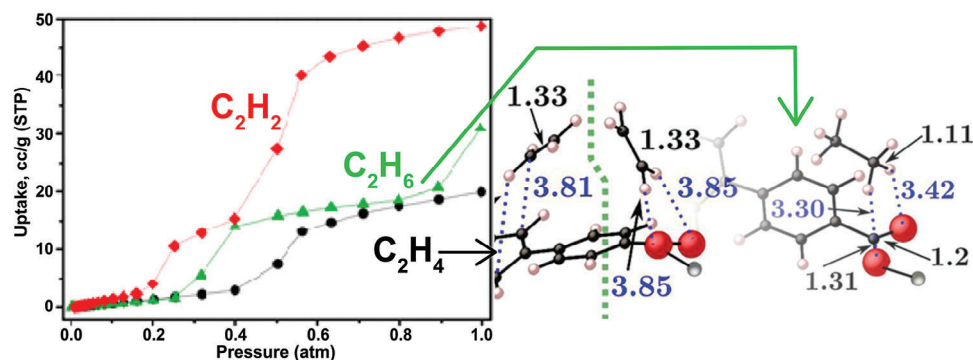


Figure 35. Hydrocarbon selectivity based on gate opening pressure. Flexible framework RPM3-Zn shows selective adsorption based on chain length and specific framework-gas interaction. Reproduced with permission.^[61c] Copyright 2012, American Chemical Society.

adsorption capability of MOF-801 to create nanocomposites for photocatalytic reduction.^[161] They characterized the performance of different composites (core-shell and corner MOF-AgNC) with in situ Raman spectroscopy. Initially, Raman scattering was employed to confirm the successful coating of silver nanocrystals with mercaptopropionic acid (MPA) and the formation of MOF-AgNC. The composites showed bands for -CH, -OH, and O-C-O out of plane bending at 668 cm^{-1} , O-C-O rocking modes at 761 cm^{-1} , stretching vibrational modes of C-O and rocking CH at 1227 cm^{-1} , as well as the stretching vibrational modes of O-C-O and C-C at 1438 cm^{-1} and 1661 cm^{-1} , respectively. Notably, the asymmetric vibration of CO_2 at 1550 cm^{-1} provided a means to determine the CO_2 concentration. Exponential saturated adsorption was detected. After the irradiation with violet light ($420 - 460\text{ nm}$, **Figure 37A**), to create the localized surface plasmons, a band at 1642 cm^{-1} appeared in the spectrum of the core-shell nanocomposite. This band was attributed to the generation of CO from the photocatalytic reduction reaction (**Figure 37B,C**). In the case of the corner MOF-AgNC, a band at 1158 cm^{-1} , assigned to the CH wagging of HCOO^- , appeared. This suggests that, depending on the morphology and environment, different conversion mechanisms take place transforming CO_2 into climate-friendly CO or HCOOH. Additionally, the reactivity could be increased by increasing the intensity of the incident irradiation light (**Figure 37D-F**). This approach provides the possibility for designing photocatalysts for various reactions.



Figure 36. Ammonia adsorption in UiO-66 and defective UiO-66. Defective UiO-66 metal-organic frameworks show enhanced NH_3 uptake and dynamics. Reproduced with permission.^[160] Copyright 2022 American Chemical Society.

5.3. MOFs for Biomedical Applications

In biomedical applications, the controlled release of drugs at the site of the disease is a great chance to reduce negative side effects and increase the healing result. Drug nanocarriers suffer from limitations like a low loading capacity (liposomes, micelles) or toxicity and unacceptable degradation (inorganic materials). MOFs feature a versatile structure with stimuli-responsive, controlled drug release, a high porosity, and biodegradability via weak coordination bonds.^[180]

5.3.1. MOF Degradation

Understanding the degradation mechanism of MOF-based nanocarriers is crucial to ensure their safety and minimize potential negative effects on patients. In a study by Li et al., Raman spectroscopy was employed to investigate the degradation of carboxylate nano- and microparticles in simulated body fluid.^[162] The high spatial resolution offered by Raman spectroscopy allowed for the simultaneous analysis of morphology and chemical composition within the same MIL-100(Fe) particle in a phosphate-containing medium. The Raman spectrum exhibited characteristic peaks corresponding to the ordered crystalline iron-based structure at 210 cm^{-1} , lattice vibration and network binding modes at $450 - 600\text{ cm}^{-1}$, the trimesate linker at 800 cm^{-1} , aromatic ring peaks at 1000 cm^{-1} , C-O-Fe stretching of Ferrimesate at 1200 cm^{-1} and H-O-H bonding vibrations at $1400 - 1600\text{ cm}^{-1}$ (**Figure 38**; brown spectrum). After eight days in phosphate-buffered saline (PBS), the MOF particles underwent degradation, forming a red core (region I) surrounded by a grey shell (region II) (**Figure 38**). The Raman spectrum of the core (**Figure 38**; red spectrum) remained similar to that of the non-degraded MOF, while the Raman spectrum of the shell lost most peaks (**Figure 38**; blue spectrum). This change in the Raman signature suggests the formation of an amorphous phase, trimesate release, and the formation of phosphate complexes. The MOF demonstrated a competitive replacement of trimesate by phosphate ions in PBS. Furthermore, Raman spectra were recorded before and after drug loading, as well as after MOF coating and no significant changes were observed, indicating the absence of degradation.

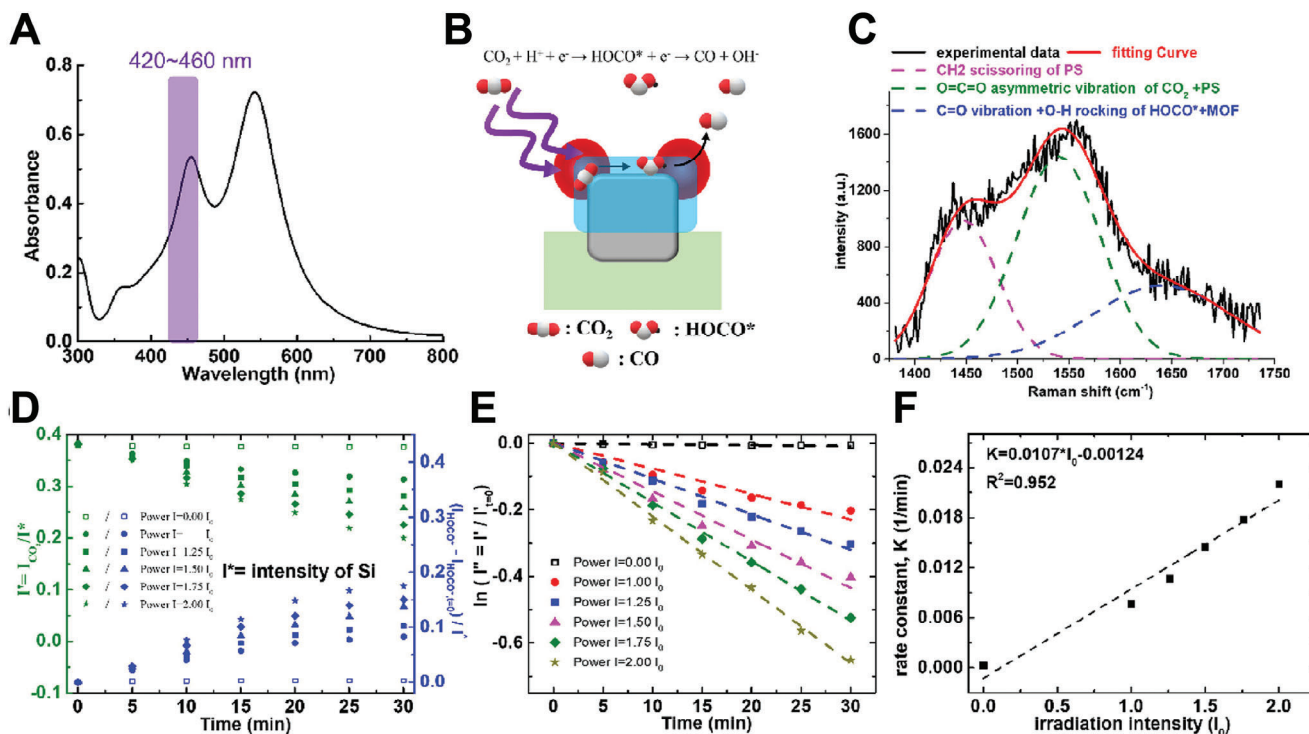


Figure 37. Core-shell MOF-AgNC nanocrystals act as photocatalysts for CO_2 reduction under the plasmon-induced electromagnetic field. A) The extinction spectrum of core-shell MOF-AgNC nanocrystals on the PS matrix reveals the hybrid quadrupole (HQ) mode around 420–460 nm, generating an electromagnetic field concentrated at the top corners of the nanocrystals. This enhanced electromagnetic field facilitates CO_2 reduction reaction, as depicted in the schematic in (B). C) The relative CO_2 concentration can be characterized by the Raman spectrum, which contains contributions from multiple materials: PS (pink dashed curve), CO_2 + PS (green dashed curve), and HOCO^* (intermediate) + MOF-801 (blue dashed curve). D) The Raman shift intensity of the CO_2 vibration mode (green labels) and the HOCO^* vibration mode (blue labels) was monitored at different times under different irradiation intensities. E) The first-order rate constant (K) of the CO_2 reduction reaction under different irradiation intensities can be obtained by the slope of the curve of $\ln(I'/I'_{t=0})$ versus time, where $I' = I_{\text{CO}_2}/I^*$ and I^* is the Raman shift intensity of the silicon substrate. F) The relationship between the rate constant and the irradiation intensity is linear. The intensity of irradiation $I_0 = 1.29 \text{ W cm}^{-2}$. Reprinted with permission.^[161] Copyright 2023, American Chemical Society.

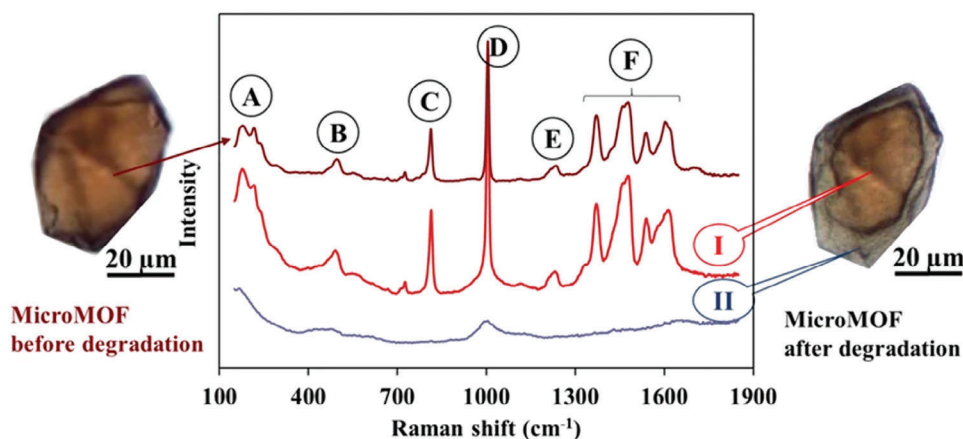


Figure 38. Investigation of MOF degradation by Raman. Raman spectra of a single microMOF particle of around 50 microns before (brown) and after (red and blue) degradation for eight days in PBS (11.9 mM). Raman spectra were recorded on the same particle, both in the red core (region I) and the degraded grey shell (region II). Adopted and reproduced under the terms of the Creative Common Attribution 4.0 Int. (CC-BY 4.0) License.^[162] Copyright 2017, The Authors, Published by Springer Nature.

In another example, Ploetz et al. found out that biodegradable MIL-100(Fe) nanoparticles can induce pyroptosis, a programmed cell death mechanism, in cells.^[163] While these MOF nanoparticles are easily tolerable by cells under physiological conditions,^[13c] the researchers demonstrated that the pH of the extracellular environment plays a crucial role in the activation of pyroptosis by MOF nanoparticles. Using Raman spectroscopy, they found out that a slightly acidic environment, as it is present in tumorous tissue, leads to a shift in redox potential inside the cell. Consecutively, MOF nanoparticles are faster degraded in lysosomes, releasing iron ions in an uncontrolled fashion. This study highlights the potential of MOF nanoparticles as a pH-responsive platform for targeted cell death applications.

5.3.2. Monitoring the Release

Plasmonic core-shell gold nanostar/zeolitic-imidazolate framework 8 (ZIF-8) nanocomposites were synthesized by Carrillo-Carrión et al. for the delivery of bioactive molecules (Figure 39).^[164] The composite material features a thermoplastic-driven release mechanism of encapsulated cargo. The loading, leakage, and delivery of the fluorescence stain HOECHST H33258 (HOE) were followed by SERS and confocal Raman microscopy. The study investigated both uncoated composites with and without illumination at 785 nm, as well as a version of the carrier coated with an amphiphilic polymer, poly[isobutylene-alt-maleic anhydride]-graft-dodecyl (PMA). In the case of uncoated ZIF-8, no HOE signal was detected, indicating framework degradation prior to cell uptake. However, the PMA-coated composite exhibited a clear HOE signal in specific regions before illumination. After 8 hours of illumination, the signal disappeared, confirming complete cargo release. In contrast, the condition without illumination showed a persistent HOE signal after 8 hours, indicating the integrity of the ZIF-8 framework. The SERS data correlated well with the confocal microscopy measurements, which showed MOF accumulation near the nuclei without staining the nuclei, indicating no leakage. The near-infrared-induced drug release resulted in staining of the nuclei, demonstrating the effectiveness of the delivery system.

5.4. MOFs for Energy Storage Applications

The demand for efficient and sustainable energy storage systems has grown with the increasing need for renewable energy sources and the growing concerns about climate change. To address these challenges, new materials and technologies that can store and deliver energy in a reliable and environmentally friendly manner are important. Metal-organic frameworks and MOF derivatives like porous carbons show great performance in energy storage and conversion applications.^[181]

5.4.1. Battery-Type Energy Storage

Mofokeng et al. introduced a Ni/MOF-derived mesoporous carbon (Ni/MOFDC) as a material for aqueous battery-type energy storage.^[165] Besides other X-ray or electron-based methods, Raman spectroscopy was employed to investigate the material. The

MOF was examined before and after acid treatment (AT). In the Ni/MOFDC spectrum, a Ni-OH band was observed at 487 cm⁻¹, along with D, G, and 2D bands at 1350, 1599, and 2450 cm⁻¹, respectively, originating from MOFDC. In the AT-Ni/MOF spectrum, the Ni-OH peak became flattened, and the D and G bands shifted to 1345 cm⁻¹ and 1589 cm⁻¹, respectively (Figure 40). However, no changes were observed in the 2D band. Based on these observations, it can be inferred that the acid treatment resulted in the removal of a passive Ni(OH)₂ layer and the generation of defects in the material.

5.4.2. Energy Storage

Carbon micro- and nanocages have emerged as highly promising systems for electrochemical energy storage. In an innovative study, Hou et al. developed a solid-state gas-steamed MOF approach to synthesize carbon cages with controlled openings and N, P dopants.^[166] Raman spectroscopy played a crucial role in characterizing the material, particularly through the intensity ratio (*I_D*/*I_G*) of the disorder-induced D band (≈1350 cm⁻¹) to the tangential stretch G band (≈1600 cm⁻¹). The open carbon cage OCC-900 and the solid carbon polyhedron SCP-900 exhibited enhanced ratios of 1.26 and 1.13, respectively, suggesting decreased graphitization and an abundance of structural defects in OCCs following P doping. Furthermore, the research group successfully demonstrated the remarkable performance of an aqueous zinc-ion hybrid supercapacitor based on these carbon cages.

5.5. MOFs as Sensors

The detection of trace amounts plays a crucial role in addressing various societal challenges. Whether it is monitoring gases, hazardous substances, or biological factors, accurately detecting and quantifying these trace components is of utmost importance. However, it remains a significant challenge to develop techniques that can effectively lower the concentration limit or artificially increase the local concentration to achieve sensitive detection. The development of such techniques is essential to ensure environmental safety, public health, and overall well-being, and MOFs could be a key.

5.5.1. Hazardous substances (Air/water)

Raman spectroscopy offers a highly sensitive, selective, rapid, and reversible method for detecting molecules in the vapor phase. Recently, this technique has been successfully employed to detect molecules adsorbed on MOF UiO-67 under ambient conditions (Figure 41).^[167] The detection mechanism is based on the quenching of Raman intensity observed in specific bands. When various nitro analytes were adsorbed, a significant quenching effect of up to 50% was observed within ≈5 s, and up to 90% quenching was achieved after 30 seconds. This quenching effect is attributed to π-π interactions between the adsorbents and the benzene rings of the MOF. Importantly, UiO-67 demonstrates excellent stability and reversibility, making it a reliable sensor for the detection of nitro-based explosives. The use of Raman spectroscopy in conjunction with MOFs holds great potential for sensitive and selective detection applications.

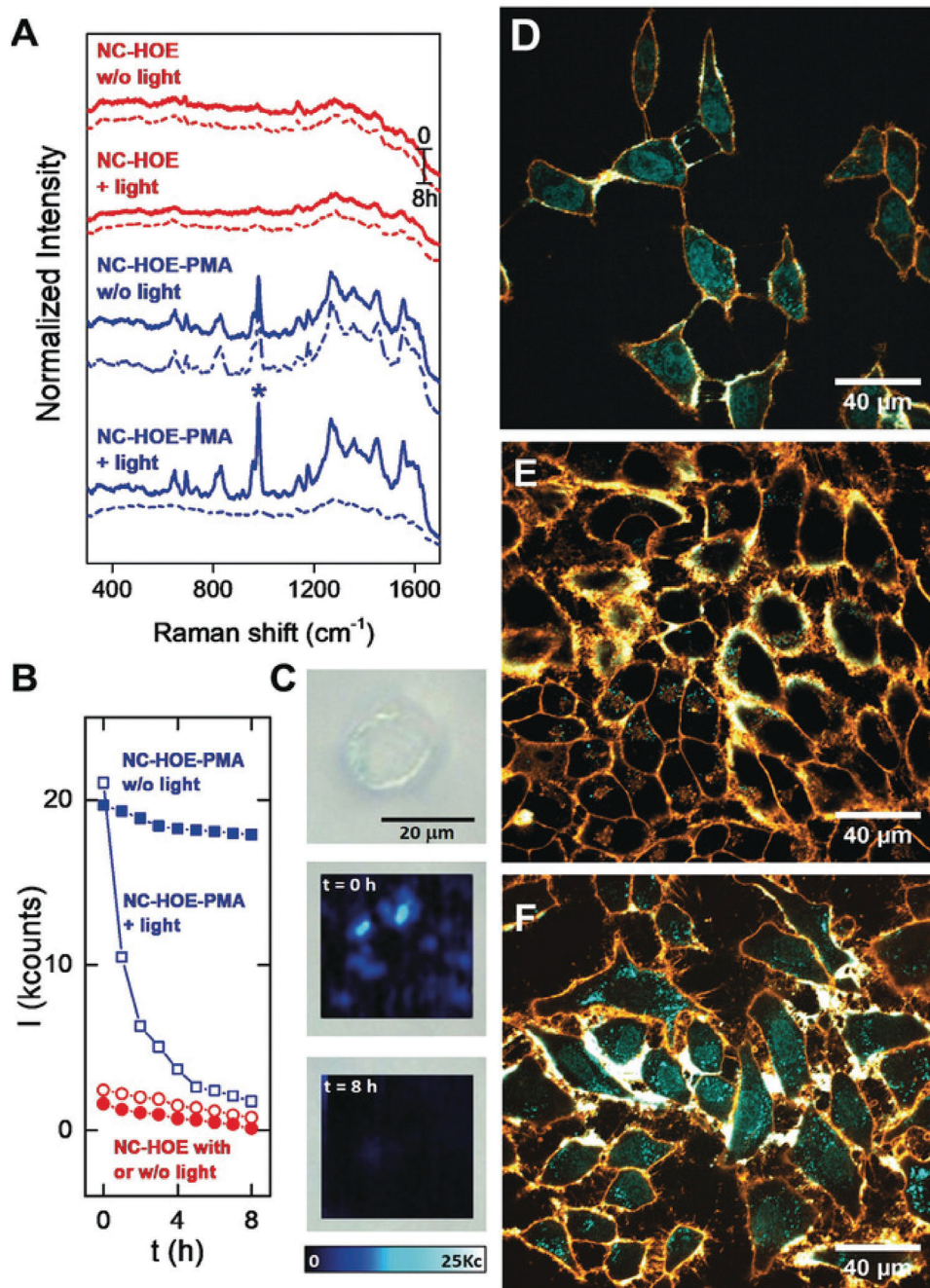


Figure 39. Monitoring of drug release and particle stability. A) SERS spectra of the NCs after cell incubation. Spectral kinetics were acquired with and without NIR illumination (785 nm); solid and dashed lines represent the time points 0 h and 8 h, respectively. B) SERS intensity of the ring breathing vibration of HOE (980 cm^{-1}), as a function of time, for both materials, with and without NIR light. C) Representative SERS imaging of a single cell incubated with NC-HOE-PMA. Optical image (top) and SERS images at 0 h (middle) and after 8 h of irradiation (down). D–F) Confocal microscopy image of cells incubated with D) NC-HOE, E) NC-HOE-PMA E), and F) NC-HOE-PMA after NIR treatment. Blue and orange colors represent HOE and cell membrane staining (CellMask™ Deep Red), respectively. Reproduced with permission.^[164] Copyright 2019, Wiley-VCH.

For the detection of toxic gases in the air, Koh et al. developed a “plasmonic nose” that is able to detect a wide range of volatile organic compounds (VOCs) and polycyclic aromatic hydrocarbons (PAH) vapors in air down to ppm levels, while differentiating between different molecules based on their vibrational sig-

natures (Figure 42). This is achieved with a SERS active array of Ag nanocubes and a 146 nm thick coating of ZIF-8 to adsorb the gas molecules close to the SERS active surface. Koh et al. showed that the plasmonic nose is able to detect toluene and chloroform down to a concentration of 200 ppm and 50 ppb, respectively.^[100]

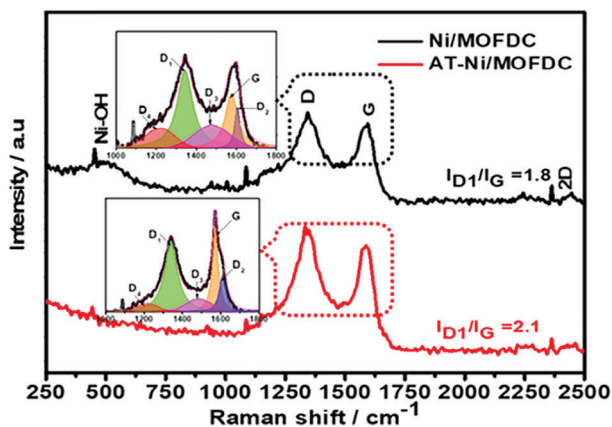


Figure 40. Raman spectra of Ni/MOFDC and AT-Ni/MOFDC. The inset shows a typical deconvoluted Raman signal of carbon. Adopted and reproduced under the terms of the Creative Commons Attribution 4.0 Int. (CC-BY 4.0) License.^[165] Copyright 2020, The Authors, Published by the American Chemical Society.

5.5.2. Medical Applications (Biomarker/Metabolites)

The timely diagnosis of diseases is crucial for effective and affordable treatment. Early detection, as stated by organizations like the World Health Organization, is an essential public health strategy for improving cancer outcomes in all healthcare settings.^[182] However, diagnosing diseases in their early stages can be challenging, as patients often do not experience noticeable symptoms, and the concentration of biomarkers indicating the illness remains low. Therefore, highly sensitive detection methods are required. In addition to sensitivity, non-invasiveness and patient safety are paramount considerations in diagnostic approaches. The use of potentially toxic labels and invasive procedures can pose risks and limit the effectiveness of diagnostic methods. Here, MOF-assisted surface-enhanced Raman spectroscopy (SERS) offers a promising solution by combining Raman spectroscopy, a non-invasive and non-destructive technique, with the high sensitivity of SERS and the local concentration enhancement provided by MOF systems. Therefore, MOF-assisted SERS represents a promising technique for early diagnosis of various diseases, offering a potential breakthrough in the field of medical diagnostics.

Hu et al. utilized the AuNPs/MIL-101 nanocomposites for the detection of Alpha-Fetoprotein (AFP) in human serum.^[62c] AFP measurement is particularly crucial during pregnancy, as elevated AFP levels can indicate developmental abnormalities in the fetus, while low levels can be indicative of conditions like trisomy 21. Abnormal AFP levels in men and non-pregnant women can also serve as potential indicators of diseases such as Hepatitis or various liver issues.^[183] The SERS-based detection of AFP using the AuNPs/MIL-101 nanocomposites demonstrated remarkable agreement with the results obtained from the well-established ELISA kit, a widely used analytical method. The normal AFP level for humans is typically around 3.0 ng mL^{-1} ,^[184] and the lowest measured AFP concentration with SERS in human serum was 2.7 ng mL^{-1} . These findings highlight the capability of SERS as a sensitive technique for detecting AFP levels, even at concentrations close to the normal range. Importantly, SERS offers the ad-

vantage of faster detection compared to established techniques, providing a more efficient and time-saving approach.

Qiao et al. conducted a study in which they successfully synthesized ordered gold superparticles (GSPs) with a size of approximately 170 nm by assembling small gold nanoparticles ($\approx 6 \text{ nm}$) in a face-centered cubic lattice. (Figure 43).^[29f] These GSPs were then coated with a layer of ZIF-8, resulting in core-shell particles referred to as GSP@ZIF-8. The researchers utilized these particles for the detection of various aldehydes at trace levels in the parts per billion (ppb) range. Of particular interest to the authors was the detection of 4-ethylbenzaldehyde, as elevated levels of this compound are indicative of early stages of lung cancer. To enable the detection of 4-ethylbenzaldehyde, a Raman-active compound called p-aminophenylthiophenol (4-ATP) was pre-adsorbed onto the GSP@ZIF-8 particles. This facilitated a chemical bond between the amino (-NH₂) group of 4-ATP and the aldehyde (-CHO) group of 4-ethylbenzaldehyde. The resulting C = N stretching peak at 1623 cm^{-1} was then detected using surface-enhanced Raman spectroscopy (SERS). By employing this technique, it was possible to measure the concentration of 4-ethylbenzaldehyde down to the ppb level, enabling the early diagnosis of lung cancer. This approach highlights the potential of combining core-shell particles and SERS for the sensitive detection of biomarkers associated with various diseases, including lung cancer.

In a further study, Jiang et al. developed a novel approach for measuring dopamine (DA) levels in urine by embedding silver nanoparticles on the surface of MIL-101(Fe).^[168] The detection method relied on surface-enhanced Raman spectroscopy and the modulation of the SERS signal of 2,2'-azino-bis(3-ethylbenzthiazoline 6-sulfonic acid) diammonium salt (ABTS) in the presence of dopamine and hydrogen peroxide (H₂O₂). Initially, the researchers measured the SERS signal of ABTS alone and ABTS in the presence of H₂O₂. In the presence of H₂O₂, ABTS is oxidized to ABTS²⁺, resulting in a significant enhancement of the SERS signal. However, when dopamine is also added to the system, it suppresses the oxidation of ABTS by H₂O₂, leading to a weakening of the SERS signal. Jiang et al. observed a strong linear correlation between the concentration of dopamine and the weakening of the ABTS SERS signal. They achieved a wide linear range of detection from 1.054 pM to 210.8 nM concentrations of dopamine, with a low detection limit of 0.32 pM in aqueous solutions. The method demonstrated good reproducibility when applied to real urine samples, enabling the measurement of dopamine levels in the range of 100 pM to 500 pM. This technique holds promise for future applications in clinical diagnostics and monitoring dopamine-related disorders.

Another example, where sensing biomarkers can save a life, is heart failure. In many cases, this is a life-threatening syndrome that globally affects more than 64 million people.^[185] Early diagnosis of heart failure is crucial for effective management and treatment. One approach to detecting heart failure involves sensing the biomarker N-terminal pro-brain natriuretic peptide (NT-proBNP), which can indicate the presence of the condition. In a study by He et al., a sensitive sensor for NT-proBNP was developed using a MOF sandwich configuration (Figure 44). The sensor involved the formation of two complexes consisting 1) of IRMOF-3, gold tetrapods (AuTP), toluidine blue (TB) and an anti-NT-proBNP antibody (IRMOF-3@AuTPs@TB@Ab2) and

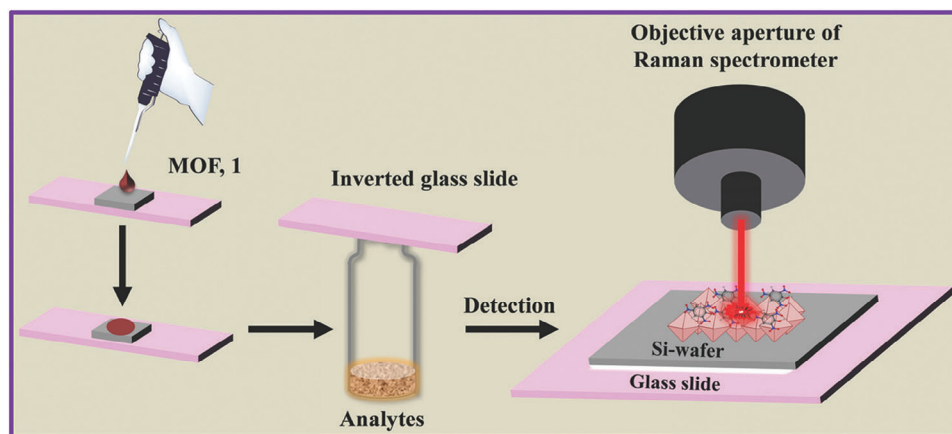


Figure 41. Detection of nitro compounds by Raman spectroscopy. Schematic showing the detection of nitro analytes by exposing the MOF film to the analyte vapors resulting in the suppression of Stokes shift peak intensities. Reproduced with permission.^[167] Copyright 2019, The Royal Society of Chemistry.

2) of magnetic CoFe₂O₄ NP; a gold NP (AuNP) and the antibody (CoFe₂O₄@AuNPs@Ab1). With this sandwich configuration, they were able to measure NT-proBNP with good linearity and reproducibility with concentrations ranging from 1 fg mL⁻¹ to 1 ng mL⁻¹.^[158b]

5.6. Food Safety and Environmental Studies

The rapid growth of industries worldwide has resulted in a significant rise in environmental pollution. Unfortunately, certain pollutants, such as pesticides and excessive fertilizer use, are intentionally released into nature. Moreover, various chemicals employed to preserve food or enhance its taste and color can be toxic when consumed in high doses. Consequently, there is a pressing need for highly sensitive sensors capable of detecting toxins and pollutants present in the environment and food supply, aiming to safeguard the health of both humans and animals. To address this

challenge, numerous research groups started to develop MOF-assisted SERS sensors specifically designed for the detection of harmful molecules. These innovative sensors offer promising solutions to accurately identify and quantify a wide range of hazardous substances, contributing to the preservation of human and environmental well-being. By leveraging the unique properties of MOFs in conjunction with the enhanced signal sensitivity provided by SERS, these sensors represent a significant advancement in the field of chemical detection, paving the way for improved monitoring and control of toxins and pollutants in various applications.

Hu et al. conducted a study in which they synthesized gold nanoparticle-embedded MIL-101 to detect p-phenylenediamine (PPD), a toxic compound commonly found in hair dyes and semi-permanent tattoos (Figure 45).^[62c] The Scientific Committee on Consumer Products (SCCP) determined a NOAEL (No Observed Adverse Effect Level) of 5 mg kg⁻¹ for rats.^[186] Before utilizing the AuNPs/MIL-101 nanocomposites for PPD

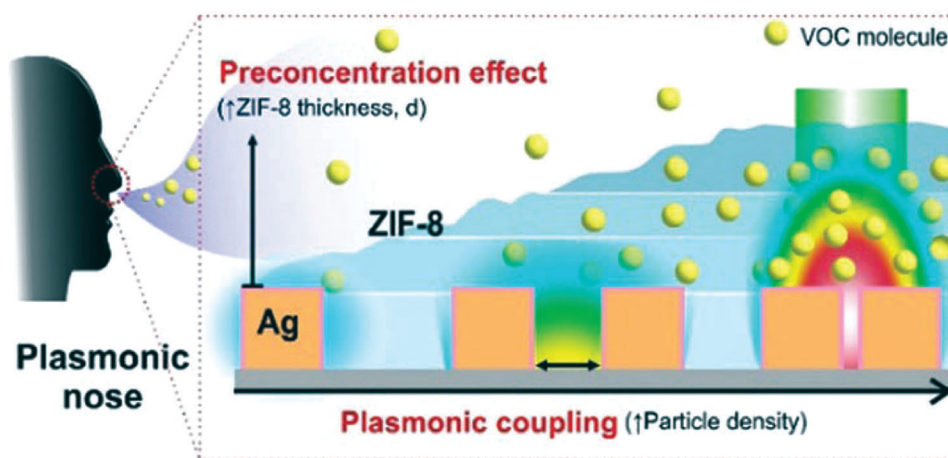


Figure 42. Plasmonic nose concept. The schematic shows three different arrangements of Ag nanocubes embedded in ZIF-8 and the corresponding field strengths around the cubes for detecting volatile organic compounds (VOC) vapor. The light blue horizontal strips indicate different heights of the ZIF-8 layer. Reproduced with permission.^[100] Copyright 2018, The Royal Society of Chemistry.

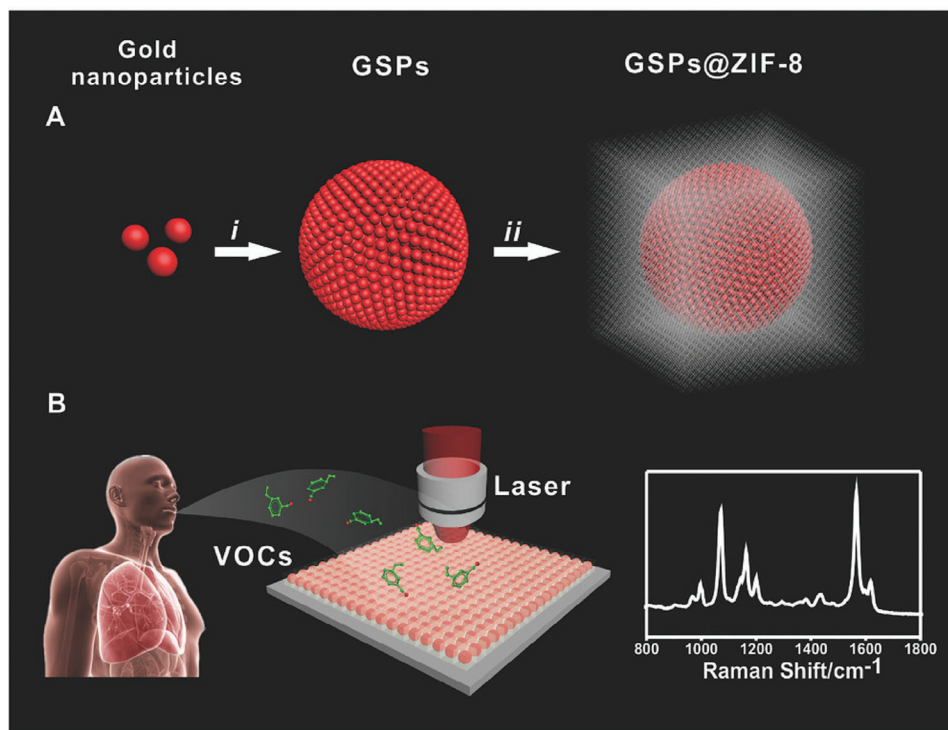


Figure 43. Sketch of Volatile organic compound (VOC) detection via GSP@ZIF-8 core-shell structure. A) Diagrammatic sketch of synthesizing GSP@ZIF-8 core-shell structure: i) gold nanoparticles assembled into GSPs, ii) ZIF-8 shell coated on GSP surface. B) Volatile organic compound (VOC) detection via SERS spectroscopy. Reproduced with permission.^[29f] Copyright 2018, Wiley-VCH.

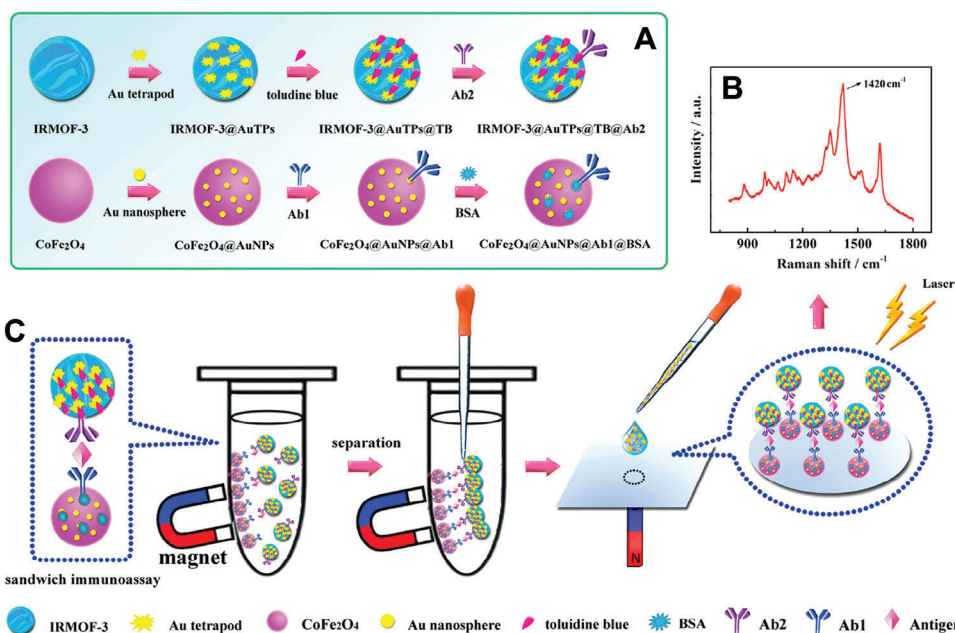


Figure 44. Schematic Diagram of the SERS-Based Immunosensor for the Detection of NT-proBNP. A) Preparation of MOF-3@AuTPs@TB@Ab₂ (top) and CoFe₂O₄@AuNPs@Ab₁ (bottom) B) SERS spectrum of NT-proBNP measured with the sandwich structure formed with both complexes MOF-3@AuTPs@TB@Ab₂ and CoFe₂O₄@AuNPs@Ab₁. C) Formation of a MOF-3@AuTPs@TB@Ab₂/Antigen/CoFe₂O₄@AuNPs@Ab₁ Sandwich structure, via magnetic separation based on the magnetic properties of CoFe₂O₄@AuNPs@Ab₁. The final measurement consists of a 10 μ l droplet on a silica wafer using a magnet to concentrate the structures on the surface. Adapted with permission.^[158b] Copyright 2016, American Chemical Society.

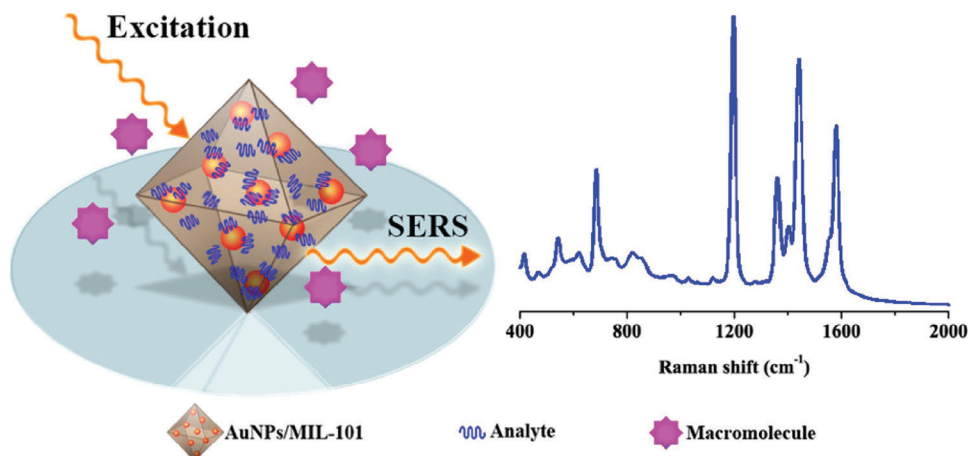


Figure 45. Sensing of p-phenylenediamine by SERS. (Left) Sketch of embedded Au NPs in MIL-101 and the adsorbed analyte in MIL-101. (Right) An exemplary SERS spectrum of an analyte. Reproduced with permission.^[62c] Copyright 2014, American Chemical Society.

detection, the researchers investigated the penetration of analytes into the MOF framework to ensure the proximity to the gold particles required for SERS enhancement. To accomplish this, they compared the SERS signals of 4,4'-bipyridine and poly 4-vinylpyridine within the nanocomposites. The SERS signal of 4,4'-bipyridine increased over time, indicating the adsorption of more molecules within the framework. However, for the larger poly 4-vinylpyridine molecules, no SERS signal was observed, suggesting that they did not penetrate the framework and, thus, did not reach the required proximity for SERS enhancement. Subsequently, Yuling et al. successfully measured PPD concentrations ranging from 1.0 to 100.0 ng mL⁻¹ in laboratory conditions using the AuNPs/MIL-101 nanocomposites, achieving high correlation coefficients of 0.9950. The lowest detectable concentration was as low as 0.1 ng mL⁻¹. Moreover, they applied the AuNPs/MIL-101 nanocomposites to analyze river and sewage water samples for PPD content. In the sewage water sample, a concentration of 1.3 ng mL⁻¹ of PPD was detected, while no PPD was found in the river water sample. These findings demonstrate the potential of the AuNPs/MIL-101 nanocomposites as effective and sensitive tools for the detection of PPD in various environmental samples.

Cai et al. employed a combination of gold nanoparticles (AuNPs) and MIL-101, where the AuNPs were encapsulated within a MIL-100 shell, resulting in Au@MIL-101 core-shell nanoparticles. The synthesis of these nanoparticles involved a layer-by-layer assembly process. By utilizing this approach, the researchers successfully detected methenamine, achieving a remarkable correlation coefficient of 0.9998 within a concentration range of 1.0×10^{-8} M (1.4 ng mL⁻¹) to 1.0×10^{-6} M (140 ng mL⁻¹) under laboratory conditions. The lowest detectable concentration reached an impressive level of 5×10^{-10} M (0.07 ng mL⁻¹). Furthermore, Cai et al. investigated the detection of methenamine in a real-world sample by spiking it into vermicelli (pasta). In this scenario, the lowest detected concentration was 1.0×10^{-9} M (0.14 ng mL⁻¹).^[101c] According to the Scientific Committee on Health and Environmental Risks, methenamine intake of up to 4000 mg per day does not pose health risks.^[187] This value corresponds to $\approx 2.9 \times 10^{-3}$ mol of methenamine, which is several

orders of magnitude higher than the detection limit achieved in the real-world vermicelli sample.

Wu et al. addressed the concern of harmful food dyes by developing a method to detect New Coccine (NC) and orange II (OII) using surface-enhanced Raman spectroscopy (SERS) in conjunction with UiO-66-NH₂ decorated with gold nanoparticles on the surface for signal enhancement.^[99] The detection of these dyes was initially tested under laboratory conditions, where Wu et al. successfully detected NC and OII in the concentration range of 0.1 mg L⁻¹ to 1.0 mg L⁻¹, demonstrating excellent linearity. These findings were further validated in real-world examples, such as a soft drink and paprika. The detection of both NC and OII is of utmost importance due to their potential health risks. OII has been banned from food usage in most parts of the world, highlighting the urgency of reliable detection methods. Furthermore, the acceptable daily intake of NC has been estimated to be only 0.7 mg kg⁻¹ by the European Food Safety Authority.^[188]

6. Conclusion and Outlook

Metal-organic frameworks (MOFs) have emerged as a transformative class of materials with immense importance on the technical and scientific landscape, unlocking new avenues in energy, environment, catalysis, electronics, and healthcare. Given the wide palette of their applications, host-guest interactions as well as chemical compositions, structural diversity, designability, and stability, it is of utmost importance to get in-depth insights into MOFs at the molecular level. Reactions like nucleation, adsorption, or catalysis require analytical tools, that feature structural sensitivity and in situ and in operando capabilities at the same time.

In this contribution, we introduced the large pool of Raman technologies currently available to study materials and explained the physical principle of Raman scattering, the underlying physics behind strategies to enhance the Raman signal, as well as the instrumentations and developed measurement modalities for probing MOFs in various applications. Raman spectroscopy can provide information on different length scales starting at the atomic level from the framework, to averaged

crystals on the micrometer scale, up to MOF layers with millimeter to centimeter sizes. Equally, Raman scattering can monitor the temporal evolution of MOFs during reactions. It can probe chemical processes like charge transfer reactions or bond formation, starting at the fs-ps regime using transient spectroscopy, over to intermediates with ns- μ s resolution using pump-probe or time-gated approaches, up to catalytical processes on the ms region upward using emCCD camera based state-of-the-art Raman systems.

Consecutively, properties in MOFs that can be investigated by Raman spectroscopy are vast, starting from structural dynamics and states of MOFs, including their morphology, the framework composition, crystal symmetry, coordination, density, functionalization, presence of guests, and defects. Raman spectroscopy allows for probing reactions of the framework upon external triggers like light illumination, and interactions with guest molecules in liquid and gas phase. Here, Raman spectroscopy can help identify analytes and intermediates, localize and investigate site-specific binding, and assess the sorption process mechanistically but also thermodynamically. Since Raman spectroscopy can study MOFs in their pristine form, as well as in situ or under different environmental conditions, such as varying temperature or pressure, it allows to monitor structural changes, guest molecule interactions, and phase transitions in MOFs, contributing to a deeper understanding of their dynamic behavior.

Lastly, we discussed recent examples where Raman spectroscopy addresses societal challenges in the fields of environmental remediation, healthcare, and energy storage. In the field of gas storage and separation, MOFs have revolutionized energy storage and delivery by providing efficient solutions for capturing and storing gases such as ammonia. Their high porosity and tailored pore sizes enable the design of MOFs with exceptional adsorption capacities relevant for sustainable energy but also environmental applications, such as air remediation and atmospheric water harvesting. On the other hand, MOFs made a profound impact in catalysis and chemical sensing. The ability to incorporate different metal nodes and organic ligands, but also the functionalization of MOFs with SERS substrates, for example, allowed the precise engineering of materials with active sites for unprecedented sensitivity down to the single-molecule level in a label-free manner. This has led to breakthroughs in catalytic processes or the field of healthcare as a platform for targeted and controlled drug delivery and drug-sensing.

As the field of MOFs constantly continues to grow, Raman spectroscopy will remain a vital technique in unraveling the complexity and the full potential of these versatile materials. Given the wide applicability of MOFs, the big question is, what might be future perspectives? We believe the future of Raman spectroscopy in the field of metal-organic framework materials is bright. Besides its applicability to MOFs, Raman spectroscopy is an eminent technique for the characterization of 2D and van der Waals materials, such as graphene or boron nitride.^[189] Besides advanced material identification, Raman scattering allows for evaluating these materials concerning the number of monolayers, defects, inter-layer modes, phonon modes, strain, or conductivities, to name some properties. Composite materials based on graphene/MOF- or BN/MOF-hybrid structures hold great promise for applications in the

field of environmental and energy technologies, such as batteries, supercapacitors, or catalysts.^[190] Here, hybrid materials might eliminate the instability problems of MOFs under harsh and humid conditions by serving as all-solid-state supercapacitors.^[191] Layer-by-layer MOF/graphene composites are tunable and could serve as anodes in batteries,^[190a,192] but also as advanced filter systems in environmental research by acting as molecular sieves, as well as by picking up toxic substances from air or water.^[190a,193] A further combination of 2D materials with MOFs could be in the field of surface passivation with anti-microbial properties^[194] or even as an anti-fouling coating.^[195] At the nanoscale, mixing MOF-nanoparticles with 2D materials and even polymers,^[196] could yield new polymeric compound materials with new thermal and elastic properties. 3D-printed graphene-based materials could act as strain sensors.^[197]

Lately, new correlative approaches have been published, combining Raman spectroscopy with a wealth of different techniques including AFM, X-ray, SEM, and SEM-EDX.^[198] They provide higher spatial resolution in 2D and 3D down to the crystal structures combined with chemical information of guest molecules due to the vibrational contrast of Raman spectroscopy. While correlative imaging systems continue to advance, we anticipate that Raman spectroscopy will take a second trajectory, becoming more portable, cost-effective, and sensitive. We envision a future where 3D-printed instruments enable field operations through small and mobile handheld devices. Leveraging MOF-based sensor chips, these analytical instruments could be deployed directly to the sight of contamination, such as after accidents or explosions, as well as for routine checks in security-critical areas like airports. In addition to technical advancements, the field is also witnessing the emergence of innovative data analysis methods, including deep learning and neural networks.^[199] This enables real-time analysis of potentially unknown compounds on the fly.^[200] In laboratories, these advancements in data analysis will facilitate the synthesis of dedicated MOF systems on-demand and the analysis of large sets of sensing data in a significantly shorter time. This, in turn, will allow for the on-the-fly analysis of analytes using SERS assays in clinical environments, as well as in the monitoring of food, water, and air quality control. The rising implementation and application of Raman techniques and their combinations will provide advanced characterization methods and provide further insight into the molecular working principle of metal-organic frameworks and composite materials in the future.

Acknowledgements

J.T. and F.K. contributed equally to this work. Funding by the Center for NanoScience Munich (CeNS), the Center for Integrated Protein Science Munich (CiPSM), Nanosystems Initiative Munich (NIM), the Deutsche Forschungsgemeinschaft (PL 696/4-1; Project-ID 201269156-SFB1032, B03) was gratefully acknowledged. The authors thank Don C. Lamb for his support and access to laboratory facilities.

Open access funding enabled and organized by Projekt DEAL.

Conflict of Interest

The authors declare no conflict of interest.

Keywords

advanced light microscopy, in-situ characterization, metal-organic frameworks, raman scattering, spectroscopy

Received: July 2, 2023

Revised: September 23, 2023

Published online:

- [1] O Yaghi, M. O'Keeffe, N. Ockwig, H. Chae, M. Eddaoudi, J. Kim, *Nature* **2003**, 423, 705.
- [2] a) P. Moghadam, A. Li, S. Wiggin, A. Tao, A. Maloney, P. Wood, S. Ward, D. Fairen-Jimenez, *Chem. Mater.* **2017**, 29, 2618; b) P. Moghadam, A. Li, X. Liu, R. Bueno-Perez, S. Wang, S. Wiggin, P. Wood, D. Fairen-Jimenez, *Chem. Sci.* **2020**, 11, 8373.
- [3] S. Moosavi, A. Nandy, K. Jablonka, D. Ongari, J. Janet, P. Boyd, Y. Lee, B. Smit, H. Kulik, *Nat. Commun.* **2020**, 11, 4068.
- [4] a) W. Fan, X. Zhang, Z. Kang, X. Liu, D. Sun, *Coord. Chem. Rev.* **2021**, 443, 213968; b) H. Li, L. Li, R. Lin, W. Zhou, Z. Zhang, S. Xiang, B. Chen, *Energy Chem* **2019**, 1, 100006; c) J. Mason, M. Veenstra, J. Long, *Chem. Sci.* **2014**, 5, 32; d) S. Hiraide, Y. Sakanaka, H. Kajiro, S. Kawaguchi, M. Miyahara, H. Tanaka, *Nat. Commun.* **2020**, 11, 3867; e) G. Chen, Y. He, Y. Yu, H. Lv, S. Li, F. Wang, Z. Gu, J. Zhang, *Angew. Chem., Int. Ed.* **2023**, 62, e202300726.
- [5] S. Rojas, P. Horcajada, *Chem. Rev.* **2020**, 120, 8378.
- [6] a) H. Furukawa, F. Gándara, Y. Zhang, J. Jiang, W. Queen, M. Hudson, O. Yaghi, *J. Am. Chem. Soc.* **2014**, 136, 4369; b) T. Matemb Ma Ntep, M. Wahiduzzaman, E. Laurenz, I. Cornu, G. Mouchaham, I. Dovgaliuk, S. Nandi, K. Knop, C. Jansen, F. Nouar, P. Florian, G. Földner, G. Maurin, C. Janiak, C. Serre, *Adv. Mater.* **2023**, 2211302; c) A. Bezrukov, D. O'hearn, V. Gascón-Pérez, S. Darwish, A. Kumar, S. Sanda, N. Kumar, K. Francis, M. Zaworotko, *Cell Rep. Phys. Sci.* **2023**, 4, 101252.
- [7] a) J. Calbo, M. Golomb, A. Walsh, *J. Mater. Chem. A* **2019**, 7, 16571; b) S. Chuhadiya, Himanshu, D. Suthar, S. Patel, M. Dhaka, *Coord. Chem. Rev.* **2021**, 446, 214115.
- [8] a) S. Rogge, A. Bavykina, J. Hajek, H. Garcia, A. Olivos-Suarez, A. Sepúlveda-Escribano, A. Vimont, G. Clet, P. Bazin, F. Kapteijn, M. Daturi, E. Ramos-Fernandez, F. Llabrés I Xamena, V. Van Speybroeck, J. Gascon, *Chem. Soc. Rev.* **2017**, 46, 3134; b) V. Pascanu, G. González Miera, A. K Inge, B. Martín-Matute, *J. Am. Chem. Soc.* **2019**, 141, 7223; c) W. Zhan, H. Gao, Y. Yang, X. Li, Q. Zhu, *ACS Sustainable Chem. Eng.* **2022**, 3, 2200004; d) Y. Sun, D. Lu, Y. Sun, M. Gao, N. Zheng, C. Gu, F. Wang, J. Zhang, *ACS Mater. Lett.* **2021**, 3, 64.
- [9] a) M. Campbell, M. Dinca, *Sensors* **2017**, 17, 1108; b) A. Ejsmont, J. Andreo, A. Lanza, A. Galarda, L. Macreadie, S. Wuttke, S. Canossa, E. Ploetz, J. Goscianska, *Coord. Chem. Rev.* **2021**, 430, 213655; c) H. Li, Y. Pan, Q. Li, Q. Lin, D. Lin, F. Wang, G. Xu, J. Zhang, *J. Mater. Chem. A* **2023**, 11, 965; d) X. Wang, P. Lan, S. Ma, *ACS Cent. Sci.* **2020**, 6, 1497.
- [10] M. Allendorf, R. Dong, X. Feng, S. Kaskel, D. Matoga, V. Stavila, *Chem. Rev.* **2020**, 120, 8581.
- [11] a) J. Wang, I. Imaz, D. Maspoch, *Small Struct.* **2022**, 3, 2100126; b) J. Andreo, R. Ettlinger, O. Zaremba, Q. Peña, U. Lächelt, R. De Luis, R. Freund, S. Canossa, E. Ploetz, W. Zhu, C. Diercks, H. Gröger, S. Wuttke, *J. Am. Chem. Soc.* **2022**, 144, 7531.
- [12] a) M. Ding, W. Liu, R. Gref, *Adv. Drug Delivery Rev.* **2022**, 190, 114496; b) M. Giménez-Marqués, T. Hidalgo, C. Serre, P. Horcajada, *Coord. Chem. Rev.* **2016**, 307, 342; c) R. Ettlinger, U. Lächelt, R. Gref, P. Horcajada, T. Lammers, C. Serre, P. Couvreur, R. Morris, S. Wuttke, *Chem. Soc. Rev.* **2022**, 51, 464; d) J. Guo, Y. Yu, W. Zhu, R. Serda, S. Franco, L. Wang, Q. Lei, J. Agola, A. Nouredine, E. Ploetz, S. Wuttke, C. Brinker, *Adv. Funct. Mater.* **2021**, 31, 2005935.
- [13] a) P. Horcajada, C. Serre, G. Maurin, N. Ramsahye, F. Balas, M. Vallet-Regí, M. Sebban, F. Taulelle, G. Férey, *J. Am. Chem. Soc.* **2008**, 130, 6774; b) H. Bunzen, *ChemNanoMat* **2021**, 7, 998; c) S. Rojas, A. Arenas-Vivo, P. Horcajada, *Coord. Chem. Rev.* **2019**, 388, 202; d) E. Ploetz, H. Engelke, U. Lächelt, S. Wuttke, *Adv. Funct. Mater.* **2020**, 30, 1909062; e) C. Sun, C. Qin, X. Wang, G. Yang, K. Shao, Y. Lan, Z. Su, P. Huang, C. Wang, E. Wang, *Dalton Trans.* **2012**, 41, 6906.
- [14] a) Y. Cui, Y. Yue, G. Qian, B. Chen, *Chem. Rev.* **2012**, 112, 1126; b) S. Miller, M. Teplensky, P. Moghadam, D. Fairen-Jimenez, *Interface Focus* **2016**, 6, 20160027; c) M. Gutiérrez, Y. Zhang, J. Tan, *Chem. Rev.* **2022**, 122, 10438; d) É. Whelan, F. Steuber, T. Gunnlaugsson, W. Schmitt, *Coord. Chem. Rev.* **2021**, 437, 213757; e) Y. Tang, H. Wu, W. Cao, Y. Cui, G. Qian, *Adv. Opt. Mater.* **2021**, 9, 2001817; f) Y. Hasegawa, Y. Kitagawa, *J. Mater. Chem. C* **2019**, 7, 7494; g) H. Kaur, S. Sundriyal, V. Pachauri, S. Ingebrandt, K. Kim, A. Sharma, A. Deep, *Coord. Chem. Rev.* **2019**, 401, 213077; h) R. Haldar, L. Heinke, C. Wöll, *Adv. Mater.* **2020**, 32, 1905227; i) P. Scheurle, A. Biewald, A. Mähringer, A. Hartschuh, D. Medina, T. Bein, *Small Structures* **2022**, 3, 2100195.
- [15] a) L. Sun, M. Campbell, M. Dinca, *Angew. Chem., Int. Ed.* **2016**, 55, 3566; b) M. Sadakiyo, T. Yamada, H. Kitagawa, *ChemPlusChem* **2016**, 81, 691; c) A. Li, Q. Gao, J. Xu, X. Bu, *Coord. Chem. Rev.* **2017**, 344, 54; d) L. Guo, J. Sun, J. Wei, Y. Liu, L. Hou, C. Yuan, *Carbon Energy* **2020**, 2, 203; e) L. Xie, G. Skorupskii, M. Dinca, *Chem. Rev.* **2020**, 120, 8536; f) D. Lim, H. Kitagawa, *Chem. Soc. Rev.* **2021**, 50, 6349.
- [16] a) S. Nadar, V. Rathod, *Int. J. Biol. Macromol.* **2018**, 120, 2293; b) P. Saines, N. Bristowe, *Dalton Trans.* **2018**, 47, 13257; c) M. Peller, K. Böll, A. Zimpel, S. Wuttke, *Inorg. Chem. Front.* **2018**, 5, 1760; d) B. Meteku, J. Huang, J. Zeng, F. Subhan, F. Feng, Y. Zhang, Z. Qiu, S. Aslam, G. Li, Z. Yan, *Coord. Chem. Rev.* **2020**, 413, 213261; e) V. Rubio-Giménez, S. Tatay, C. Martí-Gastaldo, *Chem. Soc. Rev.* **2020**, 49, 5601.
- [17] a) S. Castellanos, F. Kapteijn, J. Gascon, *CrystEngComm* **2016**, 18, 4006; b) A. Kanj, K. Müller, L. Heinke, *Macromol. Rapid Commun.* **2018**, 39, 1700239; c) A. Rice, C. Martin, V. Galitskiy, A. Berseneva, G. Leith, N. Shustova, *Chem. Rev.* **2020**, 120, 8790.
- [18] C. Liu, H. Nguyen, O. Yaghi, *AsiaChem Mag.* **2020**, 1, 18.
- [19] T. Islamoglu, K. Otake, P. Li, C. Buru, A. Peters, I. Akpinar, S. Garibay, O. Farha, *CrystEngComm* **2018**, 20, 5913.
- [20] S. Kitagawa, M. Kondo, *Bull. Chem. Soc. Jpn.* **1998**, 71, 1739.
- [21] a) Y. Li, Y. Wang, W. Fan, D. Sun, *Dalton Trans.* **2022**, 51, 4608; b) P. Zhao, S. Tsang, D. Fairen-Jimenez, *Cell Rep. Phys. Sci.* **2021**, 2, 100544; c) N. Behera, J. Duan, W. Jin, S. Kitagawa, *EnergyChem* **2021**, 3, 100067; d) T. Bennett, A. Cheetham, A. Fuchs, F. Coudert, *Nat. Chem.* **2017**, 9, 11; e) A. Schneemann, V. Bon, I. Schwedler, I. Senkovska, S. Kaskel, R. Fischer, *Chem. Soc. Rev.* **2014**, 43, 6062; f) G. Férey, C. Serre, *Chem. Soc. Rev.* **2009**, 38, 1380.
- [22] a) S. Yuan, L. Feng, K. Wang, J. Pang, M. Bosch, C. Lollar, Y. Sun, J. Qin, X. Yang, P. Zhang, Qi Wang, L. Zou, Y. Zhang, L. Zhang, Yu Fang, J. Li, H. Zhou, *Adv. Mater.* **2018**, 30, 1704303; b) O. Yaghi, M. Kalmutzki, C. Diercks, *Introduction to Reticular Chemistry: Metal-Organic Frameworks and Covalent Organic Frameworks*, Wiley-VCH Verlag GmbH & Co. KGaA, Weinheim **2019**.
- [23] a) Y. Bai, Y. Dou, L. Xie, W. Rutledge, J. Li, H. Zhou, *Chem. Soc. Rev.* **2016**, 45, 2327; b) V. Bon, V. Senkovskyy, I. Senkovska, S. Kaskel, *Chem. Commun.* **2012**, 48, 8407; c) I. Romero-Muñiz, C. Romero-Muñiz, I. Del Castillo-Velilla, C. Marini, S. Calero, F. Zamora, A. Platero-Prats, *ACS Appl. Mater. Interfaces* **2022**, 14, 27040; d) U. Schubert, *Coord. Chem. Rev.* **2022**, 469, 214686; e) V. Bon, I. Senkovska, I. Baburin, S. Kaskel, *Cryst. Growth Des.* **2013**, 13, 1231; f) C. Koschnick, M. Terban, S. Canossa, M. Etter, R. Dinnebier, B. Lotsch, *Adv. Mater.* **2023**, 2210613.

- [24] a) V. Butova, A. Budnyk, K. Charykov, K. Veltitsyna-Novikova, C. Lamberti, A. Soldatov, *Chem. Commun.* **2019**, 55, 901; b) F. Drache, V. Bon, I. Senkovska, J. Getzschmann, S. Kaskel, *Philos. Trans. R. Soc. A* **2017**, 375, 20160027; c) P. Verma, L. Huelsenbeck, A. Nichols, T. Islamoglu, H. Heinrich, C. Machan, G. Giri, *Chem. Mater.* **2020**, 32, 10556.
- [25] a) S. Canossa, Z. Ji, C. Gropp, Z. Rong, E. Ploetz, S. Wuttke, O. Yaghi, *Nat. Rev. Mater.* **2023**, 8, 331; b) S. Jeong, J. Seong, S. Moon, J. Lim, S. Baek, S. Min, M. Lah, *Nat. Commun.* **2022**, 13, 1027; c) Z. Ji, T. Li, O. Yaghi, *Science* **2020**, 369, 674.
- [26] a) J. Cavka, S. Jakobsen, U. Olsbye, N. Guillou, C. Lamberti, S. Bordiga, K. Lillerud, *J. Am. Chem. Soc.* **2008**, 130, 13850; b) Z. Chang, D. Yang, J. Xu, T. Hu, X. Bu, *Adv. Mater.* **2015**, 27, 5432; c) F. Couderc, *Chem. Mater.* **2015**, 27, 1905; d) G. Férey, C. Mellot-Draznieks, C. Serre, F. Millange, J. Dutour, S. Surblé, I. Margiolaki, *Science* **2005**, 309, 2040; e) G. Férey, C. Serre, C. Mellot-Draznieks, F. Millange, S. Surblé, J. Dutour, I. Margiolaki, *Angew. Chem., Int. Ed.* **2004**, 43, 6296; f) C. Fernandez, P. Martin, T. Schaefer, M. Bowden, P. Thallapally, L. Dang, W. Xu, X. Chen, B. Mcgrail, *Sci. Rep.* **2014**, 4, 6114; g) P. Freund, L. Mielewczyk, M. Rauche, I. Senkovska, S. Ehrling, E. Brunner, S. Kaskel, *ACS Sustain. Chem.* **2019**, 7, 4012; h) P. Freund, I. Senkovska, S. Kaskel, *ACS Appl. Mater. Interfaces* **2017**, 9, 43782; i) S. Horike, S. Shimomura, S. Kitagawa, *Nat. Chem.* **2009**, 1, 695; j) T. Kundu, M. Wahiduzzaman, B. Shah, G. Maurin, D. Zhao, *Angew. Chem. Int. Ed.* **2019**, 58, 8073; k) J. Mason, J. Oktawiec, M. Taylor, M. Hudson, J. Rodriguez, J. Bachman, M. Gonzalez, A. Cervellino, A. Guagliardi, C. Brown, P. Llewellyn, N. Masciocchi, J. Long, *Nature* **2015**, 527, 357; l) S. Rojas, N. Guillou, P. Horcajada, *ACS Appl. Mater. Interfaces* **2019**, 11, 22188; m) H. Sato, W. Kosaka, R. Matsuda, A. Hori, Y. Hijikata, R. Belosludov, S. Sakaki, M. Takata, S. Kitagawa, *Science* **2014**, 343, 167; n) C. Serre, F. Millange, C. Thouvenot, M. Nogués, G. Marsolier, D. Louër, G. Férey, *J. Am. Chem. Soc.* **2002**, 124, 13519; o) F. Walenszus, J. Evans, V. Bon, F. Schwotzer, I. Senkovska, S. Kaskel, *Chem. Mater.* **2021**, 33, 7964.
- [27] a) E. Brunner, M. Rauche, *Chem. Sci.* **2020**, 11, 4297; b) H. Dyson, P. Wright, *Curr. Opin. Struct. Biol.* **2021**, 70, 44; c) T. Easun, F. Moreau, Y. Yan, S. Yang, M. Schröder, *Chem. Soc. Rev.* **2017**, 46, 239; d) G. Foran, N. Verdier, D. Lepage, C. Malveau, N. Dupré, M. Dollé, *Polymers* **2021**, 13, 1207; e) J. Fraissard, T. Ito, *Zeolites* **1988**, 8, 350; f) Y. Fu, H. Guan, J. Yin, X. Kong, *Coord. Chem. Rev.* **2021**, 427, 213563; g) M. Ge, T. Yang, H. Xu, X. Zou, Z. Huang, *J. Am. Chem. Soc.* **2022**, 144, 15165; h) C. Horton-Garcia, G. Pavlovskaya, T. Meersmann, *J. Am. Chem. Soc.* **2005**, 127, 1958; i) C. Jameson, A. Jameson, R. Gerald, H. Lim, *J. Phys. Chem. B* **1997**, 101, 8418; j) J. Jayapaul, S. Komulainen, V. Zhivonitko, J. Mares, C. Giri, K. Rissanen, P. Lantto, V. Telkki, L. Schröder, *Nat. Commun.* **2022**, 13, 1708; k) F. Kolbe, S. Krause, V. Bon, I. Senkovska, S. Kaskel, E. Brunner, *Chem. Mater.* **2019**, 31, 6193; l) S. Krause, F. Reuter, S. Ehrling, V. Bon, I. Senkovska, S. Kaskel, E. Brunner, *Chem. Mater.* **2020**, 32, 4641; m) J. Li, S. Li, A. Zheng, X. Liu, N. Yu, F. Deng, *J. Phys. Chem. C* **2017**, 121, 14261; n) R. Main, S. Vornholt, C. Rice, C. Elliott, S. Russell, P. Kerr, M. Warren, R. Morris, *Commun. Chem.* **2023**, 6, 44; o) M. Mazaj, V. Kaucic, N. Zabukovec Logar, *Acta Chim. Slov.* **2016**, 63, 440; p) M. Oschatz, H. Hoffmann, J. Pallmann, J. Schaber, L. Borchardt, W. Nickel, I. Senkovska, S. Rico-Francés, J. Silvestre-Albero, S. Kaskel, E. Brunner, *Chem. Mater.* **2014**, 26, 3280; q) S. Rehman, S. Xu, H. Xu, T. Tao, Y. Li, Z. Yu, K. Ma, W. Xu, J. Wang, *Mater. Today Adv.* **2022**, 16, 100287; r) L. Samperisi, A. Jaworski, G. Kaur, K. Lillerud, X. Zou, Z. Huang, *J. Am. Chem. Soc.* **2021**, 143, 17947; s) J. Schaber, S. Krause, S. Paasch, I. Senkovska, V. Bon, D. Töbrens, D. Wallacher, S. Kaskel, E. Brunner, *J. Phys. Chem. C* **2017**, 121, 5195; t) S. Smeets, L. Mccusker, C. Baerlocher, S. Elomari, D. Xie, S. Zones, *J. Am. Chem. Soc.* **2016**, 138, 7099; u) J. Weber, J. Schmidt, A. Thomas, W. Böhlmann, *Langmuir* **2010**, 26, 15650; v) V. Witherspoon, J. Xu, J. Reimer, *Chem. Rev.* **2018**, 118, 10033; w) Y. Xiao, S. Li, J. Xu, F. Deng, *Curr. Opin. Colloid Interface Sci.* **2022**, 61, 101633; x) A. Yakovenko, Z. Wei, M. Wriedt, J. Li, G. Halder, H. Zhou, *Cryst. Growth Des.* **2014**, 14, 5397.
- [28] a) J. Wang, J. Yin, O. Shekha, O. Bakr, M. Eddaoudi, O. Mohammed, *ACS Appl. Mater. Interfaces* **2022**, 14, 9970; b) T. Wu, X. Gao, F. Ge, H. Zheng, *CrystEngComm* **2022**, 24, 7881.
- [29] a) B. Weckhuysen, *Angew. Chem. Int. Ed.* **2009**, 48, 4910; b) E. Stavitski, B. Weckhuysen, *Chem. Soc. Rev.* **2010**, 39, 4615; c) K. Hadjiivanov, D. Panayotov, M. Mihaylov, E. Ivanova, K. Chakarova, S. Andonova, N. Drenchev, *Chem. Rev.* **2021**, 121, 1286; d) S. Bordiga, C. Lamberti, F. Bonino, A. Traversi, F. Thibault-Starzyk, *Chem. Soc. Rev.* **2015**, 44, 7262; e) J. Sunil, C. Narayana, G. Kumari, K. Jayaramulu, *Chem. Soc. Rev.* **2023**, 52, 3397; f) X. Qiao, B. Su, C. Liu, Q. Song, D. Luo, G. Mo, T. Wang, *Adv. Mater.* **2018**, 30, 1702275; g) A. Vimont, F. Thibault-Starzyk, M. Daturi, *Chem. Soc. Rev.* **2010**, 39, 4928; h) L. Hanna, J. Lockard, *J. Phys. Condens. Matter* **2019**, 31, 483001.
- [30] a) M. Daturi, *Curr. Phys. Chem.* **2012**, 2, 178; b) F. Bonino, C. Lamberti, S. Chavan, J. Vitillo, S. Bordiga, in *Metal Organic Frameworks as Heterogeneous Catalysts*, (Eds: F. Llabres i Xamena, J. Gascon), RSC Publishing, Cambridge, UK **2013**, p. 76; c) N. Nijem, Y. Chabal, *Comments Inorg. Chem.* **2014**, 34, 78; d) V. Panchenko, S. Jhung, M. Timofeeva, *Russ. Chem. Bull.* **2015**, 8, 1772; e) F. Bonino, C. Lamberti, S. Bordiga, in *The Chemistry of Metal-Organic Frameworks: Synthesis, Characterization, and Applications*, (Ed: S. Kaskel), Wiley-VCH Verlag GmbH & Co. KGaA, Weinheim **2016**, Ch. 22, p. 657; f) V. Panchenko, M. Timofeeva, S. Jhung, *Catal. Rev. Sci. Eng.* **2016**, 58, 209; g) K. Tan, Y. Chabal, in *Metal-Organic Frameworks*, (Eds: F. Zafar, E. Sharmin), InTechOpen, London, **2016**, p. 19; h) L. Bobadilla, L. Oliviero, F. Romero-Sarria, M. Daturi, in *Zeolites and Metal-Organic Frameworks*, (Eds: V. Blay, L. Bobadilla, A. Cabrera), Atlantis Press/Amsterdam University Press, Amsterdam **2018**, Ch. 3, p. 53.
- [31] B. Chon, S. Xu, Y. Lee, *Anal. Chem.* **2021**, 93, 2215.
- [32] a) J. Shi, C. Mahr, M. Murshed, T. Gesing, A. Rosenauer, M. Bäumer, A. Wittstock, *Phys. Chem. Chem. Phys.* **2017**, 19, 8880; b) V. Bon, E. Brunner, A. Pöpl, S. Kaskel, *Adv. Funct. Mater.* **2020**, 30, 1907847; c) G. Paul, C. Bisio, I. Braschi, M. Cossi, G. Gatti, E. Gianotti, L. Marchese, *Chem. Soc. Rev.* **2018**, 47, 5684; d) A. Bieberle-Hütter, A. Bronneberg, K. George, M. Van De Sanden, *J. Phys. D Appl. Phys.* **2021**, 54, 133001; e) K. Hadjiivanov, in *Advances in Catalysis*, 57, (Ed: F. Jentoft), Academic Press, USA **2014**, Ch. 2, p. 99.
- [33] a) D. Long, *The Raman Effect: A Unified Treatment of the Theory of Raman Scattering by Molecules*, John Wiley & Sons Ltd, West Sussex, UK **2002**; b) M. Pelletier, C. Pelletier, in *Raman, Infrared, and Near-Infrared Chemical Imaging*, (Eds: S. Šašić, Y. Ozaki), John Wiley & Sons, Inc., Hoboken, NJ **2010**, p. 1; c) J. Kneipp, H. Kneipp, K. Kneipp, *Chem. Soc. Rev.* **2008**, 37, 1052; d) E. O. Potma, S. Mukamel, in *Coherent Raman Scattering Microscopy*, (Eds: J. Cheng, X. Xie), CRC Press, Boca Raton **2016**, Ch. 1, p. 24; e) F. Hu, L. Shi, W. Min, *Nat. Methods* **2019**, 16, 830.
- [34] K. Hofmann, F. Küspert, *Z. Anorg. Chem.* **1897**, 15, 204.
- [35] A. Werner, *Ber. Dtsch. Chem. Ges.* **1907**, 40, 4817.
- [36] R. Raman, K. Krishnan, *Nature* **1928**, 121, 501.
- [37] a) J. Brandmüller, *Fresenius J. Anal. Chem.* **1959**, 170, 29; b) J. Behringer, *Z. Elektrochem* **1958**, 62, 544; c) J. Behringer, *Z. Elektrochem* **1958**, 62, 906; d) A. Albrecht, *J. Chem. Phys.* **1961**, 34, 1476; e) W. Hofmann, H. Moser, *Ber. Bunsenges. Phys. Chem.* **1964**, 68, 129.
- [38] Y. Kinoshita, I. Matsubara, T. Higuchi, Y. Saito, *Bull. Chem. Soc. Jpn.* **1959**, 32, 1221.
- [39] a) A. Schawlow, C. Townes, *Phys. Rev.* **1958**, 112, 1940; b) T. Maiman, *Nature* **1960**, 187, 493.

- [40] a) E. Woodbury, W. Ng, *Proc. IRE* **1962**, *50*, 2367; b) G. Eckhardt, R. Hellwarth, F. McClung, S. Schwarz, D. Weiner, E. Woodbury, *Phys. Rev. Lett.* **1962**, *9*, 455.
- [41] a) R. Hellwarth, *Phys. Rev.* **1963**, *130*, 1850; b) N. Bloembergen, *Am. J. Phys.* **1967**, *35*, 989.
- [42] R. Terhune, P. Maker, C. Savage, *Phys. Rev. Lett.* **1965**, *14*, 681.
- [43] M. Fleisichmann, P. Hendra, A. Mcquillan, *Chem. Phys. Lett.* **1974**, *26*, 163.
- [44] a) M. Albrecht, J. Creighton, *J. Am. Chem. Soc.* **1977**, *99*, 5215; b) D. Jeanmaire, R. Van Duyne, *J. Electroanal. Chem. Interfacial Electrochem.* **1977**, *84*, 1.
- [45] M. Duncan, J. Reintjes, T. Manuccia, *Opt. Lett.* **1982**, *7*, 350.
- [46] a) B. Hoskins, R. Robson, *J. Am. Chem. Soc.* **1989**, *111*, 5962; b) B. Hoskins, R. Robson, *J. Am. Chem. Soc.* **1990**, *112*, 1546.
- [47] G. Puppels, F. De Mul, C. Otto, J. Greve, M. Robert-Nicoud, D. Arndt-Jovin, T. Jovin, *Nature* **1990**, *347*, 301.
- [48] O. Yaghi, H. Li, *J. Am. Chem. Soc.* **1995**, *117*, 10401.
- [49] O. Yaghi, G. Li, H. Li, *Nature* **1995**, *378*, 703.
- [50] M. Kondo, T. Yoshitomi, H. Matsuzaka, S. Kitagawa, K. Seki, *Angew. Chem. Int. Ed.* **1997**, *36*, 1725.
- [51] H. Li, M. Eddaoudi, T. Groy, O. Yaghi, *J. Am. Chem. Soc.* **1998**, *120*, 8571.
- [52] a) H. Li, M. Eddaoudi, M. O'Keeffe, O. Yaghi, *Nature* **1999**, *402*, 276; b) M. Yoshizawa, M. Kurosawa, *Phys. Rev. A* **1999**, *61*, 013808; c) A. Zumbusch, G. Holtom, X. Xie, *Phys. Rev. Lett.* **1999**, *82*, 4142.
- [53] a) M. Anderson, *Appl. Phys. Lett.* **2000**, *76*, 3130; b) N. Hayazawa, Y. Inouye, Z. Sekkat, S. Kawata, *Opt. Commun.* **2000**, *183*, 333; c) R. Stöckle, Y. Suh, V. Deckert, R. Zenobi, *Chem. Phys. Lett.* **2000**, *318*, 131.
- [54] J. Cheng, A. Volkmer, L. Book, X. Xie, *J. Phys. Chem. B* **2002**, *106*, 8493.
- [55] a) N. Ockwig, O. Delgado-Friedrichs, M. O'Keeffe, O. Yaghi, *Acc. Chem. Res.* **2005**, *38*, 176; b) O. Yaghi, *ACS Cent. Sci.* **2019**, *5*, 1295; c) M. O'Keeffe, M. Peskov, S. Ramsden, O. Yaghi, *Acc. Chem. Res.* **2008**, *41*, 1782; d) Z. Chen, H. Jiang, M. Li, M. O'Keeffe, M. Eddaoudi, *Chem. Rev.* **2020**, *120*, 8039.
- [56] a) A. Cortes, A. Benin, N. Ockwig, M. O'Keeffe, A. Matzger, O. Yaghi, *Science* **2005**, *310*, 1166; b) H. El-Kaderi, J. Hunt, J. Mendoza-Cortes, A. Cortes, R. Taylor, M. O'Keeffe, O. Yaghi, *Science* **2007**, *316*, 268.
- [57] a) K. Park, Z. Ni, A. Côté, J. Choi, R. Huang, F. Uribe-Romo, H. Chae, M. O'Keeffe, O. Yaghi, *Proc. Natl. Acad. Sci. U.S.A.* **2006**, *103*, 10186; b) R. Banerjee, A. Phan, B. Wang, C. Knobler, H. Furukawa, M. O'Keeffe, O. Yaghi, *Science* **2008**, *319*, 939.
- [58] S. Schlücker, B. Küstner, A. Punge, R. Bonfig, A. Marx, P. Ströbel, *J. Raman Spectrosc.* **2006**, *37*, 719.
- [59] a) E. Ploetz, S. Laimgruber, S. Berner, W. Zinth, P. Gilch, *Appl. Phys. B* **2007**, *87*, 389; b) C. Freudiger, W. Min, B. Saar, S. Lu, G. Holtom, C. He, J. Tsai, J. Kang, X. Xie, *Science* **2008**, *322*, 1857; c) P. Nandakumar, A. Kovalev, A. Volkmer, *New J. Phys.* **2009**, *11*, 033026; d) Y. Ozeki, F. Dake, S. Kajiyama, K. Fukui, K. Itoh, *Opt. Express* **2009**, *17*, 3651; e) E. Andresen, P. Berto, H. Rigneault, *Opt. Lett.* **2011**, *36*, 2387; f) H. Beier, G. Noojin, B. Rockwell, *Opt. Express* **2011**, *19*, 18885; g) Y. Ozeki, W. Umemura, K. Sumimura, N. Nishizawa, K. Fukui, K. Itoh, *Opt. Lett.* **2012**, *37*, 431; h) D. Fu, G. Holtom, C. Freudiger, X. Zhang, X. Xie, *J. Phys. Chem. B* **2013**, *117*, 4634.
- [60] J. Li, Y. Huang, Y. Ding, Z. Yang, S. Li, X. Zhou, F. Fan, W. Zhang, Z. Zhou, D. Wu, B. Ren, Z. Wang, Z. Tian, *Nature* **2010**, *464*, 392.
- [61] a) N. Nijem, P. Thissen, Y. Yao, R. Longo, K. Roodenko, H. Wu, Y. Zhao, K. Cho, J. Li, D. Langreth, Y. Chabal, *J. Am. Chem. Soc.* **2011**, *133*, 12849; b) P. Kanoo, S. Reddy, G. Kumari, R. Haldar, C. Narayana, S. Balasubramanian, T. Maji, *Chem. Commun.* **2012**, *48*, 8487; c) N. Nijem, H. Wu, P. Canepa, A. Marti, K. Balkus, T. Thonhauser, J. Li, Y. Chabal, *J. Am. Chem. Soc.* **2012**, *134*, 15201; d) K. Tan, N. Nijem, P. Canepa, Q. Gong, J. Li, T. Thonhauser, Y. Chabal, *Chem. Mater.* **2012**, *24*, 3153; e) Y. Chen, J. Zhang, J. Li, J. Lockard, *J. Phys. Chem. C* **2013**, *117*, 20068; f) N. Nijem, P. Canepa, U. Kaipa, K. Tan, K. Roodenko, S. Tekarli, J. Halbert, I. Oswald, R. Arvapally, C. Yang, T. Thonhauser, M. Omary, Y. Chabal, *J. Am. Chem. Soc.* **2013**, *135*, 12615.
- [62] a) K. Sugikawa, Y. Furukawa, K. Sada, *Chem. Mater.* **2011**, *23*, 3132; b) K. Sugikawa, S. Nagata, Y. Furukawa, K. Kokado, K. Sada, *Chem. Mater.* **2013**, *25*, 2565; c) Y. Hu, J. Liao, D. Wang, G. Li, *Anal. Chem.* **2014**, *86*, 3955.
- [63] a) W. Silva, C. Graefe, R. Frontiera, *ACS Photonics* **2016**, *3*, 79; b) Y. Bi, C. Yang, Y. Chen, S. Yan, G. Yang, Y. Wu, G. Zhang, P. Wang, *Light Sci. Appl.* **2018**, *7*, 81; c) C. Graefe, D. Punihaole, C. Harris, M. Lynch, R. Leighton, R. Frontiera, *Anal. Chem.* **2019**, *91*, 8723; d) L. Gong, W. Zheng, Y. Ma, Z. Huang, *Nat. Photonics* **2020**, *14*, 115; e) P. Upputuri, Z. Wu, Li Gong, C. Ong, H. Wang, *Opt. Express* **2014**, *22*, 12890; f) R. Leighton, A. Alperstein, R. Frontiera, *Annu. Rev. Anal. Chem.* **2022**, *15*, 37; g) J. Shou, A. Komazawa, Y. Wachi, M. Kawatani, H. Fujioka, S. Spratt, T. Mizuguchi, K. Oguchi, H. Akaboshi, F. Obata, R. Tachibana, S. Yasunaga, Y. Mita, Y. Misawa, R. Kojima, Y. Urano, M. Kamiya, Y. Ozeki, *Sci. Adv.* **2022**, *9*, eade9118; h) X. Lv, L. Gong, S. Lin, P. Jin, Z. Huang, *Opt. Lett.* **2022**, *47*, 4552; i) L. Shi, A. Klimas, B. Gallagher, Z. Cheng, F. Fu, P. Wijesekera, Y. Miao, Xi Ren, Y. Zhao, W. Min, *Adv. Sci.* **2022**, *9*, 2200315; j) H. Jang, Y. Li, A. Fung, P. Bagheri, K. Hoang, D. Skowronska-Krawczyk, X. Chen, J. Wu, B. Bintu, L. Shi, *Nat. Methods* **2023**, *20*, 448; k) L. Shi, H. Jang, *Acc. Mater. Res.* **2023**, *4*, 726.
- [64] a) A. Fuchs, P. Mannhardt, P. Hirschle, H. Wang, I. Zaytseva, Z. Ji, O. Yaghi, S. Wuttke, E. Ploetz, *Adv. Mater.* **2022**, *34*, 2104530; b) A. Fuchs, F. Knechtel, H. Wang, Z. Ji, S. Wuttke, O. M. Yaghi, E. Ploetz, *J. Am. Chem. Soc.* **2023**, *145*, 14324.
- [65] Z. Cai, Li-Q Zheng, Y. Zhang, R. Zenobi, *J. Am. Chem. Soc.* **2021**, *143*, 12380.
- [66] C. Huang, A. Li, X. Chen, T. Wang, *Small* **2020**, *16*, e2004802.
- [67] a) A. Penzkofer, A. Laubereau, W. Kaiser, *Prog. Quantum Electron.* **1979**, *6*, 55; b) R. Boyd, in *Nonlinear Optics*, Academic Press, Burlington **2008**.
- [68] a) B. Chase, *Appl. Spectrosc.* **1994**, *48*, 14A; b) O. Hollricher, in *Confocal Raman Microscopy*, (Eds: T. Dieing, O. Hollricher, J. Toporski), Springer Berlin, Heidelberg **2010**, Ch. 3, p. 43; c) R. Salzer, H. Siesler, *Infrared and Raman spectroscopic imaging*, John Wiley & Sons, Hoboken, **2014**; d) D. Polli, V. Kumar, C. M. Valensise, M. Marangoni, G. Cerullo, *Laser Photonics Rev.* **2018**, *12*, 1800020; e) H. Rigneault, P. Berto, *APL Photon.* **2018**, *3*, 091101; f) J. Homola, *Anal. Bioanal. Chem.* **2011**, *401*, 2329; g) J. Cheng, X. Xie, *Coherent Raman Scattering Microscopy*, Taylor & Francis, UK **2012**.
- [69] a) N. Stock, S. Biswas, *Chem. Rev.* **2012**, *112*, 933; b) M. Rubio-Martinez, C. Avci-Camur, A. Thornton, I. Imaz, D. MasPOCH, M. Hill, *Chem. Soc. Rev.* **2017**, *46*, 3453; c) M. Ding, X. Cai, H. Jiang, *Chem. Sci.* **2019**, *10*, 10209.
- [70] a) R. Freund, O. Zaremba, G. Arnauts, R. Ameloot, G. Skorupskii, M. Dinca, A. Bavykina, J. Gascon, A. Ejsmont, J. Goscianska, M. Kalmutzki, U. Lächelt, E. Ploetz, C. S. Diercks, S. Wuttke, *Angew. Chem. Int. Ed.* **2021**, *60*, 23975; b) N. Hanikel, M. Prévot, O. Yaghi, *Nat. Nanotechnol.* **2020**, *15*, 348; c) H. Furukawa, K. Cordova, M. O'Keeffe, O. Yaghi, *Science* **2013**, *341*, 1230444.
- [71] a) A. Howarth, A. Peters, N. Vermeulen, T. Wang, J. Hupp, O. Farha, *Chem. Mater.* **2017**, *29*, 26; b) F. Ambroz, T. Macdonald, V. Martis, I. Parkin, *Small Methods* **2018**, *2*, 1800173.
- [72] a) J. Langer, D. Jimenez De Aberasturi, J. Aizpurua, R. Alvarez-Puebla, B. Auguié, J. Baumberg, G. Bazan, S. Bell, A. Boisen, A. Brolo, J. Choo, D. Cialla-May, V. Deckert, L. Fabris, K. Faulds, F. García De Abajo, R. Goodacre, D. Graham, A. Haes, C. Haynes, C. Huck, T. Itoh, M. Käll, J. Kneipp, N. Kotov, H. Kuang, E. Le Ru, H. Lee, J. Li, X. Ling, et al., *ACS Nano* **2020**, *14*, 28; b) C. Evans, X. Xie,

- Annu. Rev. Anal. Chem.* **2008**, *1*, 883; c) R. Prince, R. Frontiera, E. Potma, *Chem. Rev.* **2017**, *117*, 5070.
- [73] N. Colthup, *Introduction to Infrared and Raman spectroscopy*, Elsevier, **1990**.
- [74] A. Smekal, *Naturwissenschaften* **1923**, *11*, 873.
- [75] C. Raman, K. Krishnan, *Nature* **1928**, *121*, 711.
- [76] G. Landsberg, L. Mandelstam, *Naturwissenschaften* **1928**, *16*, 557.
- [77] G. Placzek, in *Handbuch der Radiologie*, Vol. 6, (Ed: E. Marx), Akademische Verlagsgesellschaft, Leipzig **1934**, p. 205.
- [78] R. Aroca, in *Surface-Enhanced Vibrational Spectroscopy*, John Wiley & Sons, Ltd, West Sussex, UK **2006**, p. 1.
- [79] E. Smith, G. Dent, *Modern Raman Spectroscopy: A Practical Approach*, John Wiley & Sons, Ltd, West Sussex, UK **2005**.
- [80] R. Crichton, in *Biological Inorganic Chemistry*, Academic Press, Oxford, UK **2019**, Ch. 6, p. 149.
- [81] C. Leong, B. Chan, T. Faust, D. D'alessandro, *Chem. Sci.* **2014**, *5*, 4724.
- [82] P. Usov, C. Leong, B. Chan, M. Hayashi, H. Kitagawa, J. Sutton, K. Gordon, I. Hod, O. Farha, J. Hupp, M. Addicoat, A. Kuc, T. Heine, D. D'alessandro, *Phys. Chem. Chem. Phys.* **2018**, *20*, 25772.
- [83] a) H. Kramers, W. Heisenberg, *Z. Phys.* **1925**, *31*, 681; b) P. Dirac, *Proc. R. Soc. A: Math. Phys. Eng. Sci.* **1927**, *114*, 243; c) D. Tannor, *Introduction to Quantum Mechanics: A Time-Dependent Perspective*, University Science Books, Sausalito, CA **2006**; d) B. Schrader, *Infrared and Raman Spectroscopy: Methods and Applications*, John Wiley & Sons, xx xx **2008**.
- [84] a) E. Le Ru, E. Blackie, M. Meyer, P. Etchegoin, *J. Phys. Chem. C* **2007**, *111*, 13794; b) S. Ding, J. Yi, J. Li, B. Ren, D. Wu, R. Panneerselvam, Z. Tian, *Nat. Rev. Mater.* **2016**, *1*, 16021.
- [85] P. Stiles, J. Dieringer, N. Shah, R. Van Duyne, *Annu. Rev. Anal. Chem.* **2008**, *1*, 601.
- [86] W. Wei, S. Li, J. Millstone, M. Banholzer, X. Chen, X. Xu, G. Schatz, C. Mirkin, *Angew. Chem. Int. Ed.* **2009**, *48*, 4210.
- [87] J. Dieringer, A. McFarland, N. Shah, D. Stuart, A. Whitney, C. Yonzon, M. Young, X. Zhang, R. Van Duyne, *Faraday Discuss.* **2006**, *132*, 9.
- [88] B. Liu, B. Thielert, A. Reutter, R. Stosch, P. Lemmens, *J. Phys. Chem. C* **2019**, *123*, 19119.
- [89] R. Birke, J. Lombardi, in *Spectroelectrochemistry: Theory and Practice*, (Ed: R. Gale), Springer US, Boston, MA **1988**, p. 263.
- [90] a) S. Bell, G. Charron, E. Cortés, J. Kneipp, M. De La Chapelle, J. Langer, M. Procházka, V. Tran, S. Schlücker, *Angew. Chem. Int. Ed.* **2020**, *59*, 5454; b) R. Jones, D. Hooper, L. Zhang, D. Wolverson, V. Valev, *Nanoscale Res. Lett.* **2019**, *14*, 231; c) A. Orlando, F. Franceschini, C. Muscas, S. Pidkova, M. Bartoli, M. Rovere, A. Tagliaferro, *Chemosensors* **2021**, *9*, 262; d) R. Aroca, in *Surface-Enhanced Vibrational Spectroscopy*, John Wiley & Sons, Ltd, West Sussex, UK **2006**, Ch. 3, p. 73; e) B. Hecht, L. Novotny, in *Principles of Nano-Optics*, Cambridge University Press, Cambridge **2006**, Ch. 12, p. 378; f) S. Maier, in *Plasmonics: Fundamentals and Applications*, Springer US, New York, NY **2007**, p. 21; g) S. Maier, in *Plasmonics: Fundamentals and Applications*, Springer US, New York, NY **2007**, p. 65.
- [91] S. George, in *Self-standing Substrates: Materials and Applications*, (Eds: Inamuddin, R. Boddula, A. M. Asiri), Springer International Publishing, Cham **2020**, p. 83.
- [92] S. Youn, T. Rho, B. Min, K. Kim, *Phys. Status Solidi B Basic Res.* **2007**, *244*, 1354.
- [93] J. Homola, in *Surface Plasmon Resonance Based Sensors*, Springer Berlin, Berlin, Heidelberg **2006**, Ch. 1, p. 3.
- [94] R. Aroca, in *Surface-Enhanced Vibrational Spectroscopy*, John Wiley & Sons, Ltd, West Sussex, UK **2006**, Ch. 2, p. 35.
- [95] X. Huang, M. El-Sayed, *J. Adv. Res.* **2010**, *1*, 13.
- [96] M. Constantinou, K. Hadjiageorgiou, S. Abalde-Cela, C. Andreou, *ACS Appl. Nano Mater.* **2022**, *5*, 12276.
- [97] B. Sharma, R. Frontiera, A. Henry, E. Ringe, R. Van Duyne, *Mater. Today* **2012**, *15*, 16.
- [98] a) T. Yu, C. Ho, C. Wu, C. Chien, C. Lin, S. Lee, *J. Raman Spectrosc.* **2013**, *44*, 1506; b) H. Sun, S. Cong, Z. Zheng, Z. Wang, Z. Chen, Z. Zhao, *J. Am. Chem. Soc.* **2019**, *141*, 870.
- [99] L. Wu, H. Pu, L. Huang, D. Sun, *Food Chem.* **2020**, *328*, 127105.
- [100] C. Koh, H. Lee, X. Han, H. Sim, X. Ling, *Chem. Commun.* **2018**, *54*, 2546.
- [101] a) K. Yang, S. Zong, Y. Zhang, Z. Qian, Y. Liu, K. Zhu, L. Li, Na Li, Z. Wang, Y. Cui, *ACS Appl. Mater. Interfaces* **2020**, *12*, 1395; b) G. Phan-Quang, N. Yang, H. Lee, H. Sim, C. Koh, Y. Kao, Z. Wong, E. Tan, Y. Miao, W. Fan, T. Liu, I. Phang, X. Ling, *ACS Nano* **2019**, *13*, 12090; c) Y. Cai, Y. Wu, T. Xuan, X. Guo, Y. Wen, H. Yang, *ACS Appl. Mater. Interfaces* **2018**, *10*, 15412.
- [102] S. Bell, M. Mccourt, *Phys. Chem. Chem. Phys.* **2009**, *11*, 7455.
- [103] B. Ren, X. Lin, Z. Yang, G. Liu, R. Aroca, B. Mao, Z. Tian, *J. Am. Chem. Soc.* **2003**, *125*, 9598.
- [104] D. Chase, B. Parkinson, *Appl. Spectrosc.* **1988**, *42*, 1186.
- [105] a) S. Nie, L. Lipscomb, N. Yu, *Appl. Spectrosc. Rev.* **1991**, *26*, 203; b) E. Liang, A. Weippert, J. Funk, A. Materny, W. Kiefer, *Chem. Phys. Lett.* **1994**, *227*, 115; c) L. Buchanan, N. Gruenke, M. Mcanally, B. Negru, H. Mayhew, V. Apkarian, G. Schatz, R. Van Duyne, *J. Phys. Chem. Lett.* **2016**, *7*, 4629.
- [106] B. Pettinger, B. Ren, G. Picardi, R. Schuster, G. Ertl, *Phys. Rev. Lett.* **2004**, *92*, 096101.
- [107] P. Verma, *Chem. Rev.* **2017**, *117*, 6447.
- [108] R. Zhang, Y. Zhang, Z. Dong, S. Jiang, C. Zhang, L. Chen, L. Zhang, Y. Liao, J. Aizpurua, Y. Luo, J. Yang, J. Hou, *Nature* **2013**, *498*, 82.
- [109] a) C. Zhang, D. Zhang, J. Cheng, *Annu. Rev. Biomed. Eng.* **2015**, *17*, 415; b) C. Krafft, I. Schie, T. Meyer, M. Schmitt, J. Popp, *Chem. Soc. Rev.* **2016**, *45*, 1819.
- [110] a) M. Müller, A. Zumbusch, *ChemPhysChem* **2007**, *8*, 2156; b) Q. Cheng, Y. Miao, J. Wild, W. Min, Y. Yang, *Matter* **2021**, *4*, 1460.
- [111] W. Tipping, M. Lee, A. Serrels, V. Brunton, A. Hulme, *Chem. Soc. Rev.* **2016**, *45*, 2075.
- [112] a) N. Mazumder, N. Balla, G. Zhuo, Y. Kistenev, R. Kumar, F. Kao, S. Brasselet, V. Nikolaev, N. Krivova, *Front. Phys.* **2019**, *7*, 170; b) W. Peterson, K. Hiramatsu, K. Goda, *Light Sci. Appl.* **2023**, *12*, 113; c) C. Camp Jr., M. Cicerone, *Nat. Photonics* **2015**, *9*, 295.
- [113] J. Cheng, *Appl. Spectrosc.* **2007**, *61*, 197A.
- [114] R. Begley, A. Harvey, R. Byer, *Appl. Phys. Lett.* **2003**, *25*, 387.
- [115] a) J. Cheng, L. Book, X. Xie, *Opt. Lett.* **2001**, *26*, 1341; b) C. Evans, E. Potma, M. Puoris'haag, D. Côté, C. Lin, X. Xie, *Proc. Natl. Acad. Sci. U.S.A.* **2005**, *102*, 16807; c) F. Ganikhanov, C. Evans, B. Saar, X. Xie, *Opt. Lett.* **2006**, *31*, 1872; d) Y. Liu, Y. Lee, M. Cicerone, *Opt. Lett.* **2009**, *34*, 1363.
- [116] W. Min, C. Freudiger, S. Lu, X. Xie, *Annu. Rev. Phys. Chem.* **2011**, *62*, 507.
- [117] H. Ghaziaskar, E. Lai, *Appl. Spectrosc. Rev.* **1992**, *27*, 245.
- [118] a) E. Ploetz, B. Marx, P. Gilch, *J. Raman Spectrosc.* **2010**, *41*, 609; b) E. Ploetz, B. Marx, P. Gilch, *J. Raman Spectrosc.* **2011**, *42*, 1875.
- [119] D. Skoog, F. Holler, S. Crouch, *Principles of Instrumental Analysis*, Cengage Learning, Inc., Boston, MA **2017**.
- [120] R. Clark, B. Stewart, *The resonance Raman effect—Review of the theory and of applications in inorganic chemistry*, Springer, Berlin, Heidelberg **1979**.
- [121] A. Sakudo, *Clin. Chim. Acta* **2016**, *455*, 181.
- [122] S. Laimgruber, H. Schachenmayr, B. Schmidt, W. Zinth, P. Gilch, *Appl. Phys. B* **2006**, *85*, 557.
- [123] E. Ploetz, B. Marx, T. Klein, R. Huber, P. Gilch, *Opt. Express* **2009**, *17*, 18612.
- [124] a) N. Lee, R. Hartschuh, D. Mehtani, A. Kisliuk, J. Maguire, M. Green, M. Foster, A. Sokolov, *J. Raman Spectrosc.* **2007**, *38*, 789; b)

- Y. Saito, M. Motohashi, N. Hayazawa, S. Kawata, *J. Microsc.* **2008**, 229, 217.
- [125] a) P. Treado, I. Levin, E. Lewis, *Appl. Spectrosc.* **1992**, 46, 1211; b) S. Goldstein, L. Kidder, T. Herne, I. Levin, E. Lewis, *J. Microsc.* **1996**, 184, 35; c) H. Morris, C. Hoyt, P. Miller, P. Treado, *Appl. Spectrosc.* **1996**, 50, 805; d) J. Ma, D. Ben-Amotz, *Appl. Spectrosc.* **1997**, 51, 1845; e) M. Nelson, M. Myrick, *Appl. Spectrosc.* **1999**, 53, 751; f) H. Li, W. Luo, G. Li, G. Zhang, P. Zhang, C. Li, Y. Gu, *Rev. Sci. Instrum.* **2018**, 89, 083103; g) W. Müller, M. Kielhorn, M. Schmitt, J. Popp, R. Heintzmann, *Optica* **2016**, 3, 452.
- [126] J. Xing, S. Kang, Y. Choi, S. Lee, H. Yoo, *Meas. Sci. Technol.* **2020**, 31, 025203.
- [127] S. Ayas, G. Cinar, A. Ozkan, Z. Soran, O. Ekiz, D. Kocaay, A. Tomak, P. Toren, Y. Kaya, I. Tunc, H. Zareie, T. Tekinay, A. Tekinay, M. Guler, A. Dana, *Sci. Rep.* **2013**, 3, 2624.
- [128] a) C. Ceconello, F. Vernuccio, A. De La Cadena, A. Bresci, F. Manetti, S. Das, R. Vanna, G. Cerullo, D. Polli, *EPJ Web Conf* **2022**, 266, 08001; b) C. Heinrich, S. Bernet, M. Ritsch-Marte, *Appl. Phys. Lett.* **2004**, 84, 816.
- [129] N. Kumar, S. Mignuzzi, W. Su, D. Roy, *EPJ Tech. Instrum.* **2015**, 2, 9.
- [130] a) P. Dorenbos, J. De Haas, R. Visser, C. Van Eijk, R. Hollander, *IEEE Trans. Nucl. Sci.* **1993**, 40, 424; b) M. Pelletier, C. Pelletier, in *Encyclopedia of Analytical Science*, (Eds: P. Worsfold, A. Townshend, C. Poole), Elsevier, Oxford **2005**, p. 94.
- [131] A. Wright, *The Photomultiplier Handbook*, Oxford University Press, Oxford, UK **2017**.
- [132] R. LaBelle, S. Garvey, presented at ICIASF '95 Record. International Congress on Instrumentation in Aerospace Simulation Facilities, 18–21 July 1995, **1995**.
- [133] M. Czerny, A. Turner, *Z. Phys.* **1930**, 61, 792.
- [134] R. Kizil, J. Irudayaraj, in *Modern Techniques for Food Authentication*, (Ed: D. Sun), Academic Press, Oxford, UK **2018**, Ch. 6, p. 193.
- [135] a) M. Tamamitsu, Y. Sakaki, T. Nakamura, G. Podagatlapalli, T. Ideguchi, K. Goda, *Vib. Spectrosc.* **2017**, 91, 163; b) K. Hashimoto, J. Omachi, T. Ideguchi, *Opt. Express* **2018**, 26, 14307.
- [136] a) G. De Vito, A. Bifone, V. Piazza, *Opt. Express* **2012**, 20, 29369; b) P. Gucciardi, M. de La Chapelle, J. Valmalette, G. Picardi, R. Ossikovski, in *Scanning Probe Microscopy in Nanoscience and Nanotechnology*, (Ed: B. Bhushan), Springer, Berlin, Heidelberg **2010**, Ch. 3, p. 57; c) H. Kerdoncuff, M. R. Pollard, P. G. Westergaard, J. C. Petersen, M. Lassen, *Opt. Express* **2017**, 25, 5618; d) P. Dong, C. Zong, Z. Dagher, J. Hui, J. Li, Y. Zhan, M. Zhang, M. Mansour, J. Cheng, *Sci. Adv.* **2021**, 7, eabd5230.
- [137] A. Ciupa, M. Ptak, *Vib. Spectrosc.* **2016**, 86, 67.
- [138] L. Barron, L. Hecht, I. Mccoll, E. Blanch, *Mol. Phys.* **2004**, 102, 731.
- [139] V. Kumar, S. Schlücker, in *Molecular and Laser Spectroscopy: Advances and Applications*, 3, (Ed: V. Gupta), Elsevier, Amsterdam **2022**, Ch. 4, p. 101.
- [140] X. Xiao, R. Gillibert, A. Foti, P. Coulon, C. Ulysse, T. Levato, S. Maier, V. Giannini, P. Gucciardi, G. Rizza, *Nano Lett.* **2023**, 23, 2530.
- [141] S. Krause, J. Evans, V. Bon, S. Crespi, W. Danowski, W. Browne, S. Ehrling, F. Walenzus, D. Wallacher, N. Grimm, D. Töbrens, M. Weiss, S. Kaskel, B. Feringa, *Nat. Commun.* **2022**, 13, 1951.
- [142] F. Zaera, *J. Catal.* **2021**, 404, 900.
- [143] a) H. Hamaguchi, T. Gustafson, *Annu. Rev. Phys. Chem.* **1994**, 45, 593; b) S. Bell, *Analyst* **1996**, 121, 107R.
- [144] T. Lipiäinen, J. Pessi, P. Movahedi, J. Koivistoinen, L. Kurki, M. Tenhunen, J. Yliruusi, A. Juppo, J. Heikkonen, T. Pahikkala, C. Strachan, *Anal. Chem.* **2018**, 90, 4832.
- [145] E. Garbacik, J. Herek, C. Otto, H. Offerhaus, *J. Raman Spectrosc.* **2012**, 43, 651.
- [146] Y. Ozeki, *ITE Tech. Rep.* **2014**, 38, 65.
- [147] L. Czerwinski, J. Nixdorf, G. Di Florio, P. Gilch, *Opt. Lett.* **2016**, 41, 3021.
- [148] G. Kumari, N. Patil, V. Bhadram, R. Haldar, S. Bonakala, T. Maji, C. Narayana, *J. Raman Spectrosc.* **2016**, 47, 149.
- [149] A. Krylov, A. Vtyurin, P. Petkov, I. Senkovska, M. Maliuta, V. Bon, T. Heine, S. Kaskel, E. Slyusareva, *Phys. Chem. Chem. Phys.* **2017**, 19, 32099.
- [150] J. Seo, C. Bonneau, R. Matsuda, M. Takata, S. Kitagawa, *J. Am. Chem. Soc.* **2011**, 133, 9005.
- [151] G. Kumari, K. Jayaramulu, T. Maji, C. Narayana, *J. Phys. Chem. A* **2013**, 117, 11006.
- [152] a) Y. Qi, H. Xu, X. Li, B. Tu, Q. Pang, X. Lin, E. Ning, Q. Li, *Chem. Mater.* **2018**, 30, 5478; b) S. Kusaka, Y. Nakajima, A. Hori, A. Yonezu, K. Kikushima, W. Kosaka, Y. Ma, R. Matsuda, *Faraday Discuss.* **2021**, 225, 70.
- [153] R. Kitaura, S. Kitagawa, Y. Kubota, T. Kobayashi, K. Kindo, Y. Mita, A. Matsuo, M. Kobayashi, H. Chang, T. Ozawa, M. Suzuki, M. Sakata, M. Takata, *Science* **2002**, 298, 2358.
- [154] D. Siberio-Pérez, A. Wong-Foy, O. Yaghi, A. Matzger, *Chem. Mater.* **2007**, 19, 3681.
- [155] P. Andrade, N. Henry, C. Volkringer, T. Loiseau, H. Vezin, M. Hureau, A. Moissette, *ACS Appl. Mater. Interfaces* **2022**, 14, 29916.
- [156] K. Nath, A. Ahmed, D. Siegel, A. Matzger, *J. Am. Chem. Soc.* **2022**, 144, 20939.
- [157] W. Danowski, T. Van Leeuwen, S. Abdolazadeh, D. Roke, W. Browne, S. Wezenberg, B. Feringa, *Nat. Nanotechnol.* **2019**, 14, 488.
- [158] a) A. Hobro, B. Lendl, *Trends Anal.* **2009**, 28, 1235; b) Y. He, Y. Wang, X. Yang, S. Xie, R. Yuan, Y. Chai, *ACS Appl. Mater. Interfaces* **2016**, 8, 7683.
- [159] T. Petersen, G. Balakrishnan, C. Weeks, *Dalton Trans.* **2015**, 44, 12824.
- [160] Y. Ma, W. Lu, X. Han, Y. Chen, I. Da Silva, D. Lee, A. Sheveleva, Z. Wang, J. Li, W. Li, M. Fan, S. Xu, F. Tuna, E. McInnes, Y. Cheng, S. Rudic, P. Manuel, M. D. Frogley, A. Ramirez-Cuesta, M. Schröder, S. Yang, *J. Am. Chem. Soc.* **2022**, 144, 8624.
- [161] J. Liu, Z. Jiang, S. Hsu, *ACS Appl. Mater. Interfaces* **2023**, 15, 6716.
- [162] X. Li, L. Lachmanskii, S. Safi, S. Sene, C. Serre, J. M. Grenèche, J. Zhang, R. Gref, *Sci. Rep.* **2017**, 7, 13142.
- [163] E. Ploetz, A. Zimpel, V. Cauda, D. Bauer, D. Lamb, C. Haisch, S. Zahler, A. Vollmar, S. Wuttke, H. Engelke, *Adv. Mater.* **2020**, 32, 1907267.
- [164] C. Carrillo-Carrión, R. Martínez, M. Navarro Poupard, B. Pelaz, E. Polo, A. Arenas-Vivo, A. Olgiati, P. Taboada, M. Soliman, Ú. Catalán, S. Fernández-Castillejo, R. Solà, W. Parak, P. Horcajada, R. Alvarez-Puebla, P. Del Pino, *Angew. Chem. Int. Ed.* **2019**, 58, 7078.
- [165] T. Mofokeng, A. Ipadeola, Z. Tetana, K. Ozoemena, *ACS Omega* **2020**, 5, 20461.
- [166] C. Hou, Yu Wang, L. Zou, M. Wang, H. Liu, Z. Liu, H. Wang, C. Li, Q. Xu, *Adv. Mater.* **2021**, 33, 2101698.
- [167] M. Sen Bishwas, M. Malik, P. Poddar, *New J. Chem.* **2021**, 45, 7145.
- [168] Z. Jiang, P. Gao, L. Yang, C. Huang, Y. Li, *Anal. Chem.* **2015**, 87, 12177.
- [169] H. Kaur, N. Devi, S. Siwal, W. Alsanie, M. Thakur, V. Thakur, *ACS Omega* **2023**, 8, 9004.
- [170] a) M. Shamim, H. Zia, M. Zeeshan, M. Khan, M. Shahid, *J. Environ. Chem. Eng.* **2022**, 10, 106991; b) L. Esrafil, F. Firuzabadi, A. Morsali, M. Hu, *J. Hazard. Mater.* **2021**, 403, 123696; c) M. Adly, S. El-Dafray, A. Ibrahim, S. El-Hakam, M. El-Shall, *RSC Adv.* **2021**, 11, 13940; d) R. Paz, H. Viltres, N. Gupta, A. Romero-Galarza, C. Leyva, *Env. Sci. Adv.* **2022**, 1, 182.
- [171] a) J. Xia, Y. Gao, G. Yu, *J. Colloid Interface Sci.* **2021**, 590, 495; b) X. Li, Z. Yang, D. Hu, A. Wang, Y. Chen, Y. Huang, M. Zhang, H. Yuan, K. Yan, *Env. Sci. Nano* **2021**, 8, 2595; c) B. Wang, R. Qiu, J. Ou, M. Xiong, Y. Zeng, *Microporous Mesoporous Mater.* **2022**, 346, 112285.
- [172] Md J Uddin, R E. Ampiaiw, W. Lee, *Chemosphere* **2021**, 284, 131314.

- [173] X. Guo, L. Wang, L. Wang, Q. Huang, L. Bu, Q. Wang, *Front. Chem.* **2023**, *11*, 1116524.
- [174] V. Russo, M. Hmoudah, F. Broccoli, M. Ilesce, O. Jung, M. Di Serio, *Front. Chem. Sci. Eng.* **2020**, *2*, 581487.
- [175] X. Han, L. Besteiro, C. Koh, H. Lee, I. Phang, G. Phan-Quang, J. Ng, H. Sim, C. Lay, A. Govorov, X. Ling, *Adv. Funct. Mater.* **2021**, *31*, 2008904.
- [176] H. Kim, S. Yang, S. Rao, S. Narayanan, E. Kapustin, H. Furukawa, A. Umans, O. Yaghi, E. Wang, *Science* **2017**, *356*, 430.
- [177] A. Terzis, A. Ramachandran, K. Wang, M. Asheghi, K. Goodson, J. Santiago, *Cell Rep. Phys. Sci.* **2020**, *1*, 100057.
- [178] Y. Hu, Z. Fang, Xu Ma, X. Wan, S. Wang, S. Fan, Z. Ye, X. Peng, *Appl. Mater. Today* **2021**, *23*, 101076.
- [179] Q. Qian, P. Asinger, M. Lee, G. Han, K. Rodriguez, S. Lin, F. Benedetti, A. Wu, W. Chi, Z. Smith, *Chem. Rev.* **2020**, *120*, 8161.
- [180] M. Wu, Y. Yang, *Adv. Mater.* **2017**, *29*, 1606134.
- [181] A. Valverde, R. Gonçalves, M. Silva, S. Wuttke, A. Fidalgo-Marijuan, C. Costa, J. Vilas-Vilela, J. Laza, M. Arriortua, S. Lanceros-Méndez, R. Fernández De Luis, *ACS Appl. Energy Mater.* **2020**, *3*, 11907.
- [182] World Health Organization, Promoting cancer early diagnosis, accessed: 2023-09-18, <https://www.who.int/activities/promoting-cancer-early-diagnosis>.
- [183] M. Murray, J. Nicholson, *Arch. Dis. Child. Educ.* **2011**, *96*, 141.
- [184] D. Ball, E. Rose, E. Alpert, *An. J. Med. Sci.* **1992**, *303*, 157.
- [185] G. Savarese, P. Becher, L. Lund, P. Seferovic, G. Rosano, A. Coats, *Cardiovasc. Res.* **2022**, *118*, 3272.
- [186] European Commission, Opinion on p-Phenylenediamine, accessed: 2023-09-18, https://ec.europa.eu/health/scientific_committees/consumer_safety/docs/sccs_o_094.pdf.
- [187] European Commission, Risk Assessment Report on Methenamine, accessed: 2023-09-18, https://ec.europa.eu/health/ph_risk/committees/04_scher/docs/scher_o_054.pdf.
- [188] E. Authority, *EFSA J.* **2015**, *13*, 4073.
- [189] a) L. Malard, M. Pimenta, G. Dresselhaus, M. Dresselhaus, *Phys. Rep.* **2009**, *473*, 51; b) S. Krause, E. Ploetz, J. Bohlen, P. Schüler, R. Yaadav, F. Selbach, F. Steiner, I. Kaminska, P. Tinnefeld, *ACS Nano* **2021**, *15*, 6430; c) C. Lui, in *Raman Spectroscopy of Two-Dimensional Materials*, (Ed: P. Tan), Springer Singapore, Singapore **2019**, p. 81.
- [190] a) K. Jayaramulu, S. Mukherjee, D. Morales, D. Dubal, A. Nanjundan, A. Schneemann, J. Masa, S. Kment, W. Schuhmann, M. Otyepka, R. Zboril, R. Fischer, *Chem. Rev.* **2022**, *122*, 17241; b) H. Qu, L. Huang, Z. Han, Y. Wang, Z. Zhang, Y. Wang, Q. Chang, N. Wei, M. Kipper, J. Tang, *J. Porous Mater.* **2021**, *28*, 1837.
- [191] X. Xu, W. Shi, P. Li, S. Ye, C. Ye, H. Ye, T. Lu, A. Zheng, J. Zhu, L. Xu, M. Zhong, X. Cao, *Chem. Mater.* **2017**, *29*, 6058.
- [192] R. Bajwa, U. Farooq, S. Ullah, M. Salman, S. Haider, S. Shahida, B. Farooqi, E. Elkaeed, *J. Saudi Chem. Soc.* **2023**, *27*, 101691.
- [193] a) A. Amini, M. Khajeh, A. Oveisi, S. Daliran, M. Ghaffari-Moghaddam, H. Delarami, *J. Ind. Eng. Chem.* **2021**, *93*, 322; b) Y. Wang, L. Guo, P. Qi, X. Liu, G. Wei, *Nanomaterials* **2019**, *9*, 1123
- [194] S. Pandit, Z. Cao, V. Mokkapati, E. Celauro, A. Yurgens, M. Lovmar, F. Westerlund, J. Sun, I. Mijakovic, *Adv. Mater. Interfaces* **2018**, *5*, 1701331.
- [195] M. Firouzjaei, A. Shamsabadi, S. Aktij, S. Seyedpour, M. Sharifian Gh, A. Rahimpour, M. Esfahani, M. Ulbricht, M. Soroush, *ACS Appl. Mater. Interfaces* **2018**, *10*, 42967.
- [196] M. Kalaj, K. Bentz, S. Ayala, J. Palomba, K. Barcus, Y. Katayama, S. Cohen, *Chem. Rev.* **2020**, *120*, 8267.
- [197] D. Maurya, S. Khaleghian, R. Sriramdas, P. Kumar, R. Kishore, M. Kang, V. Kumar, H. Song, S. Lee, Y. Yan, J. Park, S. Taheri, S. Priya, *Nat. Commun.* **2020**, *11*, 5392.
- [198] a) U. Schmidt, S. Hild, W. Ibach, O. Hollricher, *Macromol. Symp.* **2005**, *230*, 133; b) B. Prats-Mateu, N. Gierlinger, *Microsc. Res. Tech.* **2017**, *80*, 30; c) W. Van Beek, O. Safonova, G. Wiker, H. Emerich, *Phase Trans.* **2011**, *84*, 726; d) R. Schmidt, M. Nachtnebel, M. Dienstleder, S. Mertschnigg, H. Schroettner, A. Zankel, M. Poteser, H. Hutter, W. Eppel, H. Fitzek, *Micron* **2021**, *144*, 103034; e) C. Cardell, I. Guerra, *Trends Anal.* **2016**, *77*, 156.
- [199] K. Jablonka, D. Ongari, S. Moosavi, B. Smit, *Chem. Rev.* **2020**, *120*, 8066.
- [200] a) F. Lussier, V. Thibault, B. Charron, G. Wallace, J. Masson, *Trends Anal.* **2020**, *124*, 115796; b) L. Pan, P. Zhang, C. Daengngam, S. Peng, M. Chongcheawchamnan, *J. Raman Spectrosc.* **2022**, *53*, 6; c) Y. Zhengmao, *IEEE Trans. Auom. Sci. Eng.* **2005**, *2*, 67.



Jonas Tittel studied at LMU Munich and TU Berlin and received his MSc. degree in Physics from LMU Munich in 2022. In his Ph.D., he develops new cutting-edge techniques based on vibrational spectroscopy and label-free imaging to follow the storage and catalytic transformation of substances like water and CO₂ in porous materials for environmental applications.



Fabian Knechtel is a doctoral student in Physical Chemistry at the LMU Munich. His research focuses on coherent Raman imaging and spectroscopy in the field of material science. He studies transport processes as well as host-guest interactions in porous materials. Currently, he applies advanced multimodal imaging for water harvesting applications in MOFs.



Evelyn Ploetz is a group leader at the Department of Chemistry at LMU Munich working on the development of advanced imaging and spectroscopy techniques to study transport phenomena and chemical processes in biological and functional materials. Her research focuses on the uptake, transport, and release mechanism of guest molecules in porous materials for harvesting, storage, and drug-delivery applications, offering insights at both molecular and particle levels. Her lab employs label-free nonlinear multimodal imaging and spectroscopy as analytical tools to study dynamic processes in real-time.